



19941228 032

MEASUREMENT OF N<sub>2</sub> MOBILITY IN He VIA  
FOURIER TRANSFORM EMISSION SPECTROSCOPY

THESIS

Patrick D. Kee, Captain, USAF

AFIT/GAP/EN/94D-4

DEPARTMENT OF THE AIR FORCE  
AIR UNIVERSITY  
**AIR FORCE INSTITUTE OF TECHNOLOGY**

Wright-Patterson Air Force Base, Ohio

AFIT/GAP/EN/94D-4

MEASUREMENT OF  $N_2^+$  MOBILITY IN He VIA  
FOURIER TRANSFORM EMISSION SPECTROSCOPY

THESIS

Patrick D. Kee, Captain, USAF

AFIT/GAP/EN/94D-4

Approved for public release; distribution unlimited

Accesion For	
NTIS	CRA&I <input checked="" type="checkbox"/>
DTIC	TAB <input type="checkbox"/>
Unannounced <input type="checkbox"/>	
Justification _____	
By _____	
Distribution / _____	
Availability Codes	
Dist	Avail and/or Special
A-1	

### Disclaimer

The views expressed in this thesis are those of the author and do not reflect the official policy or position of the Department of Defense or the U.S. Government.

MEASUREMENT OF  $N_2^+$  MOBILITY IN He VIA  
FOURIER TRANSFORM EMISSION SPECTROSCOPY

THESIS

Presented to the Faculty of the School of Engineering  
Air Education and Training Command  
In Partial Fulfillment of the  
Requirements for the Degree of  
Master of Science in Engineering Physics

Patrick D. Kee, B.A.

Captain, USAF

December 1994

Approved for public release; distribution unlimited

## Preface

The aim of this experiment was to determine the mobility of an ion in a buffer gas, specifically  $N_2^+$  in helium, via spectroscopic means. That this experiment failed to produce a value for the mobility, due to the insensitivity of the fitting function to the parameter of interest, does not imply a failure of the experiment. The lessons learned from this experiment underscore the necessity of understanding the statistical significance of experimental results, and the necessity of using statistical methods to design an experiment. These lessons are particularly timely as I prepare to assume my duties in a gas analysis laboratory, where I will be involved in improving the performance of a gas analysis system.

I would like to thank Dr. Charles DeJoseph, my advisor at Wright Laboratory, for allowing me to work with his beloved Bomem Fourier Transform Spectrometer, and allowing me to learn by example during the summer months. Thanks also go to Dr. William Bailey, my AFIT advisor, for influencing my selection of this project, and helping me achieve closure with this thesis by assisting me with his insight of the kinetics of the discharge. I am also grateful to Dr. Alan Garscadden, of Wright Laboratory, for serving on the committee, and for offering possible explanations for the disagreement between my measurements, and those of other researchers. (Alan, after five years, you finally got a presentation out of me!). I am indebted to Dr. Rajesh Nagpal, a participant in the AFOSR Senior Investigator Program, who provided the calculations of the electron energy distribution function, which were essential for explaining the discrepancy between

my observations and previously published results. I am also indebted to Dr. Kirk Mathews for providing guidance in solving the nonlinear least-squares fitting problem. I would also like to recognize the significant contributions of Mike Ray, for crafting four different discharge tubes for this study, and Robert Knight, for providing me with the use of his pumpstation.

On a personal note, I would like to take a moment to thank those who contributed to my scientific career. Success in the pursuit of excellence is the result of responding to the challenge of high standards. Some who set high standards in my life were not appreciated at the time, so now I set the record straight: Sr. Lucinda Girard, my high school algebra instructor, deserves special thanks for laying the foundation of my knowledge of mathematics. Her method was simple and effective: homework, homework, homework, and when you're tired of it, more homework. Mr. Stephen Hamersky and Bro. Timothy Pieprzyca also placed high demands in their physics and chemistry classes, and strongly influenced my choice of career. However, none of these opportunities would have been available, were it not for the love, inspiration, and financial sacrifice of my parents, Eugene and Mary Kee, who were determined to provide a quality, value-based education for their six children. To them, this work is dedicated.

Patrick D. Kee

## Table of Contents

	Page
Preface.....	i
List of Figures.....	v
List of Tables.....	viii
Abstract.....	ix
I. Introduction.....	1
A. Purpose and Relevance.....	1
B. Definition of Ion Mobility.....	1
C. Approaches to the Experimental Determination of Ion Mobility.....	2
1. Drift Tube Measurements.....	2
Biondi and Chanin.....	3
McFarland, et al.....	4
2. Optical Measurements of Drift Velocity.....	4
Haese, Pan, and Oka.....	5
Gudeman, et al.....	6
Radunsky and Saykally.....	7
Martin and Guelachvili.....	7
Hong and Miller.....	7
D. Problem, Scope, and Approach.....	11
E. Overview.....	12
II. Theory.....	13
A. Determination of Mobility.....	13
1. Calculation of Time Averaged Observed Ensemble Velocity.....	14
2. Derivation of Ion Average Velocity.....	15
3. Derivation of Emission Probability Density.....	15
4. Derivation of E-scaled Doppler shift.....	17
5. Calculation of Ion Mobility from Collision Cross-Section.....	17
B. Theory of Fourier Transform Spectrometer.....	19
1. The Interferogram and its Relation to the Spectrum.....	19
2. Sampling Function.....	21
3. Recovery of Spectra.....	22

4. Elimination of Phase Error.....	23
5. Limits of Resolution.....	23
III. Equipment and Software.....	25
A. Discharge Tube.....	25
B. Vacuum System (Including Flow System).....	27
1. Static Gas Fill.....	27
2. Flowing Gas System.....	28
C. DC Discharge Power Supply.....	29
D. Fourier-Transform Spectrometer.....	29
E. Electric Field Measurement System.....	32
IV. Procedure.....	34
A. Measurement of Tube Dimensions.....	34
B. Calibration of FTS System: Phase File.....	34
C. Alignment of Discharge Tube.....	35
D. Acquisition of Spectra.....	36
E. Determination of Ion Temperatures.....	38
F. Voltage Measurements.....	39
V. Results and Analysis.....	40
A. Data.....	40
1. Static Gas Fill.....	40
Electric Field.....	40
Doppler Shift.....	42
Temperature.....	44
2. Flowing Gas.....	47
Electric Field.....	47
Doppler Shift.....	49
Temperature.....	50
B. Analysis.....	54
1. Corrections to Electric Field in Low Pressure Limit.....	54
2. E-scaled Doppler Shift vs Pressure.....	57
3. Disagreement with Hong-Miller Experiment.....	61
4. Plot of $\chi^2$ surface.....	63
Comparison to Hong-Miller results.....	71
VI. Conclusion and Recommendations.....	75
A. Summary of Results.....	75
B. Recommendations for Further Research.....	75

Appendix A: Example Search for Minima of $\chi^2$ .....	77
Appendix B: Residence Time in Discharge Tube.....	81
Appendix C: Resolution of Spectrometer.....	83
Bibliography.....	87
Vita.....	90

## List of Figures

<u>Figure</u>	<u>Page</u>
1. Biondi-Chanin Experiment.....	3
2. Haese, Pan, and Oka Experiment.....	6
3. Hong and Miller Experiment.....	8
4. Doppler Shift in $N_2^+$ emission spectra.....	9
5. Michelson Interferometer.....	20
6. Discharge Tube.....	25
7. Probe Design.....	26
8. Static Gas Fill Vacuum System.....	28
9. Schematic of Fourier Transform Spectrometer.....	31
10. Electric Field Measurement System.....	32
11. Peak Picking Program.....	33
12. E vs P, Static Fill, $I = 1$ mA.....	40
13. E vs P, Static Fill, $I = 5$ mA.....	41
14. E vs P, Static Fill, $I = 10$ mA.....	42
15. Doppler Shift vs Pressure, Static Fill, $I = 1$ mA.....	43
16. Doppler Shift vs Pressure, Static Fill, $I = 5$ mA.....	43
17. Doppler Shift vs Pressure, Static Fill, $I = 10$ mA.....	44
18. Ion Temperature vs Pressure, Static Fill, $I = 1$ mA.....	45
19. Ion Temperature vs Pressure, Static Fill, $I = 5$ mA.....	45
20. Ion Temperature vs Pressure, Static Fill, $I = 10$ mA.....	46
21. Ion Temperature vs Current, Static Fill.....	46
22. E vs P, Flowing Gas, $I = 1$ mA.....	47
23. E vs P, Flowing Gas, $I = 5$ mA.....	48
24. E vs P, Flowing Gas, $I = 10$ mA.....	48
25. Doppler Shift vs Pressure, Flowing Gas, $I = 1$ mA.....	49
26. Doppler Shift vs Pressure, Flowing Gas, $I = 5$ mA.....	50
27. Doppler Shift vs Pressure, Flowing Gas, $I = 10$ mA.....	50
28. Ion Temperature vs Pressure, Flowing Gas, $I = 1$ mA.....	51
29. Ion Temperature vs Pressure, Flowing Gas, $I = 5$ mA.....	52
30. Ion Temperature vs Pressure, Flowing Gas, $I = 10$ mA.....	52
31. Ion Temperature vs Current, Static Fill.....	53
32. Adjusted Electric Field vs Pressure, Static Fill, $I = 1$ mA.....	54
33. Adjusted Electric Field vs Pressure, Static Fill, $I = 5$ mA.....	55
34. Adjusted Electric Field vs Pressure, Static Fill, $I = 10$ mA.....	55
35. Adjusted Electric Field vs Pressure, Flowing Gas, $I = 1$ mA.....	56
36. Adjusted Electric Field vs Pressure, Flowing Gas, $I = 5$ mA.....	56
37. Adjusted Electric Field vs Pressure, Flowing Gas, $I = 10$ mA.....	57

38.	E-scaled Doppler Shift vs Pressure, Static Fill, I = 1 mA.....	58
39.	E-scaled Doppler Shift vs Pressure, Static Fill, I = 5 mA.....	58
40.	E-scaled Doppler Shift vs Pressure, Static Fill, I = 10 mA.....	59
41.	E-scaled Doppler Shift vs Pressure, Flowing Gas, I = 1 mA.....	59
42.	E-scaled Doppler Shift vs Pressure, Flowing Gas, I = 5 mA.....	60
43.	E-scaled Doppler Shift vs Pressure, Flowing Gas, I = 10 mA.....	60
44.	$N_2^+(B)$ Formation Processes.....	61
45.	Electron Energy Distribution Function.....	62
46.	$\chi^2$ Plot, Static Fill, I = 1 mA.....	66
47.	$\chi^2$ Plot, Static Fill, I = 5 mA.....	67
48.	$\chi^2$ Plot, Static Fill, I = 10 mA.....	68
49.	$\chi^2$ Plot, Flowing Gas, I = 1 mA.....	69
50.	$\chi^2$ Plot, Flowing Gas, I = 5 mA.....	70
51.	$\chi^2$ Plot, Flowing Gas, I = 10 mA.....	71
52.	$\chi^2$ Plot, Hong-Miller Experiment, I = 25 mA.....	73
53.	Insensitivity of Fitting Equation to Choice of $Q_v$ for Hong-Miller Data.....	74

## List of Tables

<u>Table</u>	<u>Page</u>
1. $\chi^2$ values, Static Fill, I = 1 mA.....	66
2. $\chi^2$ values, Static Fill, I = 5 mA.....	67
3. $\chi^2$ values, Static Fill, I = 10 mA.....	68
4. $\chi^2$ values, Flowing Gas, I = 1 mA.....	69
5. $\chi^2$ values, Flowing Gas, I = 5 mA.....	70
6. $\chi^2$ values, Flowing Gas, I = 10 mA.....	71
7. $\chi^2$ values, Hong-Miller Experiment, I = 25 mA.....	73

### Abstract

Recently, Hong and Miller used Fourier Transform Emission (FTE) spectroscopy to determine the  $N_2^+$  mobility in helium by relating the observed Doppler shift of the  $N_2^+$  (B-X) transition to the measured electric field in the discharge as determined by probes. In order to establish the technique in house, this effort duplicated that experiment and investigated the sensitivity and utility of that method. Doppler shift measurements in this experiment disagreed significantly with those reported by Hong and Miller. Attempts to reduce the data (and thus determine the mobility) using a model developed by Hong and Miller were unsuccessful. The model did not qualitatively or quantitatively describe the Doppler shifts observed in this work. At this time, an explanation for the differences between the two experiments is not known. Possibilities include effects of striations on the Doppler shift measurements, competition between one- and two-step excitation of the  $N_2^+$  (B) state, and failure to interpret the Hong and Miller model correctly. Subsequent attempts to model Hong and Miller's own data (taken from their figures) yielded mobility parameters which disagreed with their published results.

# MEASUREMENT OF $N_2^+$ MOBILITY IN He VIA FOURIER TRANSFORM EMISSION SPECTROSCOPY

## I. Introduction

### A. Purpose and Relevance

The study of the transport of ions in gases yields information applicable to scientific investigations of interest to the Air Force. The determination of the ion mobility, a coefficient that relates an ion's drift velocity in a buffer gas to an applied electric field, can yield collision cross-section data essential for a quantitative understanding of gas discharges and atmospheric phenomena [1:8]. Current Air Force research projects that may benefit from ion-mobility data include: studies of atmospheric phenomena, and gas discharge lasers.

In this effort, the mobility of  $N_2^+$  ions will be measured in a carrier gas using Fourier-transform spectroscopy, and will be compared to previously published values obtained from both drift tube and spectroscopic measurements.

### B. Definition of Ion Mobility

The *ion mobility*, K, is defined as:

$$K = \frac{v_d}{E} \quad (1)$$

where  $v_d$  is the drift velocity of an ion in either a parent or buffer gas, and  $E$  is the electric field. The measurements of the two quantities are necessary for the determination of the ion mobility. Electric field measurements are often made using probes, while drift velocity measurements have been made by several methods. These measurements can be conveniently divided into two areas: drift tube measurements, and optical drift velocity measurements. Illustrative examples of both techniques are discussed in the following sections.

Ion mobility measurements are taken under a variety of experimental conditions. To compare the ion mobilities taken under different temperatures and pressures, a quantity known as the *reduced ion mobility*,  $K_o$ , is defined as:

$$K_o = K \frac{P}{760 \text{ torr}} \frac{273.16 \text{ Kelvin}}{T} \quad (2)$$

where  $K$ ,  $P$ , and  $T$  are respectively the experimental values for the ion mobility, buffer gas pressure, and buffer gas temperature.

### C. Approaches to the Experimental Determination of Ion Mobility

1. Drift Tube Measurements. A drift tube has been the most common device used to measure the drift velocity of ions. The principle of operation is to measure the time of flight of ions through a buffer gas, across a known distance. The essential characteristics of a drift tube apparatus are a vacuum system, a pulsed ion source, a pair of electrodes to accelerate the ion cloud, probes for measuring the electric field, and an ammeter connected to the collector [1:32]. Variations in drift tube design may include

mass spectrometers to separate ions of interest from other ionic species, and flowing-afterglow discharges for ion production for the drift tube.

Biondi and Chanin. In an experiment by M.A. Biondi and L.M. Chanin [2], (see Figure 1), ions are produced by a high voltage pulse in a drift tube in a region between an electrode and a grounded grid. An electric field applied between the electrode and the grid accelerates the ions, which penetrate the grid and enter the drift space of the tube. The ion current in the drift tube induces a current across a resistor in an external circuit. The voltage across the resistor is measured and displayed on an oscilloscope, with an external trigger supplied by the pulse generator. Then with  $v_d = d/t$  and  $E = V/d$ , the ion mobility is determined by:

$$K = \frac{d^2}{Vt} \quad (3)$$

where  $d$  is the spacing between the grid and the negative electrode,  $V$  is the potential difference between the grounded grid and the negative electrode, and  $t$  is the transit time of the ion across the drift space. Similar techniques were used to determine the  $N_2^+$  ion mobility in helium [3], yielding a result of  $K_o = 19 \pm 2 \text{ cm}^2/\text{volt/sec.}$

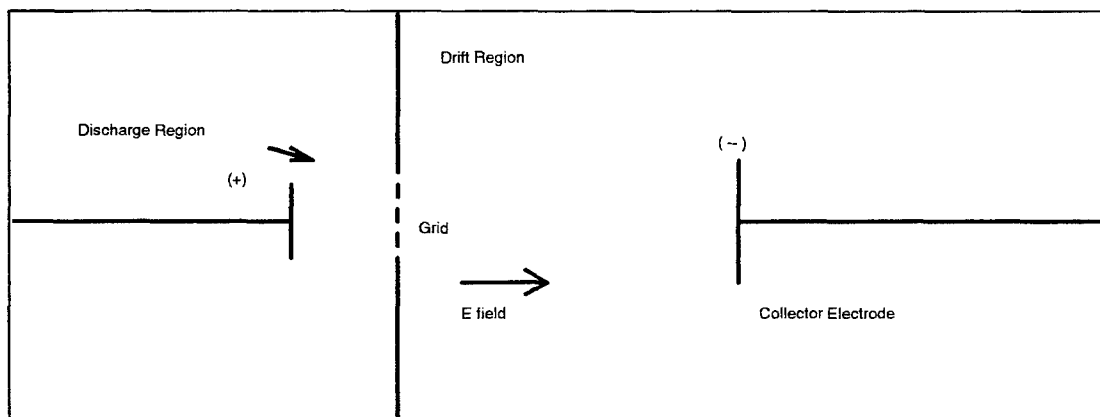


Figure 1. Biondi-Chanin Experiment

McFarland, et al. McFarland, *et al*, combined a flowing afterglow system with a drift tube apparatus to measure the mobilities of a variety of ions, including  $\text{N}_2^+$ , with helium as the buffer gas [4]. The flowing afterglow system was used for measurement of reaction rates by accelerating a steady-state stream of ions through a reactant gas in a drift tube. When the reactant gas was replaced with a buffer gas, and the ions produced in a pulsed mode, the ion mobility was then determined from the time of flight of the ion through the drift tube. The results of their measurement yielded a value of  $K_o = 21.0 \pm 1.3 \text{ cm}^2/\text{volt/sec}$ , which agrees with the previously measured value of Johnsen, Brown, and Biondi [3]. Advantages of the flowing afterglow/drift tube apparatus over a conventional drift tube device include the ability to measure the mobility of negative ions (which was done with  $\text{H}^-$ ,  $\text{O}^-$ , and  $\text{OH}^-$  in helium). In addition, measurements were made of the reaction rates of ions with neutrals as a function of the ion kinetic energy.

2. Optical Measurements of Drift Velocity. Advances in spectroscopy in the last fifteen years have permitted the observation of high-resolution vibration-rotation spectra of gas phase molecular ions in a dc discharge [5]. If a spectrometer has sufficient resolution to measure the spectral shift due to the Doppler effect of an ion in a dc discharge, then the drift velocity of the ion can be determined from the Doppler shift. The advantage of this technique over a drift tube apparatus is that the spectra of an ionic species can be distinguished from other ions in the discharge, whereas with a drift tube, care must be taken to differentiate among the time-of-arrival of many ionic species.

The first successful spectroscopic measurement of an ion mobility was performed by Haese, Pan, and Oka using infrared laser spectroscopy [5]. Subsequent work in detecting faint molecular ion absorption lines was pioneered by Gudeman, *et al*, with a technique known as ‘velocity modulation’ [6]. Radunsky and Saykally then applied velocity modulation to the measurement of axial electric fields in a He/N<sub>2</sub> discharge by using the established value of the N<sub>2</sub><sup>+</sup> mobility in helium and the observed Doppler shift in the N<sub>2</sub><sup>+</sup> spectra [7]. Velocity modulation was extended to the case of emission by Martin and Guelachvili [8], who combined the technique with Fourier-transform spectroscopy (FTS) for the selective detection of molecular ions, and discussed the feasibility of applying this method to the measurement of quantum-state specific ion mobilities. Most recently, Hong and Miller applied Fourier-transform spectroscopy with a reversible-polarity discharge with results that agree well with previous results [9].

Haese, Pan, and Oka. Haese, Pan, and Oka performed the first successful spectroscopic ion mobility measurement, using infrared laser spectroscopy to observe the drift-velocity induced Doppler shift in ArH<sup>+</sup> known vibration-rotation absorption lines [5]. Using a beamsplitter, Haese, Pan, and Oka illuminated the positive column of the discharge from opposite ends of the discharge tube, simultaneously measuring the blue and red shifted absorption spectra (see Figure 2). The drift velocity of the ions was deduced from the Doppler shift in the vibration-rotation absorption lines, while the axial electric field was measured with platinum wire probes. The calculated values for the ion mobility of ArH<sup>+</sup> agreed with a previous mass-spectroscopic drift-tube study [10].

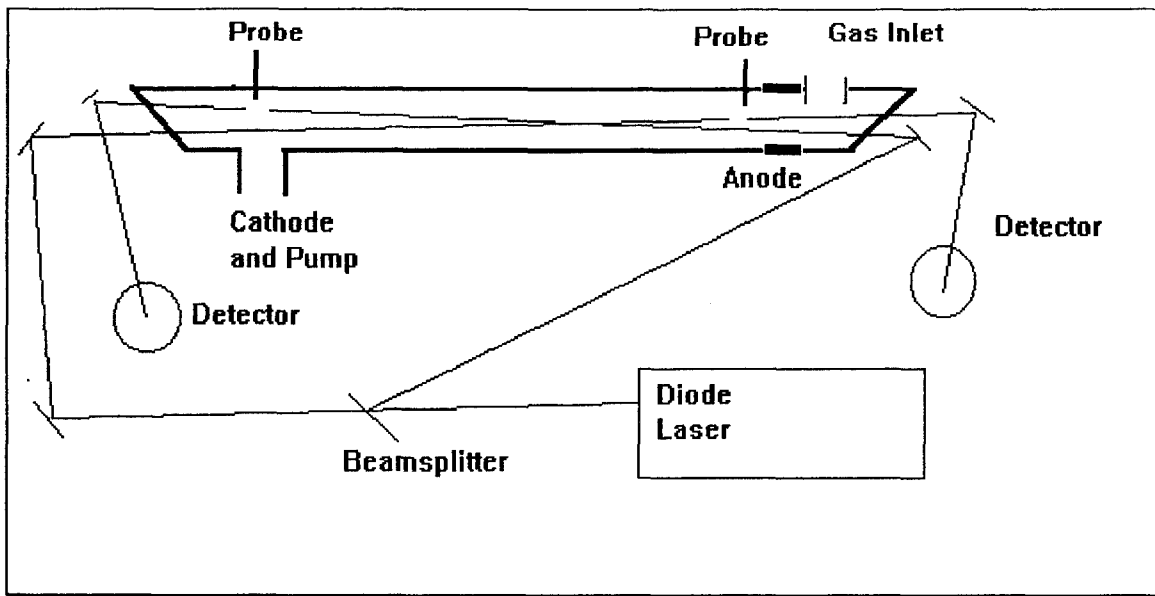


Figure 2. Haese, Pan, and Oka Experiment

Gudeman, et al. One complication faced in obtaining ion spectra when the ion number density is a small fraction of the total gas density, is that the signal from ion absorption may be much less than that from neutral absorption [6]. One of the first successful measurements of the infrared spectrum of a molecular ion was by Gudeman, Begemann, Pfaff, and Saykally, using the “velocity modulation” method [6]. The  $\text{HCO}^+$  ion absorption spectrum was obtained by modulating the polarity of a gas discharge at several kilohertz. The modulation of the discharge polarity resulted in both red- and blue-shifted absorption peaks. This Doppler shift was used to separate ion transitions from the more intense neutral transitions. The ion mobility was not measured in this experiment, but the concept of modulating the polarity of the discharge to obtain ionic spectra would be adopted by Hong and Miller for their ion mobility measurements.

Radunsky and Saykally. Radunsky and Saykally applied the velocity modulation method in combination with laser absorption spectroscopy to determine the axial electric field in a glow discharge of a N<sub>2</sub>/He mixture [7]. In their experiment, the shift in the absorption spectra of N<sub>2</sub><sup>+</sup> was measured, and related to the axial electric field using the previously published value of the N<sub>2</sub><sup>+</sup> mobility in helium.

Martin and Guelachvili. This velocity modulation method was extended to the case of emission by Martin and Guelachvili [8]. They combined velocity modulation of the ions with Fourier transform spectroscopy (FTS) to selectively detect molecular ions in a discharge, and to measure the ratio of the dipole moment to the vibrational transition moment of ArH<sup>+</sup>. FTS has the advantage over laser absorption spectroscopy of having wide and continuous spectral coverage, as well as having more consistent wave-number accuracy. No ion mobility measurements were made in this experiment, however, it was suggested in this paper that this technique could be used to determine the excited-state mobilities of ions [8].

Hong and Miller. Hong and Miller applied the FTS technique to determine the ion mobility of N<sub>2</sub><sup>+</sup> in He, and fit their data to a theoretical model to determine the velocity changing and quenching cross sections for He-N<sub>2</sub><sup>+</sup> collisions [9]. N<sub>2</sub><sup>+</sup> ions were produced in a dc discharge, the Doppler shift in both the B<sup>2</sup>Σ<sub>u</sub><sup>+</sup>(v=0)-X<sup>2</sup>Σ<sub>g</sub><sup>+</sup>(v=1), and the A<sup>2</sup>Π<sub>u</sub>(v=1)-X<sup>2</sup>Σ<sub>g</sub><sup>+</sup>(v=0) transitions were observed. To select red- or blue-shifting of the emission spectra, the polarity of the electrodes could be swapped by a computer controlled switch connected to the power supply (see Figure 3). The discharge was viewed with a high-resolution Fourier transform spectrometer, and successive spectra

were taken by first viewing from one polarity, then with the polarity reversed. Because the spectra were taken under nearly identical conditions (except direction of ion drift velocity), the only differences in the resulting spectra were the opposite signs of Doppler shift. Taking the difference of the red- and blue-shifted spectra isolated the emission peaks due to ionic transitions, and the Doppler shift was obtained by taking half the separation between the blue and red shifted peaks. Figure 4 displays the Doppler shift observed by the author in the  $N_2^+$  spectra as a result of switching the electrode polarities between measurements.

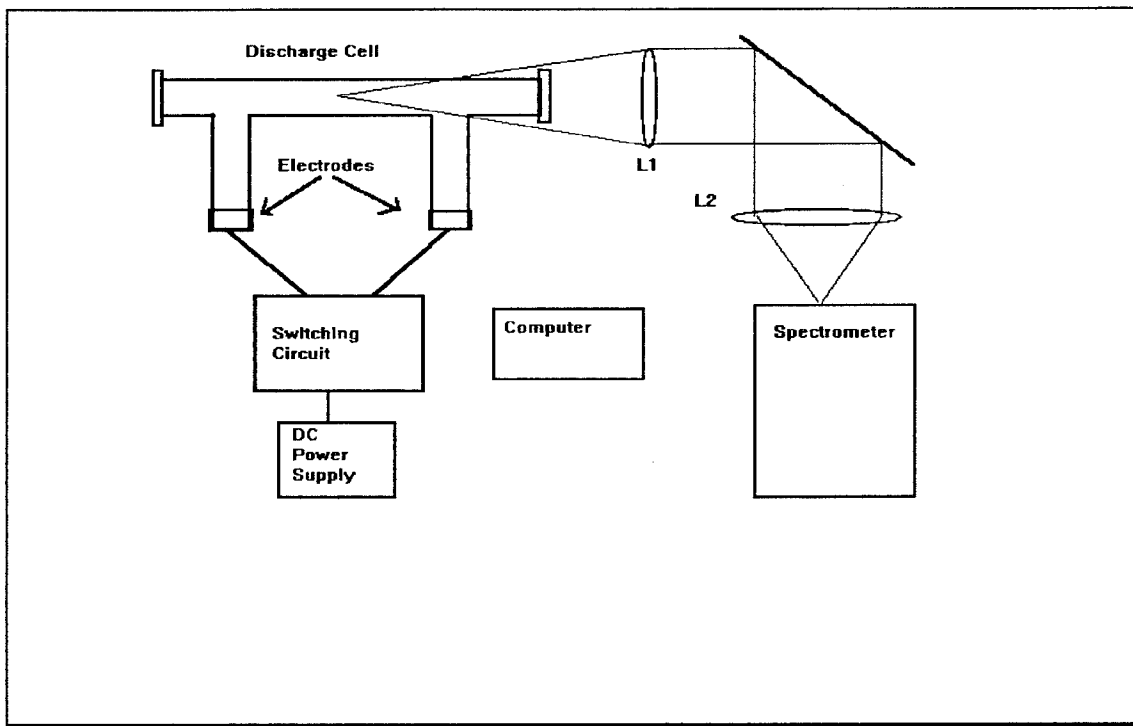


Figure 3. Hong and Miller Experiment.

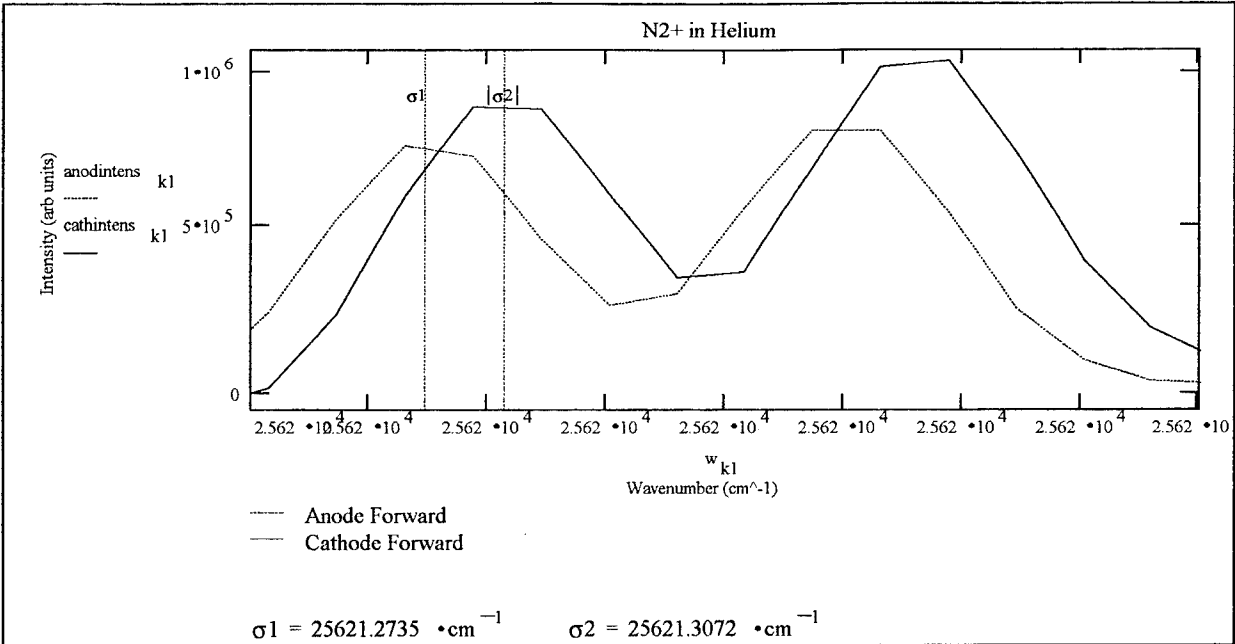


Figure 4. Doppler Shift in  $\text{N}_2^+$  emission spectra (Author's data).

The electric field was estimated by using one of two methods. At pressures below 1 torr, (no collision limit), the electric field can be determined from Doppler shift of the short-lived  $\text{B} \rightarrow \text{X}$  transition of  $\text{N}_2^+$ , (for which  $\tau=66\text{ns}$ ) [11]:

$$E_D = \frac{M\Gamma c}{\left[ 1 - \frac{1}{1 + \Gamma\tau} \frac{1 - \exp\left(-\frac{\lambda_q}{V\tau} - \frac{\Gamma\lambda_q}{V}\right)}{1 - \exp\left(-\frac{\lambda_q}{V\tau}\right)} \right]} \frac{\Delta v}{v_o e} \quad (4)$$

where  $M$  is the ion mass,  $\Gamma$  is the collision frequency,  $\lambda_q$  is the mean free path for quenching collisions,  $V$  is the ion-molecule relative velocity,  $\tau$  is the radiative lifetime of the upper quantum state of the ion,  $\Delta v$  and  $v_o$  are respectively the shift in the emission frequency, and the emission frequency, and  $c$  is the velocity of light. In the no collision limit, ( $N \rightarrow 0$ ), equation (4) becomes:

$$E_D = \frac{M\Gamma c}{1 - \frac{1}{1 + \Gamma\tau}} \frac{\Delta v}{ev_o} \quad (5)$$

If the product  $\Gamma\tau$  is small, then performing the binomial expansion on  $(1+\Gamma\tau)^{-1}$  leads to:

$$E_D = \frac{Mc}{e\tau} \frac{\Delta v}{v_o} \quad (6)$$

At pressures below than 1 torr, this is a good approximation for the short-lived  $B \rightarrow X$  transition. At pressures above 1 torr, this is not a good approximation, nor is it a good approximation for the longer lived  $A \rightarrow X$  transition.

Hong and Miller also used probes to measure the electric field. The electric field measured by probes at low pressures was observed to differ by a constant of 1.5 V/cm from the result obtained from equation (6) using the measured Doppler shift. This offset was attributed to sheath effects and probe positioning. The estimated value of the electric field was then taken to be the probe measurement minus the offset value. This estimated value was used at pressures above 1 torr, and for the  $A \rightarrow X$  transition, where equation (6) no longer applies (due to the longer lifetime of the  $A$  state). Hong and Miller's results for the electric field agreed well with Radunsky and Saykally, who used velocity modulation IR laser absorption spectroscopy in a similar  $N_2$ -He glow discharge [7]. The resulting  $N_2^+$  reduced ion mobility for the  $B \rightarrow X$  transition was  $16.6 \text{ cm}^2/\text{V/s}$ , and  $20.7 \text{ cm}^2/\text{volt/sec}$  for the  $A \rightarrow X$  transition, as compared to the established value of  $19 \text{ cm}^2/\text{V/s}$  [3].

#### D. Problem, Scope, and Approach.

In this effort, the mobility of the  $\text{N}_2^+$  ion is measured in helium using Fourier-transform emission spectroscopy. This value for the mobility is compared to results obtained from both drift tube and spectroscopic measurements. The  $\text{N}_2^+ - \text{He}$  collision cross-section is determined as a fitting parameter from a relationship between the Doppler shift of the ionic spectra to the pressure. Then the mobility is computed from the collision cross-section. The development of these relationships is presented in the Theory.

The transition observed in computing the Doppler shift was the  $\text{B}^2\Sigma_u^+(v=0)$ - $\text{X}^2\Sigma_g^+(v=0)$ . This differs from Hong and Miller who used the weaker  $v = 0 \rightarrow 1$  transition [9]. Measurements were not taken of the A-X transition. Pressures in this experiment varied from 0.25 torr to 6 torr, while discharge current was varied from 1 to 10 mA. Higher currents were not used due to observed sputtering in the tube. In comparison, the Hong-Miller experiment maintained the discharge at 25 mA.

The experimental setup is similar to that of Hong and Miller, is described in Chapter III. The discharge tube has the same internal diameter, however, a significant variation is that provisions are made in this effort for both flowing gas and a static gas fill. Axial electric fields are measured using four bare tungsten voltage probes inserted in the positive column. The probe voltage is plotted as a function of distance of the probe from an electrode, and the absolute value of the slope is taken as the electric field.

### E. Overview.

The following sections present in detail the effort to determine the  $\text{N}_2^+$  mobility in helium. Essential background theory is developed and presented in Chapter II. This includes the expressions that relate the Doppler shift in the  $\text{N}_2^+$  spectra to the collision cross-section for  $\text{N}_2^+$  and He, and the computation of the ion mobility from the collision cross-section. This also includes a brief survey of the principles of Fourier-transform spectroscopy.

The equipment used for the experiment, and the algorithms used in the analysis are discussed in Chapter III, followed by a description in Chapter IV of the experimental and analytical procedures. Results are analyzed, presented, and discussed in Chapter V. Conclusions drawn from this effort and recommendations for further efforts are presented in Chapter VI.

## II. Theory

### A. Determination of Mobility

The shift in the spectral lines, from an ensemble of ions drifting in a buffer gas under the influence of an electric field, can be related to the drift velocity by the Doppler relation:

$$\Delta v = \frac{\langle u_r \rangle}{c} v_o \quad (7)$$

where  $\langle u_r \rangle$  is the time average of the ensemble average velocity of the absorbing/emitting ions along the direction of the electric field. For the case of absorption, the ground state ion is observed, and the Doppler shift in the absorption spectra is a measure of average ground state ion velocity. This means that  $\langle u_r \rangle$  is equal to  $v_d$ . Thus in the case of absorption spectroscopy, the mobility can be directly calculated from:

$$K = \frac{v_d}{E} = \frac{\langle u_r \rangle}{E} = \frac{c\Delta v}{v_o E} \quad (8)$$

For emission, it is an upper state that is being observed. The probability that an ion in an excited state will emit a photon is a function of time, and is related to the lifetime of the upper state. This finite lifetime means that the Doppler shift measures the time average of the mean velocity of the ions accumulated prior to emission, not the average drift velocity:

$$\langle u_r \rangle \neq v_d \quad (9)$$

Hence, the mobility must be calculated by another method than equation (8) for the case of emission spectroscopy. To do this, a simple model is presented in the following sections that relates the observed Doppler shift to the collision cross-section, and thus, to the ion mobility.

1. Calculation of Time Averaged Observed Ensemble Velocity. The time average of the mean observed ion velocity for an ensemble of ions is defined as:

$$\langle \mathbf{u}_r \rangle = \frac{\int_0^{t_q} P(t) \mathbf{u}_r(t) dt}{\int_0^{t_q} P(t) dt} \quad (10)$$

where  $P(t)$  is the probability of emission per unit time, or *emission probability density*. Here,  $t_q$  is the mean time between quenching collisions for the ion and is defined as:

$$t_q = \frac{\lambda_q}{V} \quad (11)$$

where  $V$  is the rms average velocity of the reduced collision mass,  $\mu$ , and  $\lambda_q$  is the mean free path for quenching [9]. The mean time between quenching is chosen as the upper limit for the time average, because for  $t > t_q$ , ions are not expected to be in the excited state, and no longer contribute to the observed Doppler shift.  $V$  is determined by equation (12), where  $k_B$  is Boltzmann's constant, and  $T$  is the ion/gas temperature (assuming equilibrium) [12:121]:

$$V = \sqrt{\frac{3k_B T}{\mu}} \quad (12)$$

The mean free path for quenching can be expressed as [9]:

$$\frac{1}{\lambda_q} = \sum_i Q_q(i) N_i + \frac{\gamma_i}{V} \quad (13)$$

where  $Q_q(i)$  is the quenching cross section for the ion with the  $i^{\text{th}}$  buffer gas and  $\gamma_i$  is the ambipolar diffusion rate of arrival of ions at the wall.

2. Derivation of Ion Average Velocity. For an ion moving under the influence of an electric field in a buffer gas, the differential equation of motion for the ion can be expressed as [13:565]:

$$M \frac{du_r}{dt} = eE - \alpha u_r \quad (14)$$

where  $M$  is the ion mass,  $\alpha u_r$  is the Stoke's resistance term and  $\alpha$  is a function of the viscosity of the buffer gas.

Equation (14) is a linear first order differential equation, and the solution is:

$$u_r = \frac{eE}{M\Gamma} (1 - \exp(-\Gamma t)) \quad (15)$$

where  $\Gamma = \alpha/M$  is the ion collision frequency.

3. Derivation of Emission Probability Density. The calculation of the ensemble average velocity from equation (10) requires knowing the emission probability density,  $P(t)$ . For emission from  $i \rightarrow j$ , the probability density can be expressed as:

$$P(t) = \beta A_{i,j} N_i \quad (16)$$

where  $A_{i,j}$  is the  $i \rightarrow j$  transition rate,  $N_i$  is the number of ions in the excited state, and  $\beta$  is a proportionality constant.

The number of ions in the upper state is a function of time and is given by

$$\frac{dN_i}{dt} = -N_i \sum_j A_{i,j} \quad (17)$$

Solving for  $N_i$  yields:

$$N_i = N_{io} \exp\left(-\frac{t}{\tau}\right) \quad (18)$$

where

$$\tau = \frac{1}{\sum_j A_{i,j}} \quad (19)$$

Then the probability density may be expressed as:

$$P(t) = \beta A_{i,j} N_{io} \exp\left(-\frac{t}{\tau}\right) \quad (20)$$

The probability of emission over all time must equal 1, thus:

$$1 = \int_0^\infty P(t) dt = \int_0^\infty \beta A_{i,j} N_{io} \exp\left(-\frac{t}{\tau}\right) dt \quad (21)$$

Integrating equation (21) gives:

$$\beta A_{i,j} N_{io} = \frac{1}{\tau} \quad (22)$$

And the probability density is given as:

$$P(t) = \frac{1}{\tau} \exp\left(-\frac{t}{\tau}\right) \quad (23)$$

4. Derivation of E-scaled Doppler shift. Inserting the equations (15) and (23) into equation (10), and performing the integration yields the time average of the observed mean ion velocity:

$$\langle \mathbf{u}_r \rangle = \frac{c\Delta v}{v_o} = \frac{eE}{M\Gamma} \left[ 1 - \frac{1}{1 + \Gamma\tau} \frac{1 - \exp\left(-\frac{\lambda_q}{V\tau} - \frac{\Gamma\lambda_q}{V}\right)}{1 - \exp\left(-\frac{\lambda_q}{V\tau}\right)} \right] \quad (24)$$

Dividing both sides of equation (24) by  $c$  and  $E$  yields the *E-scaled Doppler shift*:

$$\frac{\Delta v}{v_o E} = \frac{e}{M\Gamma c} \left[ 1 - \frac{1}{1 + \Gamma\tau} \frac{1 - \exp\left(-\frac{\lambda_q}{V\tau} - \frac{\Gamma\lambda_q}{V}\right)}{1 - \exp\left(-\frac{\lambda_q}{V\tau}\right)} \right] \quad (25)$$

5. Calculation of Ion Mobility from Collision Cross-Section. Taking the steady state limit of equation (15) yields [14]:

$$\mathbf{u}_r = \mathbf{v}_d = \frac{qE}{M\Gamma} \quad (26)$$

The Wannier free-flight theory yields another expression for the drift velocity for an ion drifting in a buffer gas of mass  $m_g$  [12:121]:

$$v_d = \xi \left( \frac{1}{m_g} + \frac{1}{M} \right) \frac{eE}{NQ_v V} \quad (27)$$

where  $Q_v$  is the collision cross section for the ion/gas collision,  $m_g$  is the mass of the buffer gas, and  $\xi$  is a constant which is generally accepted to be equal to 1 for the case of a heavy ion and a light buffer gas.

Combining equations (26) and (27), and solving for  $\Gamma$  yields:

$$\Gamma = \frac{m_g}{m_g + M} NQ_v V \quad (28)$$

This disagrees with Hong and Miller, who state for a collision frequency [9]:

$$\Gamma = \sqrt{\frac{m_g}{m_g + M}} NQ_v V \quad (29)$$

With a value of  $Q_v$  determined from fitting equation (25) to experimental Doppler shift data over a range of pressure, the mobility can be determined from equations (26) and (28)

$$K = \frac{v_d}{E} = \frac{qE}{M\Gamma E} = \frac{q}{MNQ_v V} \frac{m_g + M}{m_g} \quad (30)$$

$$K = \frac{q}{\mu NQ_v V}$$

At this point it is worth mentioning the relationship and role of  $Q_v$  and  $Q_q$ . The velocity changing cross-section,  $Q_v$ , determines the steady state drift velocity of an ion. The quenching cross-section,  $Q_q$ , serves to nonradiatively depopulate the upper state of

the excited ion, and remove the ion from the sample viewed by the experiment.  $Q_q$  and  $Q_v$  are related in the sense that a quenching collision is also a velocity changing collision. If there are nonquenching velocity changing collisions, then we expect  $Q_v > Q_q$ .

## B. Theory of Fourier Transform Spectrometer

The theory of the Fourier transform spectrometer has been well explained elsewhere [15]. The following sections contain an elementary discussion of the mathematics involved in the use of a Fourier transform spectrometer in this experiment.

1. The Interferogram and its Relation to the Spectrum. The essential components of the Fourier transform spectrometer are a Michelson interferometer, a detector, and a computer for processing the signal from the detector. Figure 5 is a diagram of a Michelson interferometer with a detector at the image plane. For this discussion, we will assume an on-axis, quasi-monochromatic point source and a beamsplitter of amplitude transmittance  $t$ , and a reflectance  $r$ .

If the incident wave is of the form  $A \exp[i(\omega t - 2\pi x\sigma)]$ , where  $\omega$  and  $\sigma$  are respectively the angular frequency and wavenumber of the radiation, then the net amplitude at the image plane will be:

$$A'_{\text{det}} = A(rt) [e^{i(\omega t - 2\pi x_1\sigma)} + e^{i(\omega t - 2\pi x_2\sigma)}] \quad (31)$$

where  $x_1$  and  $x_2$  are respectively the roundtrip distances from the beamsplitter to the fixed and the movable mirror.

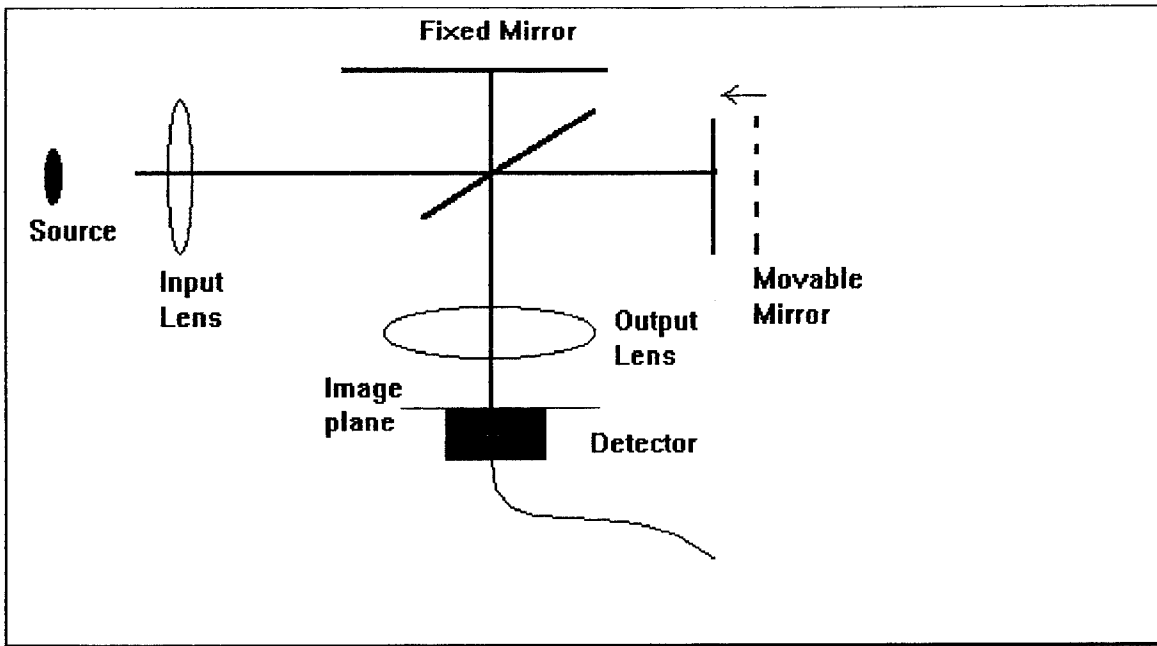


Figure 5. Michelson Interferometer

Then the energy reaching the detector is:

$$E_{\text{det}} = |A_{\text{det}}|^2 = 2A^2|rt|^2[1 + \cos(2\pi(x_1 - x_2)\sigma)] \quad (32)$$

This consists of a dc term and an ac term. The ac term is called the *interferogram*. Letting  $A^2 = B(\sigma) d\sigma$ , where  $B(\sigma)$  is the spectral density, expressing  $|rt|^2$  as  $\epsilon$ , the beamsplitter efficiency, and  $x_1 - x_2 = x$  as the path difference, then the ac part of equation (32) can be expressed as:

$$dI(x) = 2\epsilon B(\sigma) \cos(2\pi\sigma x) d\sigma \quad (33)$$

So far we have considered our source as being quasi-monochromatic. To determine the interferogram resulting from a broad spectral range, we integrate  $dI(x)$  with respect to  $\sigma$ :

$$I(x) = \int_{\sigma} dI(x) = 2\varepsilon \int_0^{\infty} B(\sigma) \cos(2\pi\sigma x) d\sigma \quad (34)$$

The interferogram is recorded as a function of the path difference  $x$ , by scanning the movable mirror over its maximum path difference. The spectral density,  $B(\sigma)$  is then recovered by performing the inverse cosine Fourier transform on  $I(x)$ :

$$B(\sigma) = \int_{-\infty}^{\infty} I(x) \cos(2\pi\sigma x) dx \quad (35)$$

2. Sampling Function. The signal received at the detector is of an analog nature. In order to be analyzed by a digital computer, an analog-to-digital conversion must take place. This can be represented by a *sampling function*,  $\Psi$  [15]:

$$\Psi(x) = \sum_{n=-\infty}^{\infty} \delta(x - n) \quad (36)$$

where  $\Psi$  is a series of delta functions at regularly spaced intervals,  $n$ .

Some identities of the sampling function are:

$$\Psi(x + m) = \Psi(x) \quad (m = \text{any integer}) \quad (37)$$

$$\Psi(ax) = \frac{1}{a} \Psi\left(x - \frac{n}{a}\right) \quad (38)$$

And the Fourier transform of  $\Psi$  is expressed as:

$$FT[\Psi(ax)] = \frac{1}{a} \Psi\left(\frac{\sigma}{a}\right) \quad (39)$$

Then an interferogram which is digitally sampled may be expressed as:

$$I'(x) = \Psi\left(\frac{x}{\Delta x}\right) \cdot I(x) \quad (40)$$

And the spectrum obtained from performing a Fourier transform on the interferogram is:

$$B'(\sigma) = (\Delta x) \Psi\left(\frac{\sigma}{\Delta \sigma}\right) * B(\sigma) \quad (41)$$

where the symbol ‘\*’ refers to the convolution of the two functions, and  $B(\sigma)$  is the ‘true’ spectrum.

3. Recovery of Spectra. In practical situations, interferogram may not be an even function of the path difference,  $x$ . In that case, the sampled interferogram will be [15]:

$$I'(x) = I(x) T(x) \Psi(x + \delta) \quad (42)$$

where  $\delta$  is the phase error in  $\Psi$ , and  $T(x)$  is the truncation function used to account for the fact that the mirror is scanned over a finite path difference, instead of the infinite path difference assumed in equation (35).

Performing a cosine Fourier transform on equation (42) yields:

$$B'(\sigma) = [B(\sigma) * t(\sigma)] e^{i\phi(\sigma)} \quad (43)$$

where  $B(\sigma)$  is the true spectrum, and  $\phi(\sigma)$  is a phase error resulting from an error in the zero path difference position in the sampling function, as well as from imperfect compensation for the beamsplitter.

The consequence of the phase errors include distortion in the spectral lines, as well as a modification of the baseline of the spectrum. Methods of elimination of the phase error are discussed below.

4. Elimination of Phase Error. If the phase function  $\phi(\sigma)$  is known, the sampled interferogram can be corrected by:

$$I''(x) = I'(x) * FT e^{-i\phi(\sigma)} \quad (44)$$

In the Bomem Fourier transform spectrometer, the phase function may be obtained by recording a low-resolution interferogram on both sides of zero path difference. The phase function is calculated from [16]:

$$\phi(\sigma) = -\arctan\left(\frac{m_i(\sigma)}{m_r(\sigma)}\right) \quad (45)$$

where  $m_i(\sigma)$  and  $m_r(\sigma)$  are respectively the imaginary and real components of the Fourier transform of the interferogram as a function of  $\sigma$ .

5. Limits of Resolution. If tilt and synchronization errors are negligible, an expression for the inherent resolution of the spectrometer may be derived [15].

The number of spectral elements may be expressed as:

$$m = \frac{\sigma_2 - \sigma_1}{\delta\sigma} \quad (46)$$

where the spectrum ranges from  $\sigma_1$  to  $\sigma_2$ , and  $\delta\sigma$  is the resolution of the spectrometer.

If the minimum resolution occurs when two nearby lines are resolved for a path difference  $L$ , boundary conditions require:

$$L = \frac{m}{\sigma} \quad \text{and} \quad L = \frac{m + 1}{\sigma + \delta\sigma} \quad (47)$$

Eliminating  $L$  from the above equation yields:

$$\delta\sigma = \frac{\sigma}{m} \quad (48)$$

Expressing  $m$  in terms of the path difference gives an order of magnitude estimate for the minimum resolution:

$$\delta\sigma \approx \frac{1}{L} \quad (49)$$

In practical situations, the minimum achievable resolution for the instrument is larger than this. Thus the resolution of the instrument may be expressed in terms of the *resolving power*,  $R = \sigma/\Delta\sigma$ , where  $R$  is given by the manufacturer, and  $\sigma$  is an average wavenumber at which the spectra is recorded.  $R$  will depend on several factors, with mechanical stability and solid angle subtended by source being dominant.

### III. Equipment and Software

#### A. Discharge Tube

The discharge tube is U- shaped (see Figure 6), and mounted upright and level, with the left pipe nearest to the spectrometer. The hollow electrodes are mounted vertically in the sidearms. The sidearms are 15 cm in length (measured from electrode surface to the near wall of horizontal section), and the horizontal section of the tube is approximately 9.5 cm in length, with an sidearm separation of about 5 cm. The inner diameter of the tube is 0.8 cm. Optical windows are mounted on the ends of the horizontal section.

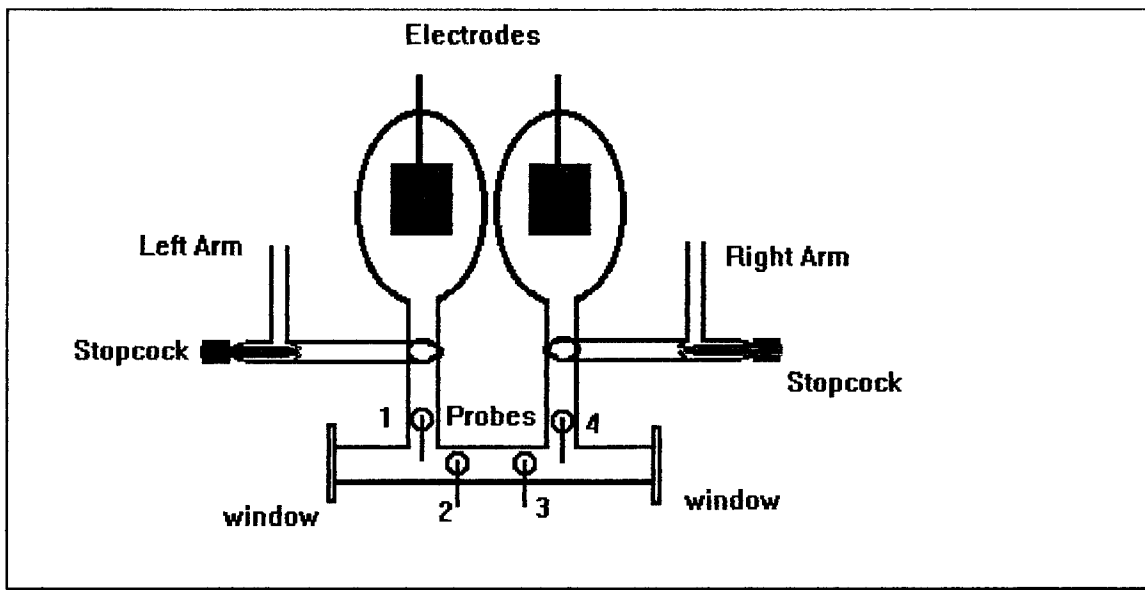


Figure 6. Discharge Tube

The hollow electrodes and mounting rods were machined from Kovar. The inner diameter of the hollow electrodes is 2.54 cm, and was hollowed to a depth of 3.810 cm. The wall thickness of the electrodes was 0.312 cm. All electrode surfaces were polished.

Four tungsten probes were inserted into the tube for measurements of the electrical potential relative to ground (see Figure 7). The joint of the probe housing with the wall was funnel-shaped, leading to a constriction. The funnel shape avoids sharp edges that would affect the boundary conditions of the plasma, while the constriction effectively reduces the surface area of the wire exposed to the plasma, eliminating the need to insulate the wire. The tips of probes in the horizontal section extended 1 mm from the wall of the tube, while the probes in the side arms extended to the center of the tube.

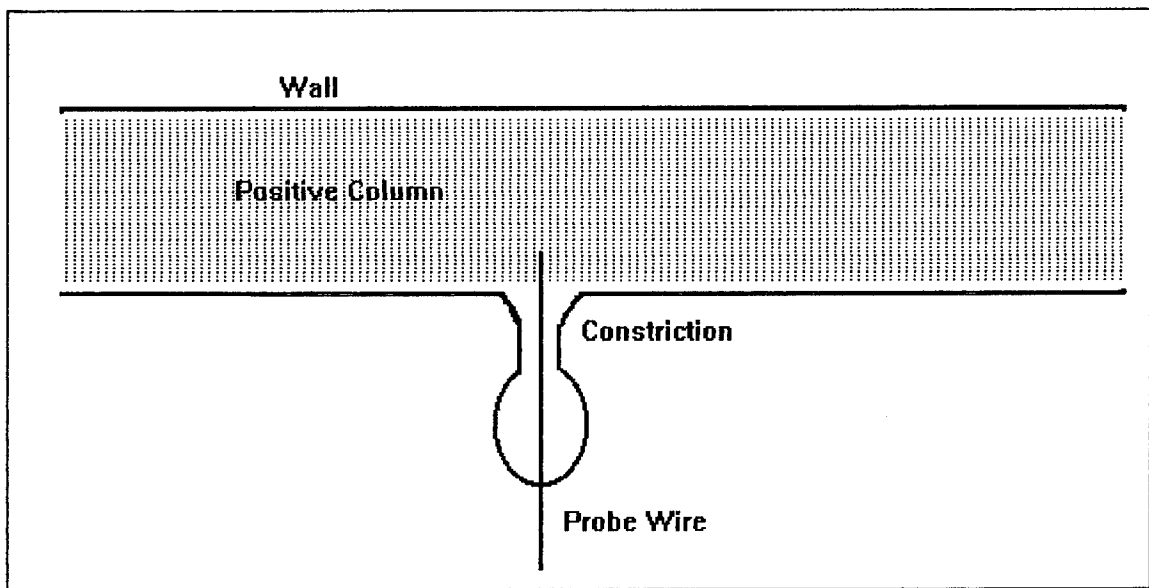


Figure 7. Probe Design

The tube was filled by flowing gas through the left pipe of the discharge tube. For the static gas fill experiments, the right pipe was sealed, and the tube was pumped out through the left pipe. For the flowing gas experiments, the gas entered the tube from the left pipe, and was pumped from the right pipe. Details on the vacuum system are included in the next section.

## B. Vacuum System (Including Flow System)

Two separate vacuum system configurations were used for this experiment. The first configuration was for a static gas fill, while the second configuration was for the flowing gas experiment.

1. Static Gas Fill. For the static gas fill configuration, a custom-built pump station was used (see Figure 8). This was an oil-free system, using an Alcatel CFV 100 turbopump, an Alcatel CFV 10 drag pump, and a KNF oil-free diaphragm pump. Butterfly valves placed at the vacuum pump ports could be used to isolate the vacuum pumps.

The connection between the pumpstation and the discharge tube was via a stainless steel bellows. The bellows was sealed to the glass tube via an O-ring. In addition, the discharge tube could be isolated from the pumpstation with a stopcock.

The gas was supplied through a manifold which could be isolated using Varian viton-sealed vacuum valves, and a needle valve at the gas bottle. Connections were available on the manifold for 1 liter glass flasks, as well as lecture bottles. Matheson research grade helium (99.9999% pure) and Spectra Gases research grade nitrogen (99.9995% pure) were used for this phase of the experiment.

Pressure was measured at the pumpstation, using a 10 torr MKS Baratron, and a 100 torr Vacuum General pressure transducer. In addition, a Granville-Phillips ion gauge was used to measure pressures  $< 10^{-4}$  torr.

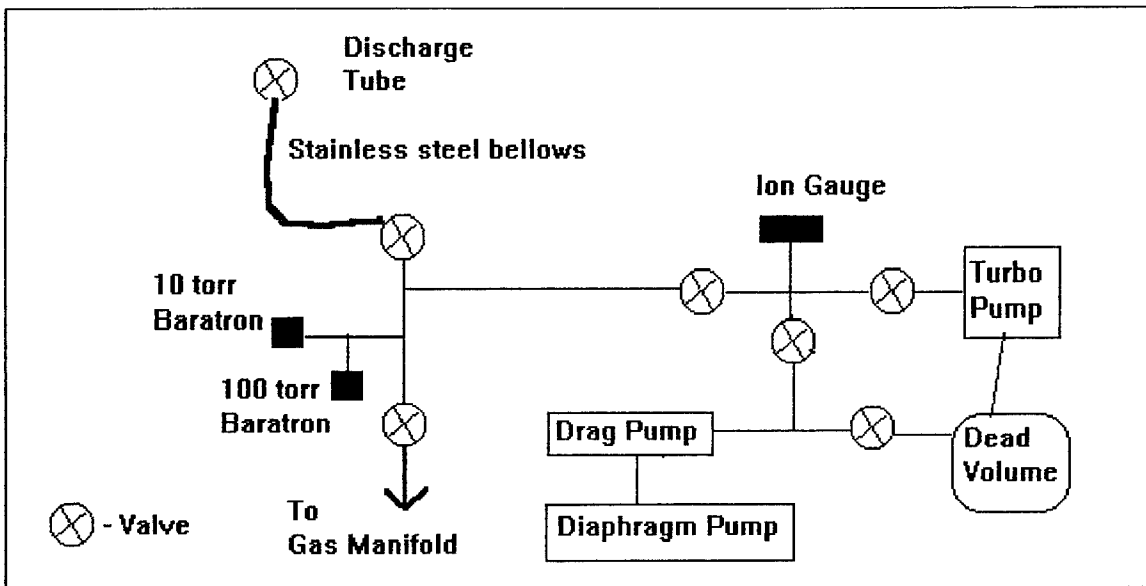


Figure 8. Static Gas Fill Vacuum System

2. Flowing Gas System. The flowing gas system can be broken down into three functions: mass flow control, pump rate control, and pumping.

The gas mass flow rate was controlled using MKS type 1259C mass flow controllers. The flow rates were set and monitored using an MKS type 247 C flow controller readout. For this portion of the experiment, Airco Grade 6 (99.9999% pure) helium and Matheson UHP (99.999% pure) nitrogen were used. Pressure was measured upstream from the discharge tube using an MKS Baratron pressure transducer.

An Alcatel 2012A mechanical pump was used for the flowing gas experiments. The pump rate was controlled by an MKS type 253A butterfly-type control valve, placed in series with the vacuum pump. The butterfly-valve was controlled by an MKS type 252A Exhaust Valve Controller, which monitored the pressure measured by the Baratron, and generated an error signal to control the butterfly-valve. The mechanical pump could be isolated with a Varian viton-sealed vacuum valve. Overnight pumpdown was

accomplished using the turbopump, drag pump, and diaphragm pump system described above.

### C. DC Discharge Power Supply.

The discharge was powered by a Glassman High Voltage DC power supply (model PS/EW10R60.0-11), operating in the current-controlled mode. The current was controlled via the setting of a potentiometer on the power supply front panel. Current regulation for this power supply is rated at better than 0.05% [17]. The accuracy of the current display is rated at  $\sim 1\%$ .

### D. Fourier-Transform Spectrometer.

A Bomem DA3.002 Fourier-transform spectrometer was used to collect the spectra. The essential features of this system are: the input optics, a Michelson interferometer, a detector, and a vector processor (see Figure 9).

The input optics consist of the collection optics, an adjustable iris aperture, and a collimator. The collection optics are used to focus an image of the source onto the iris aperture. The collection optics consist of a lens, a flat steering mirror, and an off-axis paraboloid mirror. The focal length of the lens was approximately 13 cm, and the focal length of the paraboloid mirror was 12.8 cm. This resulted in a magnification of the image of the tube on the input aperture of approximately 1:1.

The iris aperture is the independent factor determining the resolving power of this spectrometer, as it limits the solid angle subtended by the source. The aperture was manually set by closing the iris around a 1 mm gauge. Using an equation supplied by the manufacturer, the resolving power is limited to  $4.2 \times 10^5$  for an aperture diameter of 1 mm.

The Michelson interferometer was used to generate the interferograms, from which the spectra could be obtained. The maximum path difference for this model was 250 cm. The mirrors were dynamically aligned, using electronic tilt correction, resulting in less than 1  $\mu$ radian rms tilt error over the full travel of the moving mirror. The velocity accuracy of the moving mirror is rated at  $\pm 0.5\%$ , with a uniformity of  $\pm 2\%$  or  $\pm 0.002$  cm/sec (whichever is greater).

A single mode, thermally stabilized He-Ne laser, operating at 632.8 nm, was coaxially aligned with the input beam of the interferometer. The interferogram of the laser is nearly a cosine wave, and is used to produce sample pulses to trigger the analog to digital conversion of the interferogram. In normal operation, a removable mask is placed to block the output of the laser to the detector. This mask was removed for this experiment to allow light propagating along the axis to reach the detector. The light from the laser was blocked from the detector using a narrowband filter.

In addition to the He-Ne laser, a broadband white-light source is coaxially aligned with the input beam. The purpose of the white-light source is to produce a strong signal

at zero-path difference (determining its location), which then allows interferograms from multiple successive scans to be co-added.

The detector was an R928 photomultiplier (PMT), manufactured by Hamamatsu [18]. It has a nine-stage, circular-cage design. The input window material is UV glass, and the photocathode material is multialkali. The R928 has a spectral range of 285-900 nm with a peak wavelength at 400 nm.

The voltage signal from the detector is converted from analog to digital, and stored in the vector processor. The vector processor co-adds interferograms from successive scans of interferometer. At the completion of the scans, the vector processor performs a fast-Fourier transform (FFT) on the interferogram to obtain the spectrum. The resulting spectrum and interferogram are sent over a local network to a VAX computer.

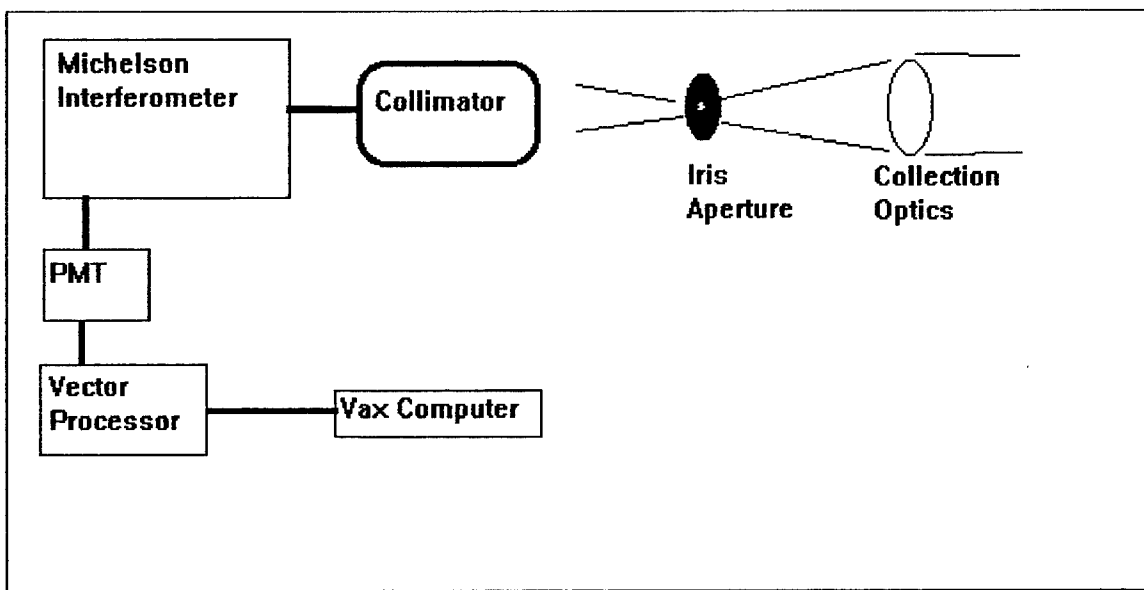


Figure 9. Schematic of Fourier Transform Spectrometer

#### E. Electric Field Measurement System.

As described in section A of this chapter, tungsten probes were used to measure the electric potential relative to ground at four locations in the positive column. Voltages were recorded by an automated system (see Figure 10), consisting of two Fluke model 80K-40 HV 1000:1 voltage reduction probes. The resistance of the Fluke probes was  $1000\text{ M}\Omega$ , (a high resistance being essential to minimize current drawn from the discharge). The probe voltages were measured with two HP3478A multimeters. The voltage data was sampled with a HP9836C computer which acquired the data over an IEEE interface. The computer used a program written in BASIC to compute the mean and standard deviation of the voltage.

The distances from the left electrode to each tungsten probe were measured prior to the experiment, allowing the electric field to be determined from the slope of the voltage plotted as a function of distance.

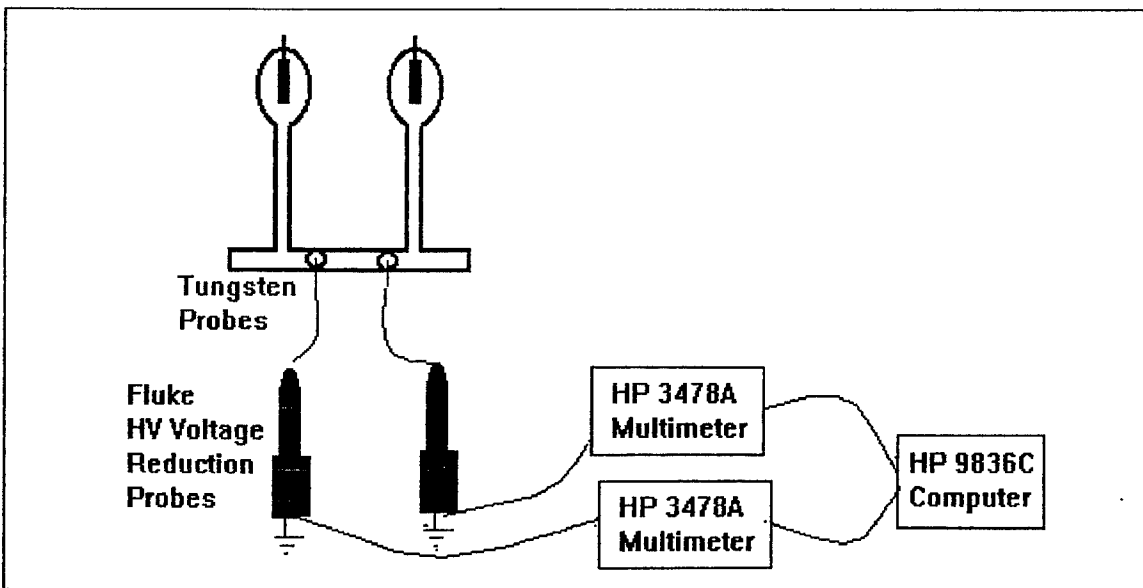


Figure 10. Electric Field Measurement System

#### F. Peak Picking Programs.

Two routines were used and compared for determining peak intensity wavelengths for the spectra. The first routine is BOMFIT, developed in-house at Wright Laboratory. BOMFIT uses a least-squares approach to fit Doppler lineshapes to the data, using line position and temperature as adjustable parameters (instrument lineshape also factored into the fit). The routine used the Levenberg-Marquardt method to vary the parameters until the least-squares error between the calculated lineshape and the experimental lineshape was minimized. Data output from the program include line positions, line intensities, and temperature.

The second routine used for peak finding was the differential peak finding function included with the Bomem spectrometer software. This function numerically differentiates the spectrum. Sharp oscillations in the differentiated spectrum correspond to line positions. A threshold level is set using a cursor, and peaks are assigned to wavenumbers where the oscillation exceeds the threshold level.

The performance of the two systems was comparable. BOMFIT showed better performance in noisy regions of the spectrum. The least-squares method may have been more immune to noise than the differential method. In addition, BOMFIT yielded values for the ion temperatures.

## IV. Procedure

### A. Measurement of Tube Dimensions

Prior to mounting the discharge tube, the tube dimensions were measured using a metric tape measure. The dimensions of the tube that were measured included tube diameter, length of horizontal section, side arm length, side arm separation, probe location, and probe separation.

For each dimension, nine measurements were taken, and a mean computed. The error in the measurement was taken to be 1mm or the standard deviation (whichever was greater).

The distance between the tungsten probes and the left electrode was defined to be the length of the line running along the axis of the tube from the electrode lip to the probe. This approximation will tend to overestimate the probe distance, but for long distances, the error is small.

### B. Calibration of FTS System: Phase File

As mentioned in the theory section, determination of the phase function of a spectrometer allows compensation for phase errors in the spectra. The phase function was obtained by recording the interferogram of a broadband lamp on both sides of the ZPD location of the moving mirror. The spectrometer software computes the sine and cosine

Fourier transforms from the interferogram, and produces the phase function using equation (45).

### C. Alignment of Discharge Tube

The tube was mounted on an X-Y translation stage with vertical and rotational adjustments. Alignment of the optical system was done using a three separate tests. The first test was to align the image on the front and rear windows, produced by backlighting the spectrometer with a white light source (see Figure 11). The image sizes and locations on the front and back windows of the discharge tube were obtained using a white index card. The tube orientation was adjusted such that the white light image was centered on both the front and back windows, with the front and back images being of equal size.

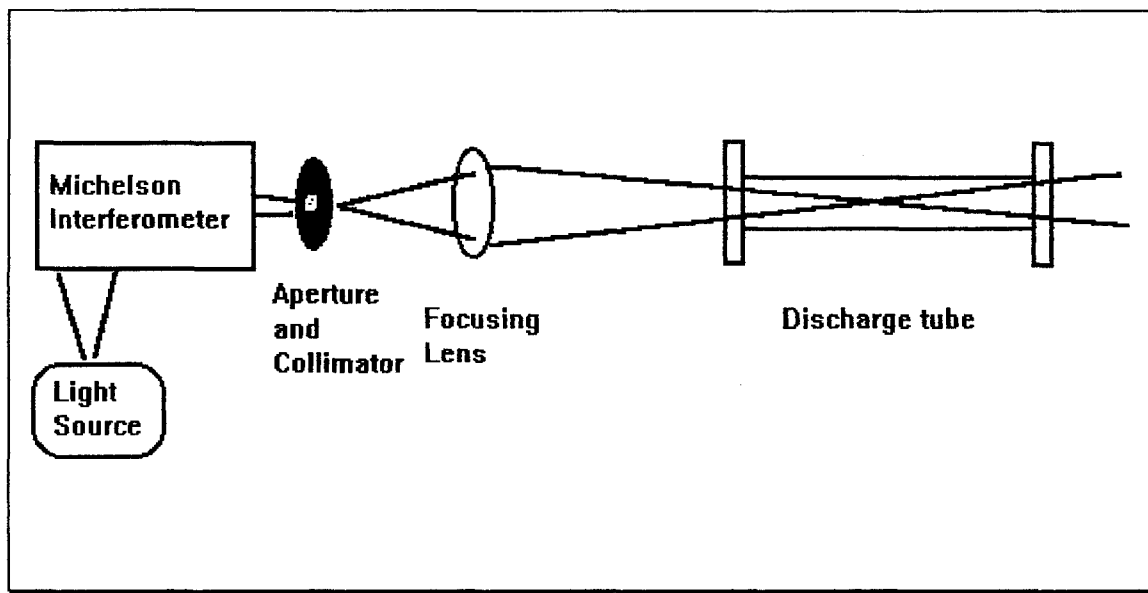


Figure 11. Backlight Alignment Technique

The second alignment test was to turn on the discharge, and observe its image on the spectrometer aperture. Proper alignment is indicated by having the pupil of the aperture in the center of the image of the discharge tube.

The third alignment test is performed using the spectrometer's co-axial He-Ne laser alignment beam. The interferometer reflects a portion of the laser beam out the spectrometer aperture. As this beam is used for aligning the spectrometer, it can be used to check the alignment of the tube. This is not a precise test, as the He-Ne laser is not precisely co-axial with optical axis, but instead is parallel to the axis. However, it is useful for detecting gross misalignments of the tube.

#### D. Acquisition of Spectra

The initial step in the acquisition of spectra is preparation of the gas mix. For the static fill case, the sequence begins by pumping the discharge tube until it reaches a base pressure  $< 10^{-6}$  torr. The vacuum pump and discharge tube are isolated from the rest of the vacuum system while the gases are premixed at the pumpstation. Gases are premixed using the law of partial pressures to determine the ratio of N<sub>2</sub> to He. After premixing, the valve to the discharge tube is opened, and the gas mix enters the discharge tube. The final pressure is read with the Baratron at the pumpstation. The ratio of the pressure in the isolated pumpstation to the final pressure is a constant, and can be used to compute the necessary pressure during premix to obtain a desired pressure in the discharge tube.

For the flowing gas case, the sequence begins with setting the flow setpoints of the flow controllers and the pressure setpoint of the exhaust valve controller. Next, the flow controllers are filled with gas, and after a warmup period, the flow controllers are zeroed. Then the turbopump, drag pump, and diaphragm pump are isolated from the pumpstation. Gas flow is initiated at this point, and after the pressure rises above 1 torr, the valve to the mechanical pump is opened.

The mass flow parameters were set to maintain a constant residence time of 0.026 seconds for the pressure range over which this experiment was performed. The limiting factors were the resolution of the 20 sccm flow controller, and the pump rate through the discharge tube. This limited our experimental conditions to pressures above 0.5 torr and 0.08 sccm of N<sub>2</sub>. The flow rate of He was adjusted accordingly to achieve the desired total pressure in the tube, yet maintain the constant residence time.

Preparations are made to make voltage measurements (see section F, this chapter), the power supply is connected to the anode of the discharge tube, and the cathode is connected to ground. The power supply is turned on, initiating the discharge, and the current level is set using the potentiometer on the front panel. The voltage on the PMT is adjusted such that the analog to digital converter on the spectrometer will read between 15% and 80% of the scale.

At this point, the menu driven Bomem software is used to control the acquisition of spectra. The operator selects the desired resolution and the number of scans taken by the interferometer. In this experiment, at least nine scans were recorded and co-added to generate the interferograms for every reported spectrum. In most cases sixteen scans

were recorded. The desired resolution was set at  $0.06\text{ cm}^{-1}$  for all reported spectra. The time necessary to obtain a spectra under these conditions was approximately 40 minutes.

### E. Determination of Ion Temperatures

The ion translational and rotational temperatures of the  $\text{N}_2^+$  ion were determined from the spectra. The translational temperature was obtained from the BOMFIT software, which fit Doppler line shapes to the lines in the observed spectra, with temperature being one of the parameters.

The rotational temperature can be determined from [19:126]:

$$I_{\text{em}} = \frac{C_{\text{em}} v^4}{Q_r} (J' + J'' + 1) \exp[-BJ'(J' + 1)hc / kT] \quad (50)$$

where  $I_{\text{em}}$  is the emission intensity,  $C_{\text{em}}$  is depends on the change in dipole moment and the total number of molecules in the initial vibrational level,  $B$  is the fundamental molecular rotational constant for  $\text{N}_2^+$ ,  $Q_r$  is the sum of the Boltzmann factors over all of the rotational states, and  $J'$  and  $J''$  are the rotational quantum numbers for the transition.

In practice, these terms have been previously calculated [20] giving a new fitting equation of:

$$I_{\text{em}} = \frac{LT}{T_{\text{rot}}} \text{Exp}\left[-ET/T_{\text{rot}}\right] \quad (51)$$

where LT and ET are respectively the linear and exponential terms that correspond to a particular line in the spectra, and  $T_{\text{rot}}$  is the rotational temperature. At this point, the rotational temperature is found by performing a least-squares fit.

#### F. Voltage Measurements

At the beginning of a laboratory session, the HP9836C computer was loaded with the voltage data acquisition program, and given an initial time/date setting. Prior to recording a spectra, tungsten probes 1 and 4 (located in the sidearms) were connected to the Fluke HV voltage probes. After the discharge was initiated, the voltage was sampled at the two probe locations. When the spectrometer finished scanning, voltages at probes 1 and 4 were sampled again and checked against the initial reading for drift. The power to the discharge was disconnected, and the tube was grounded for safety. The Fluke voltage probes were then connected to tungsten probes 2 and 3 (in the horizontal section). The power to the discharge was turned on, and the voltages were sampled at probes 2 and 4. For each probe voltage measurement, the voltage was sampled 256 times over period of approximately two minutes.

## V. Results and Analysis

### A. Data

#### 1. Static Gas Fill

Electric Field. The axial electric field was measured using probes, as discussed previously. At low current (1 mA), the measured field shows poor agreement with Hong and Miller (see Figure 12), especially at low pressure, and diverges from Saykally's measurement at 6 torr. The trend is essentially a flat line, showing no pressure dependence for the electric field.

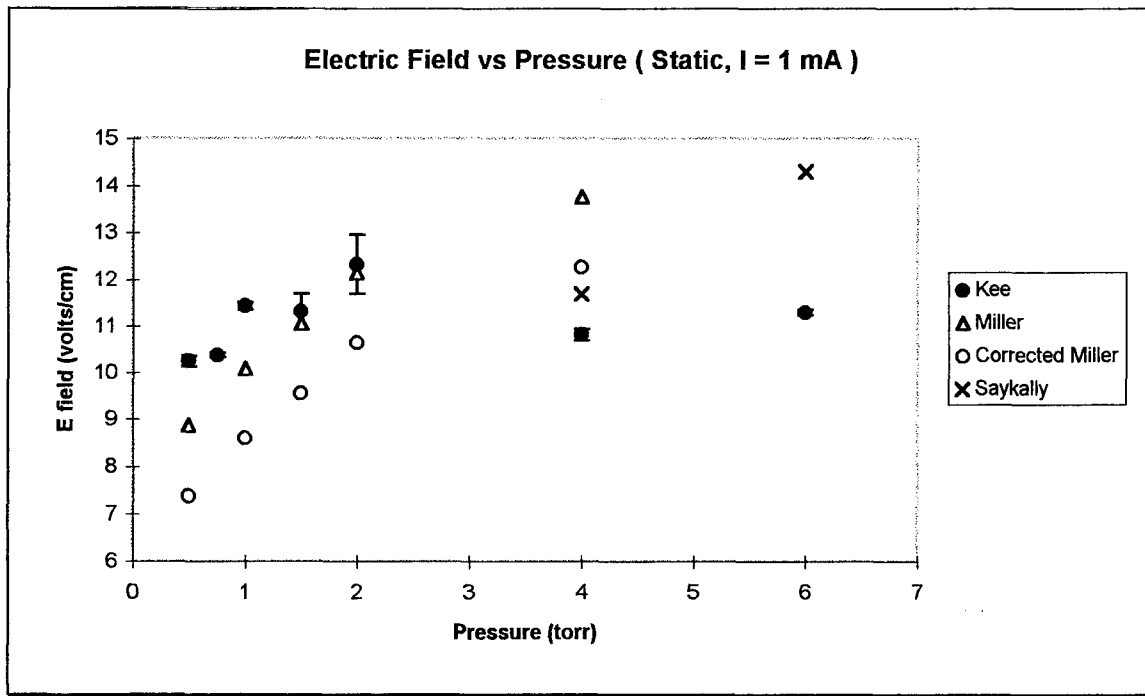


Figure 12.  $E$  vs  $P$ , Static Fill,  $I = 1$  mA

The electric field plot changes considerably as the discharge current is increased to 5 mA (see Figure 13). At pressures  $< 3$  torr, the measured field agrees with the values

obtained by Hong and Miller using probes, and parallels their corrected field values. However, at pressures  $> 3$  torr, the measured field is close to both the Hong and Miller corrected field, as well as Radunsky and Saykally's value obtained from velocity-modulation laser absorption spectroscopy [7].

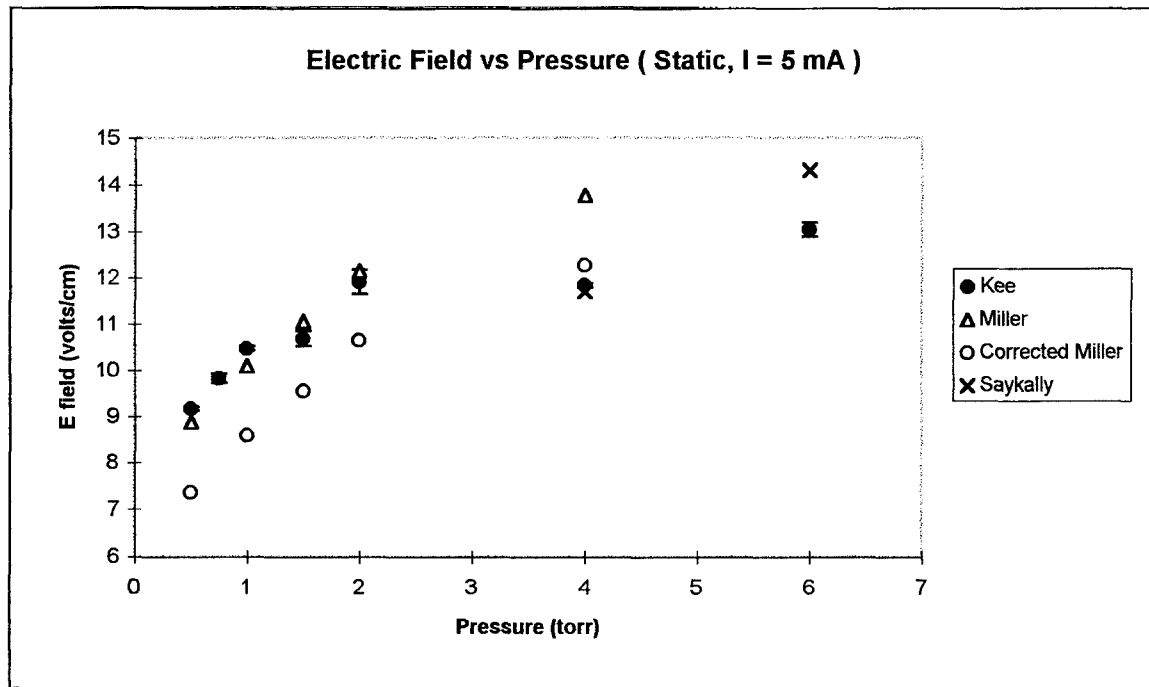


Figure 13.  $E$  vs  $P$ , Static Fill,  $I = 5$  mA

Similar behavior occurs at 10 mA. The trend is to follow the uncorrected Hong and Miller data at low pressures, and agree with their corrected data, and with Saykally at higher pressures. The cross-over point for this behavior appears to be  $\sim 1.5$  torr.

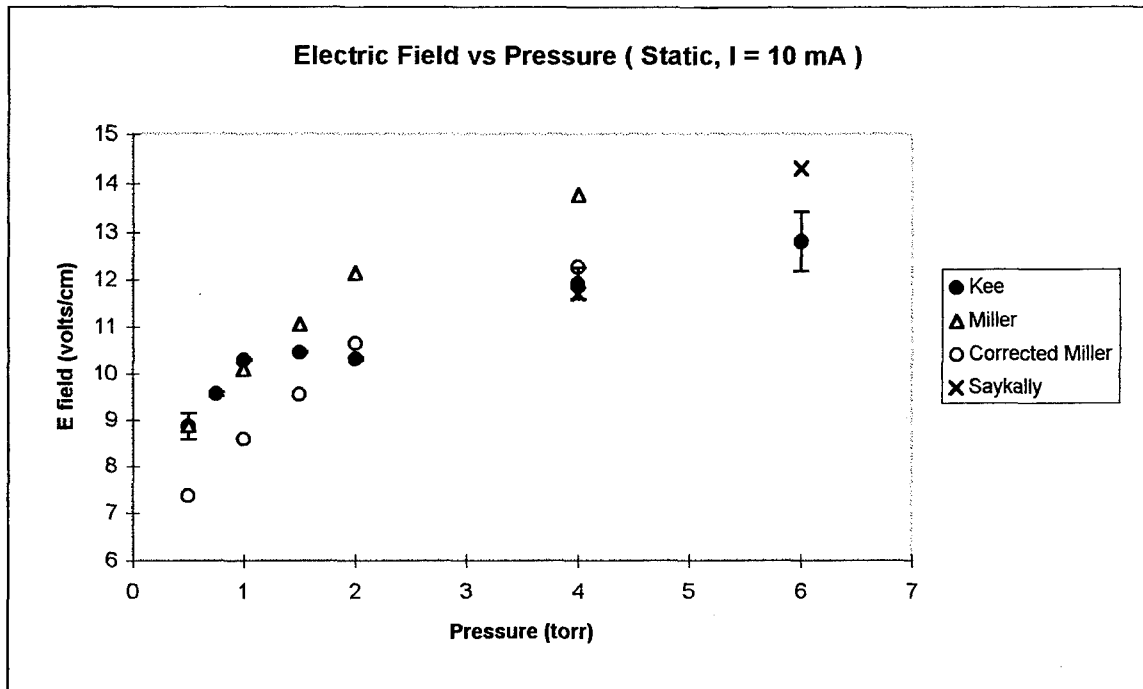


Figure 14.  $E$  vs  $P$ , Static Fill,  $I = 10$  mA

Doppler Shift. In the case of the static gas fill, the measured Doppler shift differed considerably from that obtained by Hong and Miller (see Figures 15, 16 and 17). The measured shift is slightly lower than the Hong and Miller data at low pressures, but diverges widely at higher pressures. The measured peak Doppler shift occurs at  $\sim 1$  torr, in comparison to  $\sim 2$  torr for Hong and Miller.

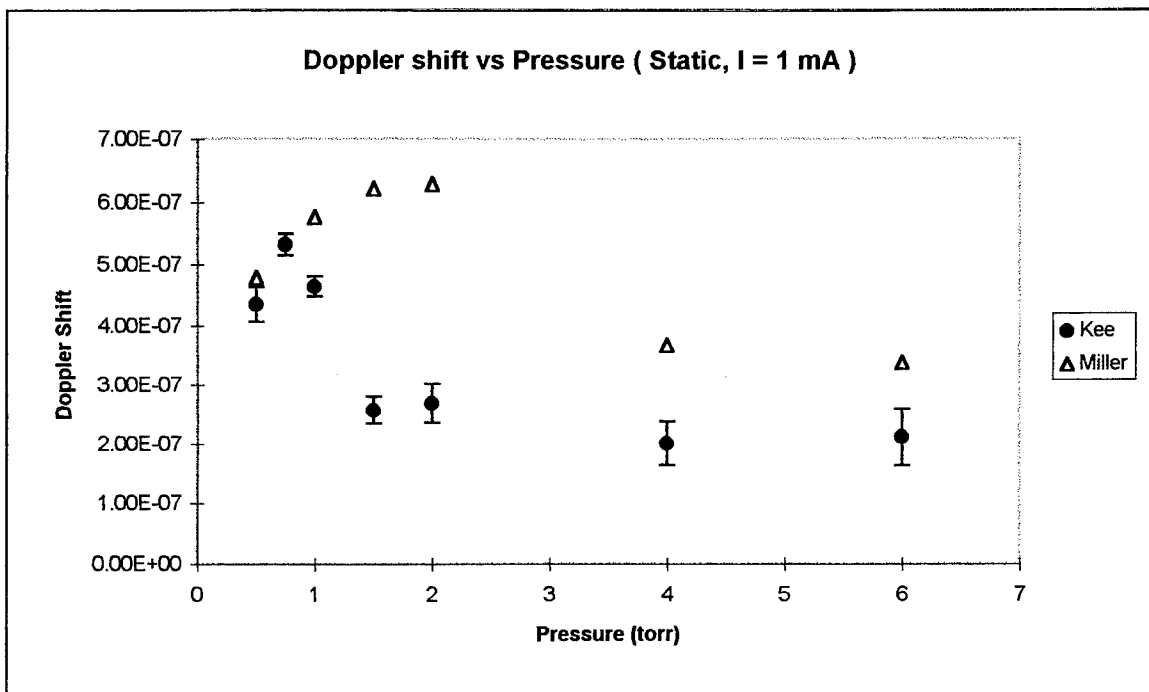


Figure 15. Doppler Shift vs Pressure, Static Fill,  $I = 1 \text{ mA}$

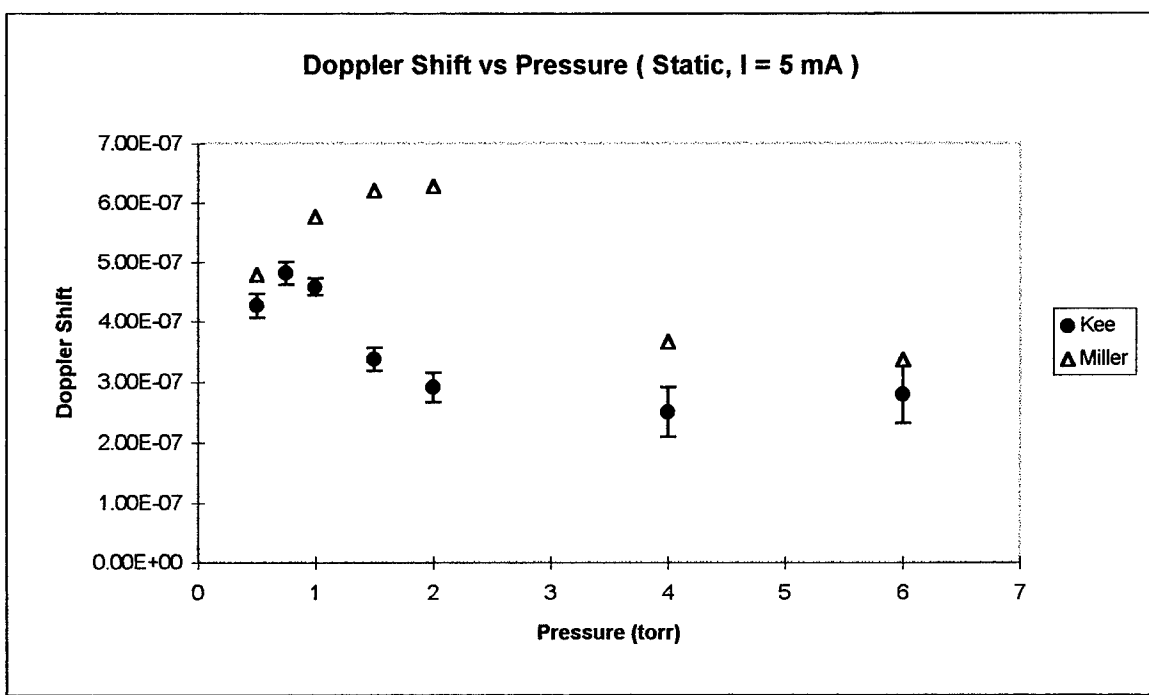


Figure 16. Doppler Shift vs Pressure, Static Fill,  $I = 5 \text{ mA}$

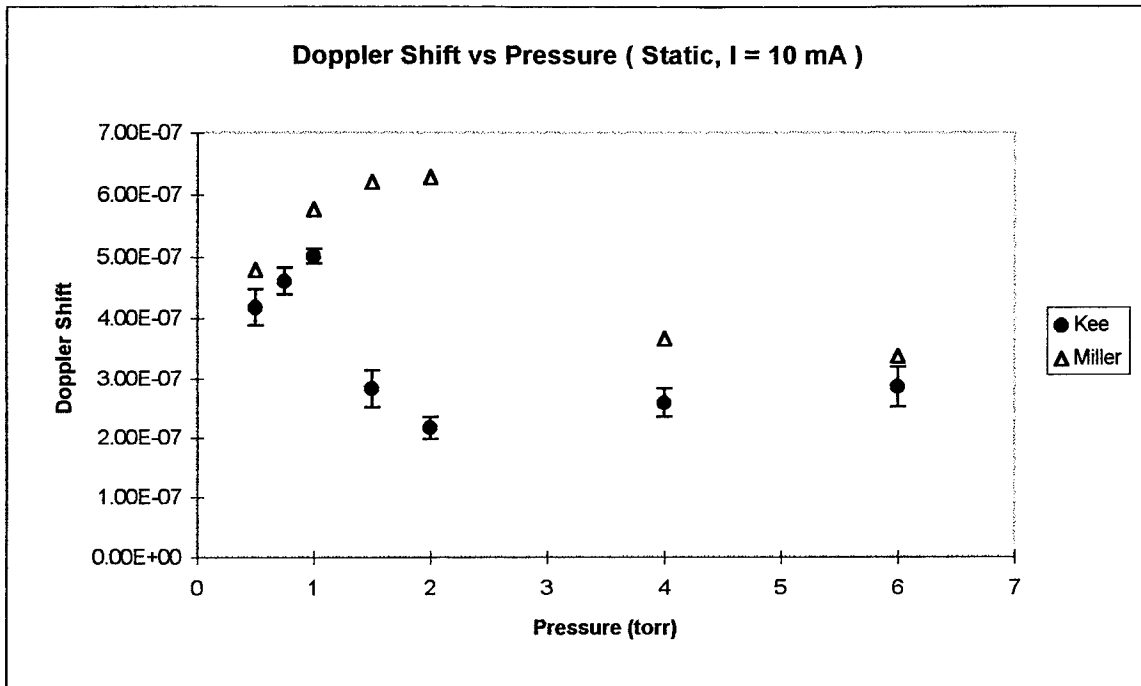


Figure 17. Doppler Shift vs Pressure, Static Fill,  $I = 10 \text{ mA}$

Temperature. The measured  $\text{N}_2^+$  rotational and translational temperatures are given in Figures 18, 19, and 20. The temperatures appear to be independent of pressure and electrode orientation. The rotational temperature shows a moderate level of dispersion at a discharge current of 1 mA, with the dispersion tightening as the discharge current is increased. Both the rotational and translational temperatures increase with the discharge current (see Figure 21), but the functional dependence of the increase cannot be determined from the three data points from this experiment, and the data point reported by Radunsky and Saykally [21].

One notable feature of these plots is the  $\sim 200 \text{ K}$  difference in the translational and the rotational temperatures, implying nonequilibrium between the translational and rotational energies. Similar observations were reported by Radunsky and Saykally, who

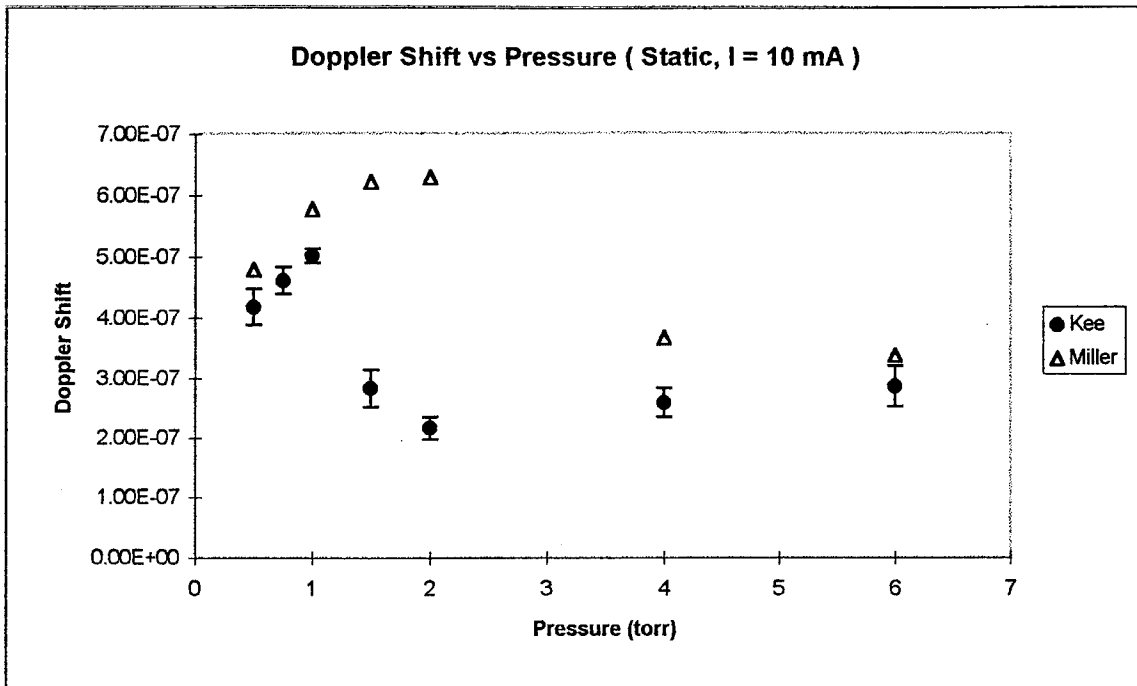


Figure 17. Doppler Shift vs Pressure, Static Fill,  $I = 10 \text{ mA}$

Temperature. The measured  $\text{N}_2^+$  rotational and translational temperatures are given in Figures 18, 19, and 20. The temperatures appear to be independent of pressure and electrode orientation. The rotational temperature shows a moderate level of dispersion at a discharge current of 1 mA, with the dispersion tightening as the discharge current is increased. Both the rotational and translational temperatures increase with the discharge current (see Figure 21), but the functional dependence of the increase cannot be determined from the three data points from this experiment, and the data point reported by Radunsky and Saykally [21].

One notable feature of these plots is the  $\sim 200 \text{ K}$  difference in the translational and the rotational temperatures, implying nonequilibrium between the translational and rotational energies. Similar observations were reported by Radunsky and Saykally, who

reported a translational temperature of 1200 K and a rotational temperature of 412 K for a discharge current of 120 mA [21].

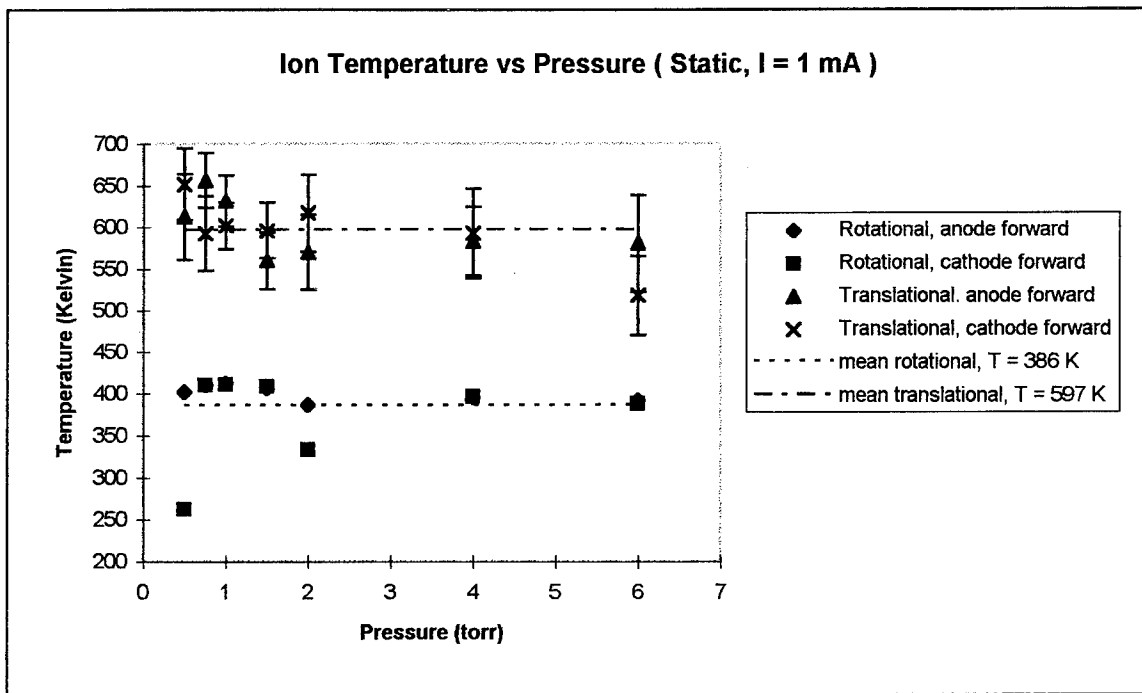


Figure 18. Ion Temperature vs Pressure, Static Fill,  $I = 1$  mA

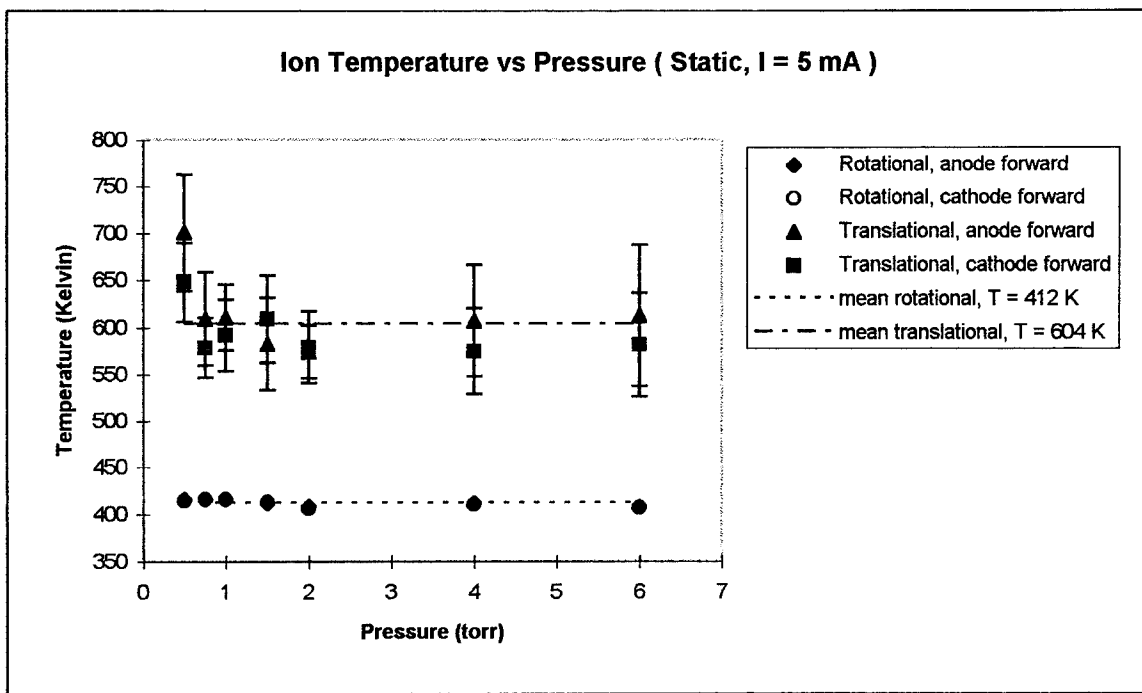


Figure 19. Ion Temperature vs Pressure, Static Fill,  $I = 5$  mA

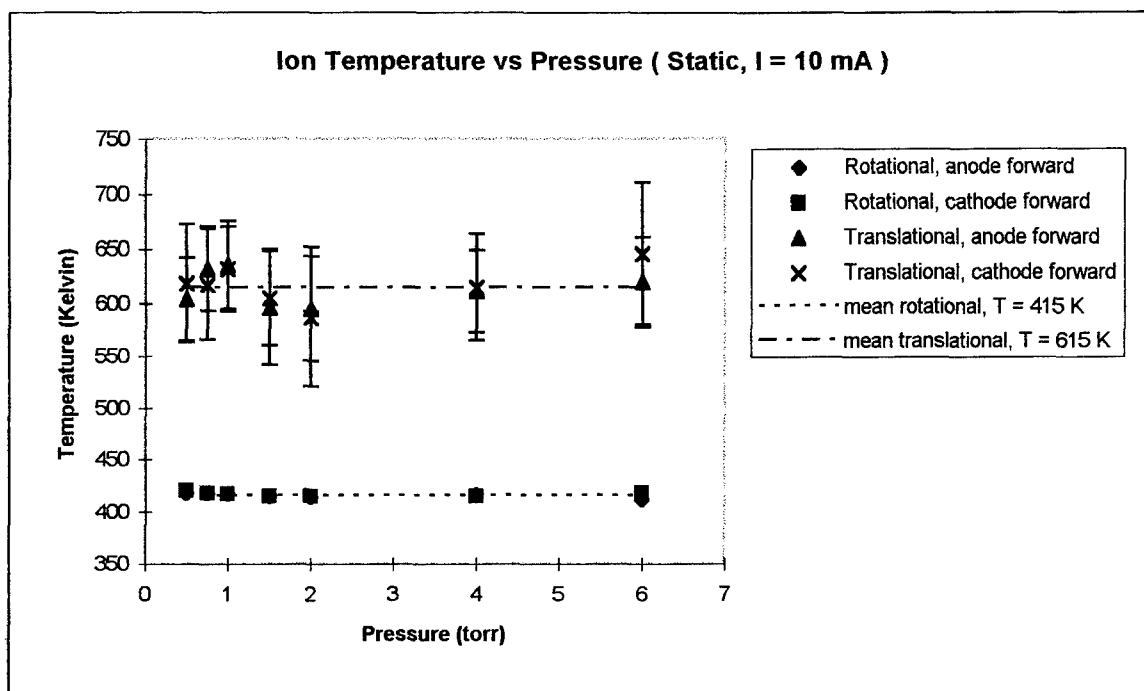


Figure 20. Ion Temperature vs Pressure, Static Fill,  $I = 10 \text{ mA}$

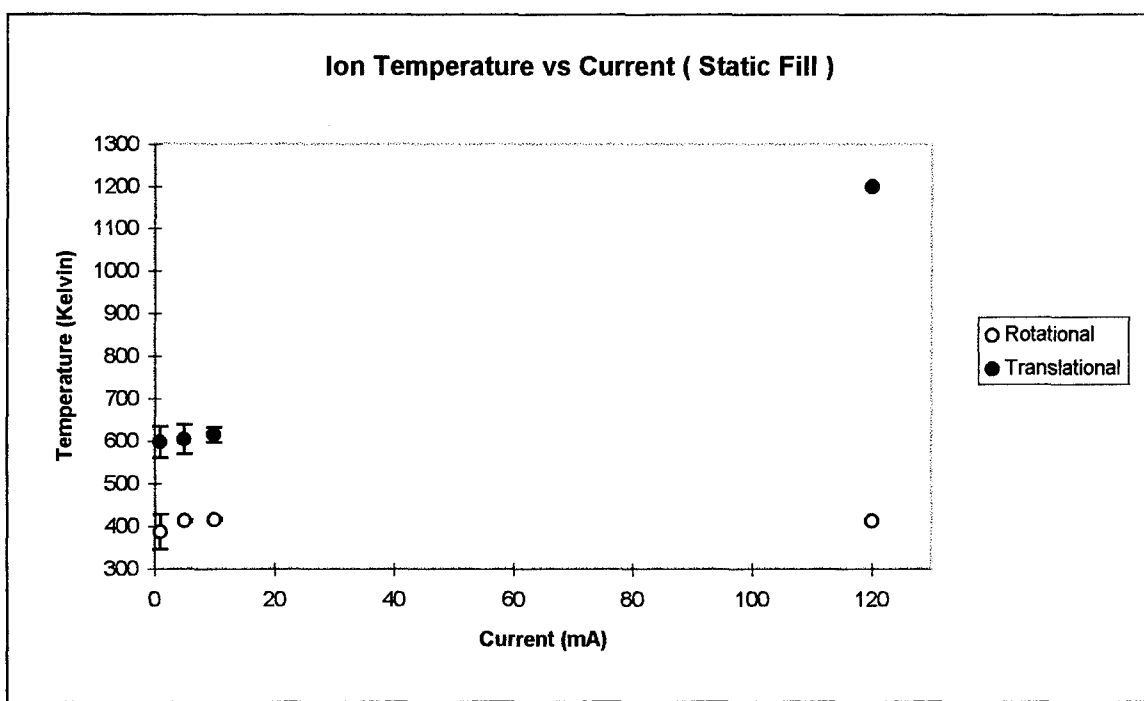


Figure 21. Ion Temperature vs Current, Static Fill

## 2. Flowing Gas

Electric Field. The measured electric field at 1mA discharge current with a flowing gas differs considerably from the case of the static gas fill (see Figures 12 and 22). Comparing the two, the static gas fill displayed essentially no dependence of the E field due to pressure, whereas in the case of the flowing gas, the electric field is pressure dependent. It is observed that the measured field closely follows the uncorrected Hong and Miller data at low pressures, and parallels their corrected data. At higher pressure, the measured field agrees with Radunsky and Saykally, and the corrected Hong and Miller data. The cross-over point for the behavior is  $\sim 1.5$  torr.

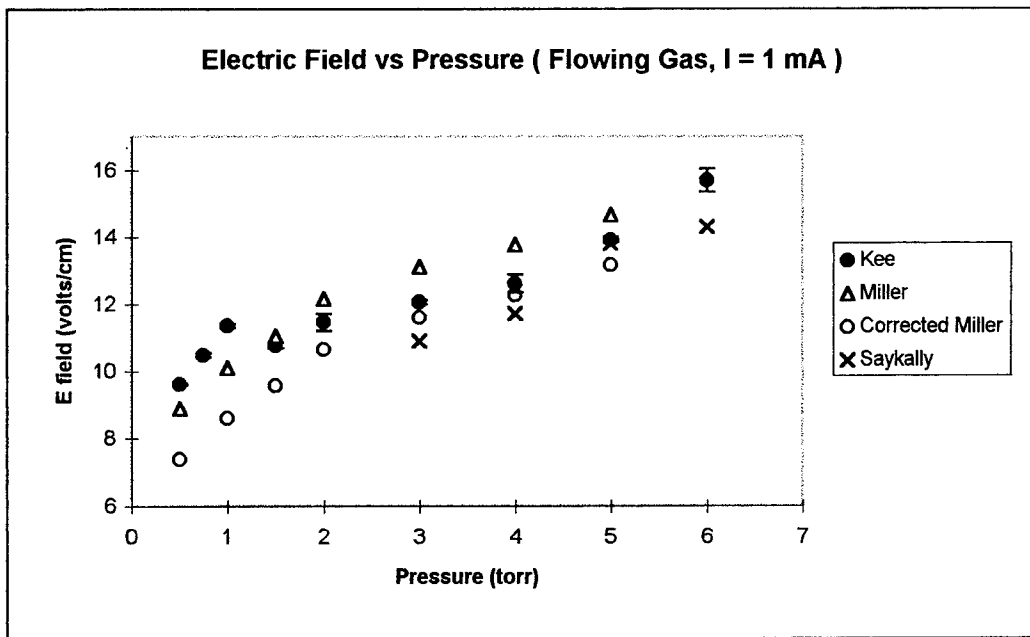


Figure 22.  $E$  vs  $P$ , Flowing Gas,  $I = 1$  mA

At discharge currents of 5 and 10 mA, the electric field displays similar behavior to the measurements taken at 1 mA (see Figures 23 and 24).

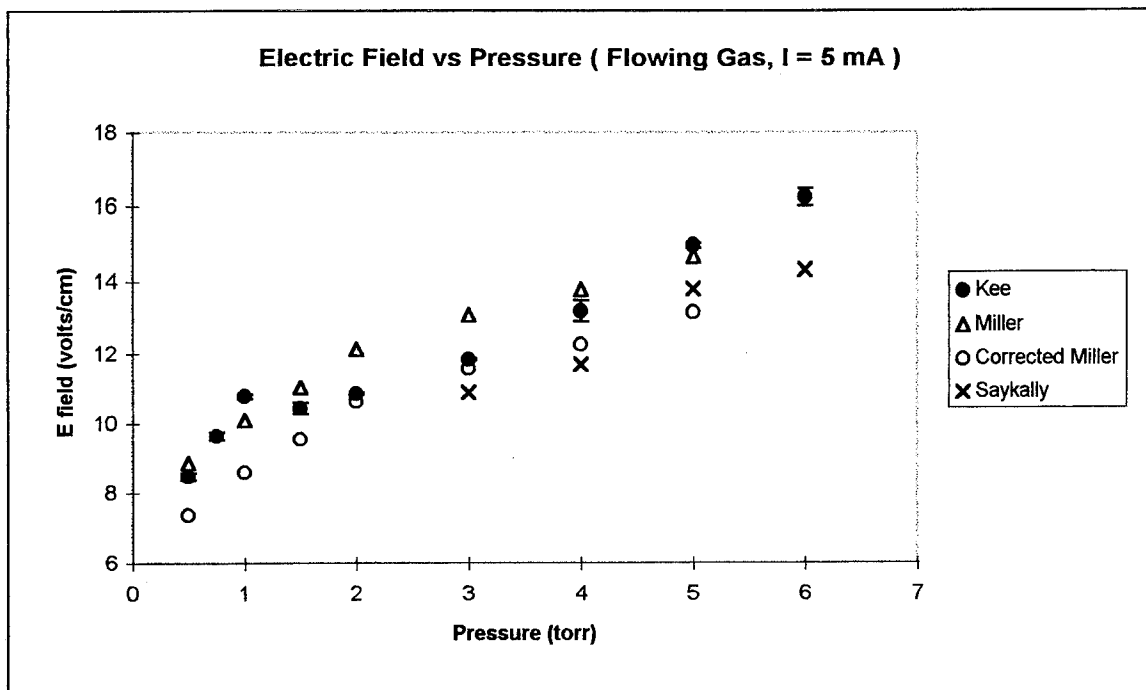


Figure 23.  $E$  vs  $P$ , Flowing Gas,  $I = 5$  mA

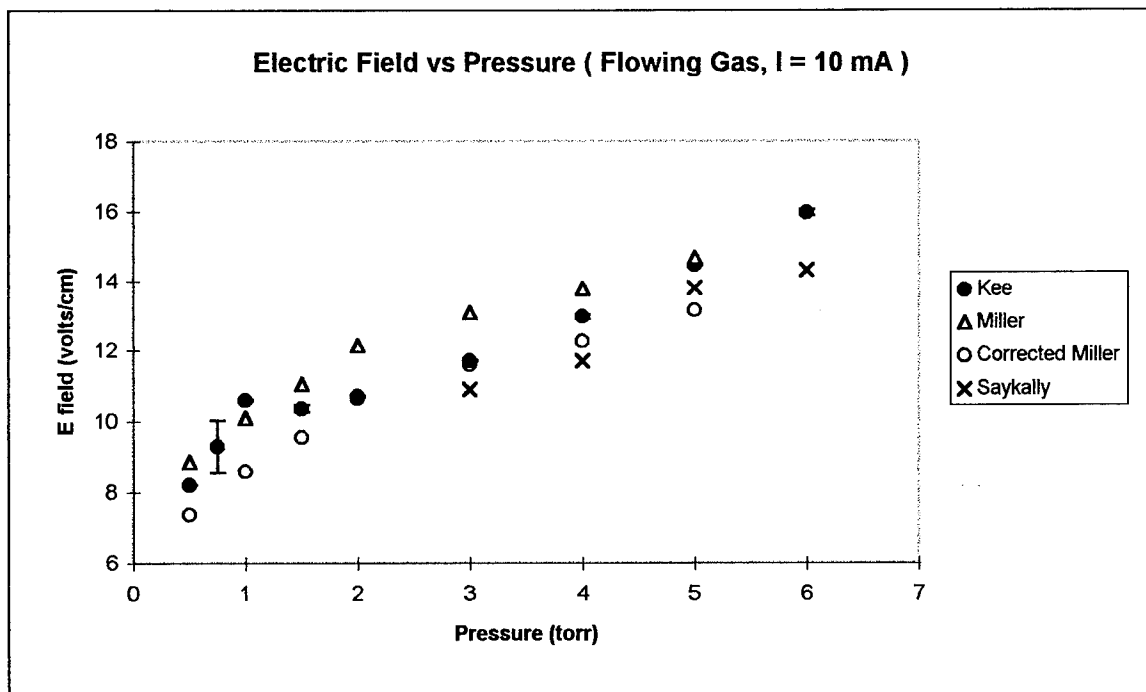


Figure 24.  $E$  vs  $P$ , Flowing Gas,  $I = 10$  mA

Doppler Shift. In the case of the flowing gas, the measured Doppler shift showed similar behavior to the case of the static gas fill. At low pressures, the size of the shift was lower than the Hong and Miller data. At pressures between  $\sim 0.75$  to  $\sim 5$  torr, the shift values diverge, until at higher pressures, they agree. The peak value of the Doppler shift occurred at  $\sim 0.75$  torr for discharge currents of 5 and 10 mA, in comparison to  $\sim 2$  torr for Hong and Miller. The highest value of the Doppler shift at 1 mA occurred at the lowest pressure, 0.5 torr.

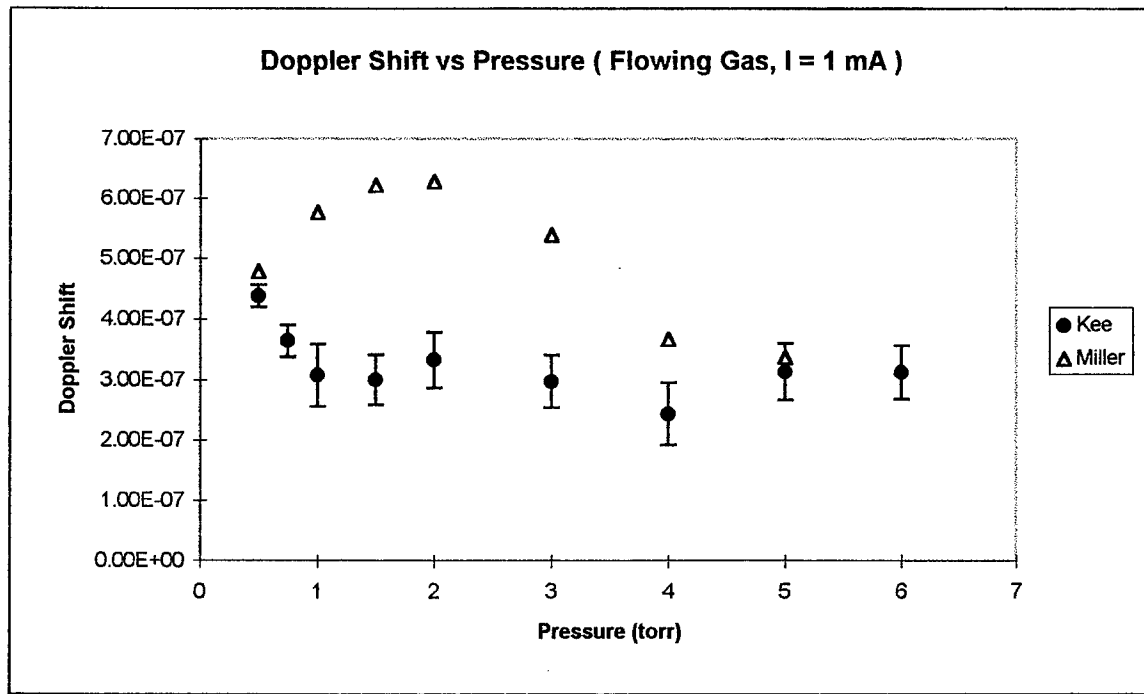


Figure 25. Doppler Shift vs Pressure, Flowing Gas,  $I = 1$  mA

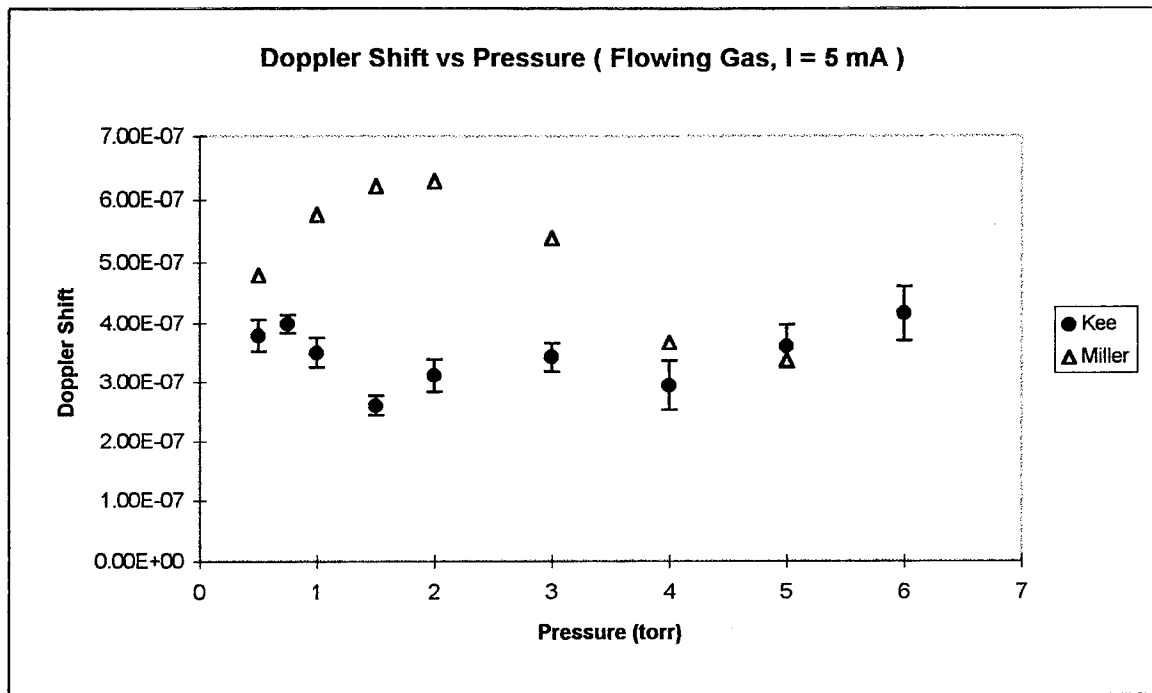


Figure 26. Doppler Shift vs Pressure, Flowing Gas, I = 5 mA

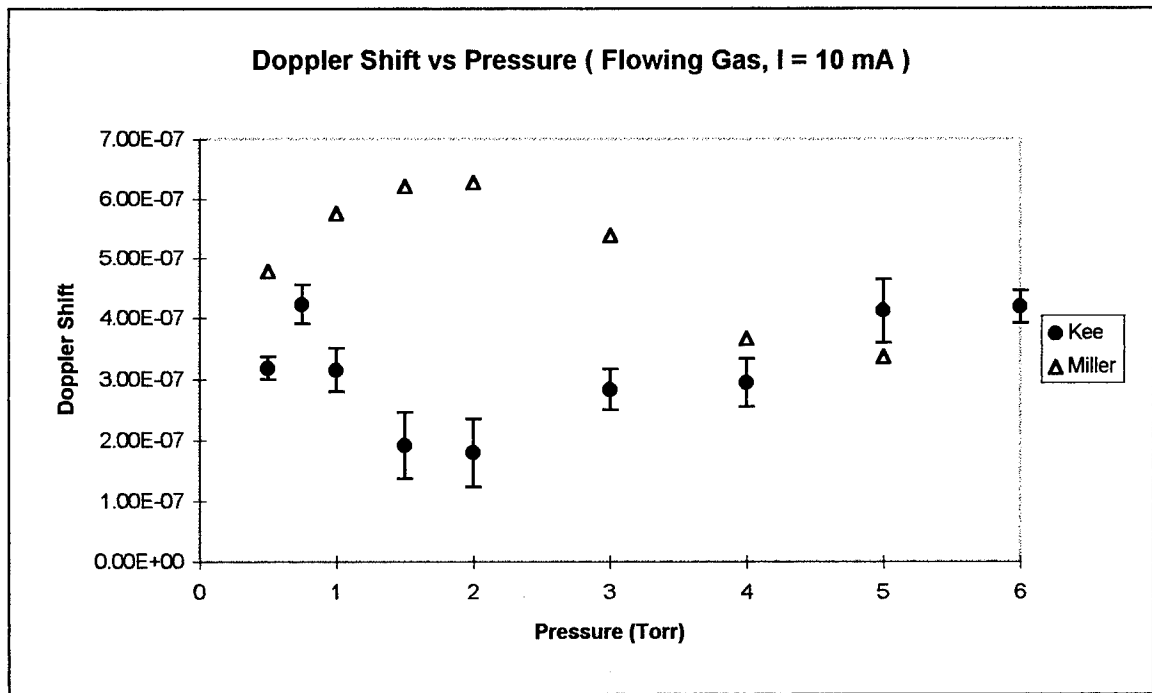


Figure 27. Doppler Shift vs Pressure, Flowing Gas, I = 10 mA

Temperature. The  $\text{N}_2^+$  rotational and translational temperatures are given in Figures 28, 29, and 30 for the case of flowing gas. Significant differences are observed in

comparison to the static gas fill. The mean rotational temperatures are lower for the flowing gas than for the static gas fill. This is to be expected, as residence time of the flowing gas is short ( $\sim 0.026$  sec), and thus the flowing gas can be expected to stay at room temperature. In contrast, the mean translational temperatures are slightly higher for the flowing gas than for the static gas fill.

The rotational temperatures show a wide dispersal at a discharge current of 1 mA, with some of the data points being below room temperature. This is attributed to low signal-to-noise of the spectra. This dispersal is sharply reduced as the discharge current is increased. Similar behavior is observed for the translational temperature.

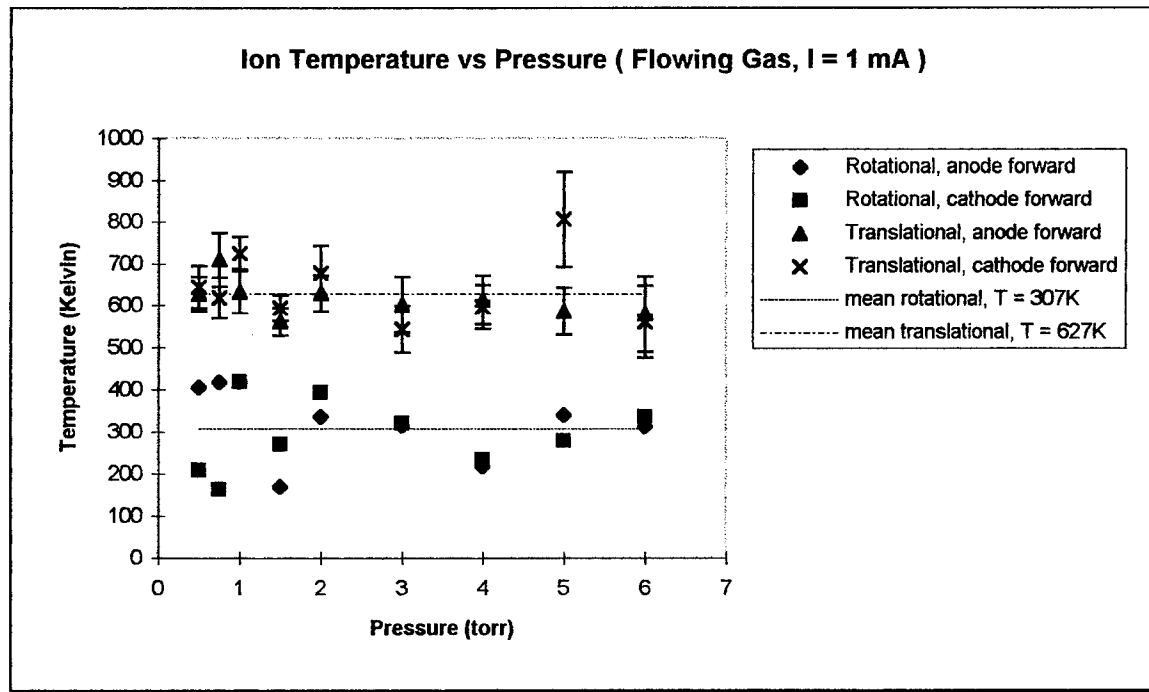


Figure 28. Ion Temperature vs Pressure, Flowing Gas,  $I = 1$  mA

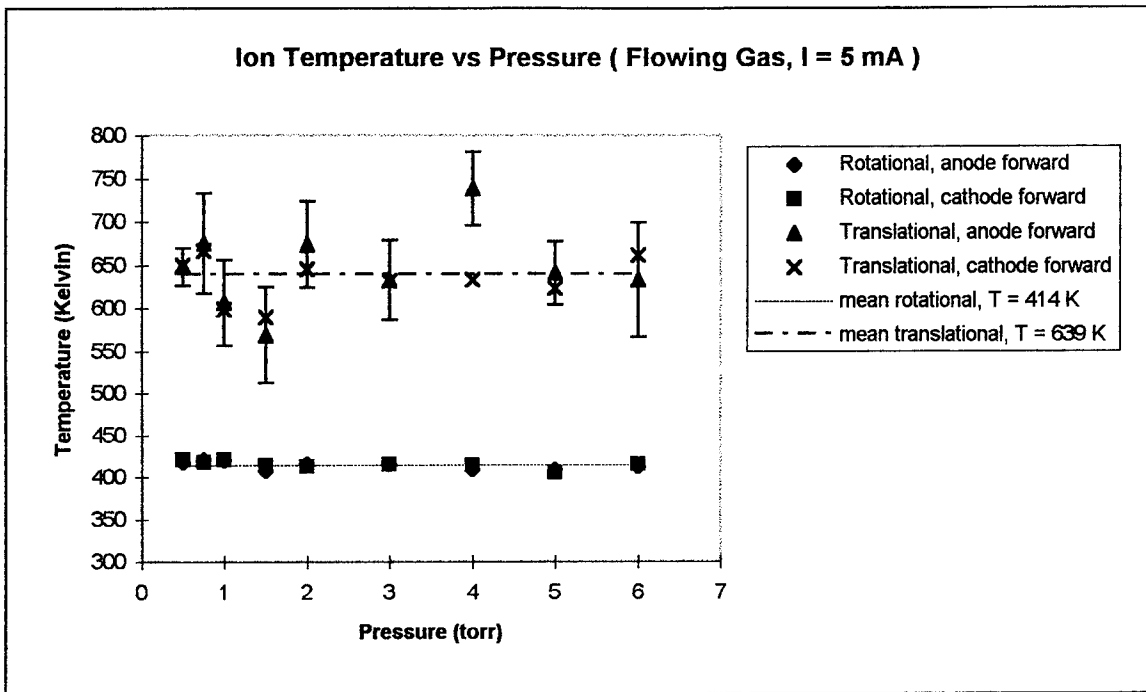


Figure 29. Ion Temperature vs Pressure, Flowing Gas,  $I = 5 \text{ mA}$

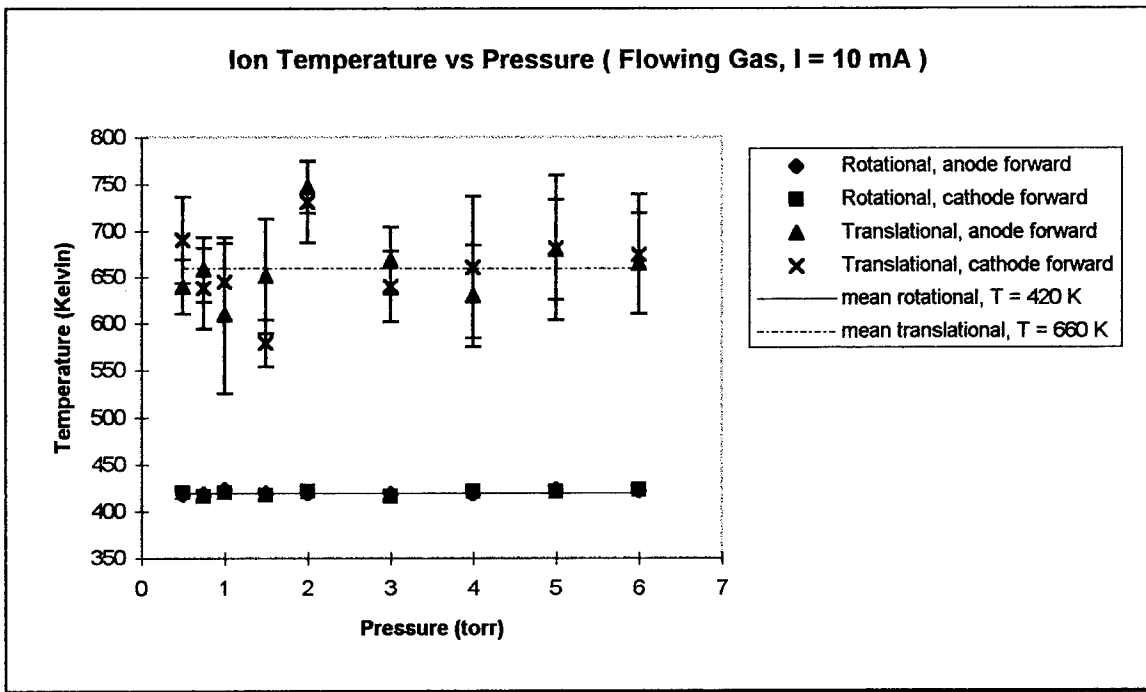


Figure 30. Ion Temperature vs Pressure, Flowing Gas,  $I = 10 \text{ mA}$

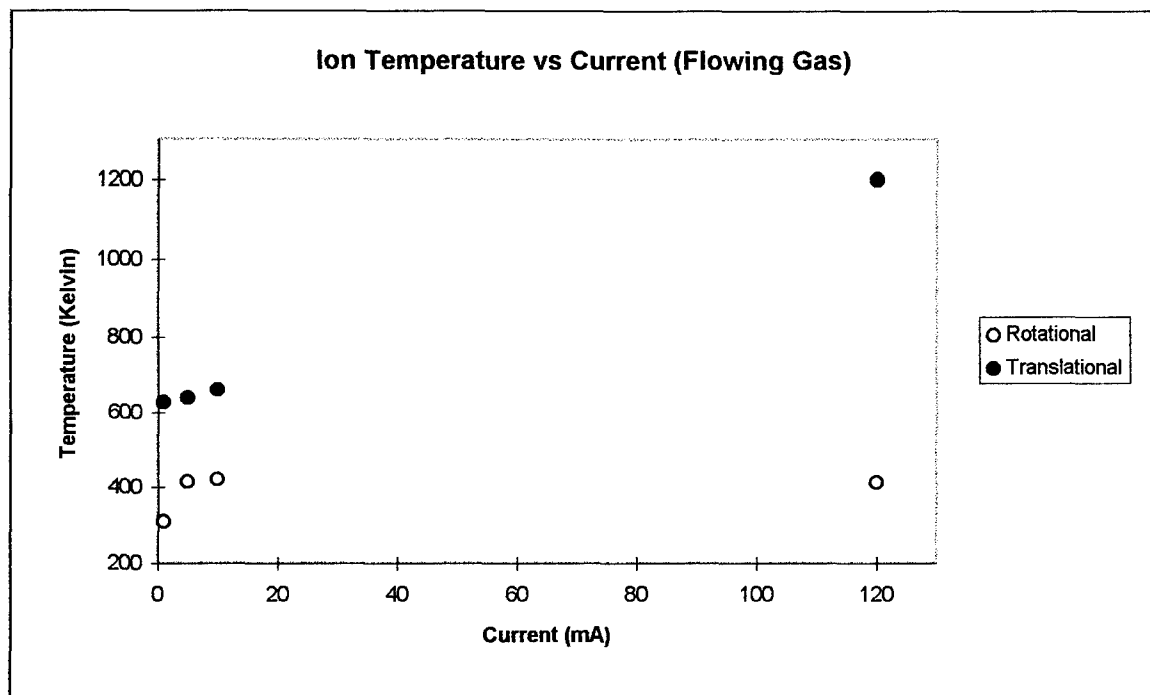


Figure 31. Ion Temperature vs Current, Flowing Gas

## B. Analysis

1. Corrections to Electric Field in Low Pressure Limit. The electric fields resulting from probe measurements resulted in poor agreement with previously published data at low pressures, but good agreement at high pressures. To correct the low pressure data, the electric field was calculated from the measured Doppler shift using equation (5). As the collision rate increases with pressure, equation (5) is no longer a good approximation, and as the following figures show, the calculated electric field decreases with pressure after reaching a peak at  $\sim 1$  torr.

The adjusted electric field will then consist of: 1) at low pressure ( $P < 1$  torr), values calculated from the measured Doppler shift; 2) at high pressure (3-6 torr), probe measurements; and 3) linearly interpolated values for the mid-pressure range (1-3 torr). The adjusted electric fields are given in Figures 32-37.

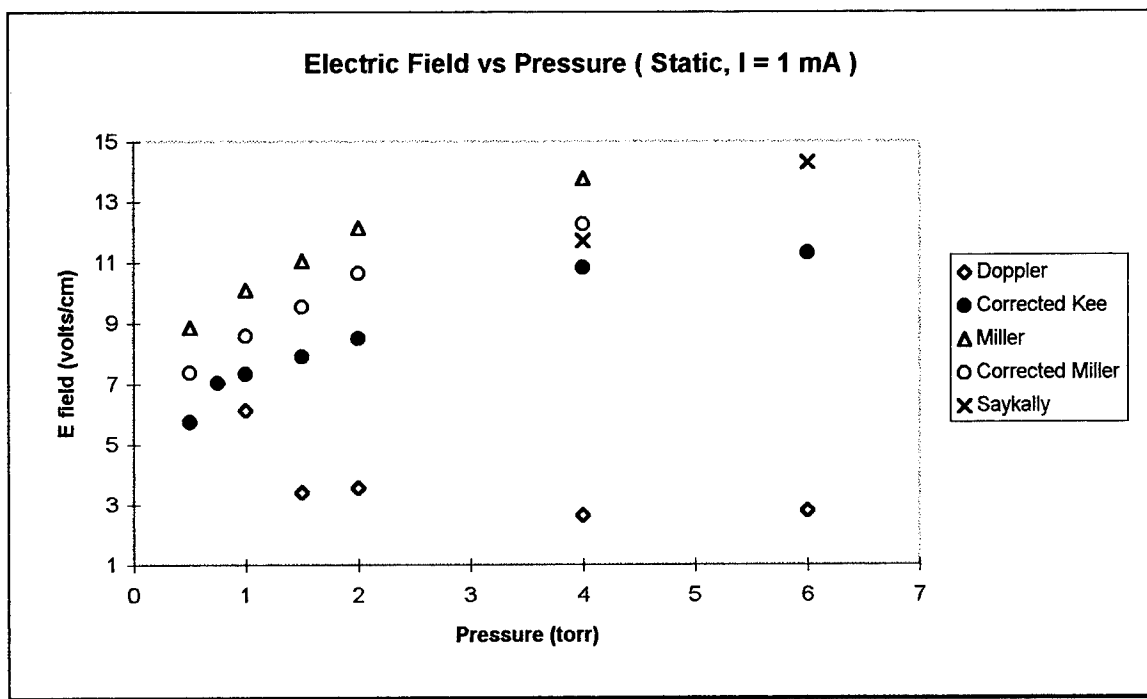


Figure 32. Adjusted Electric Field vs Pressure, Static Fill,  $I = 1$  mA

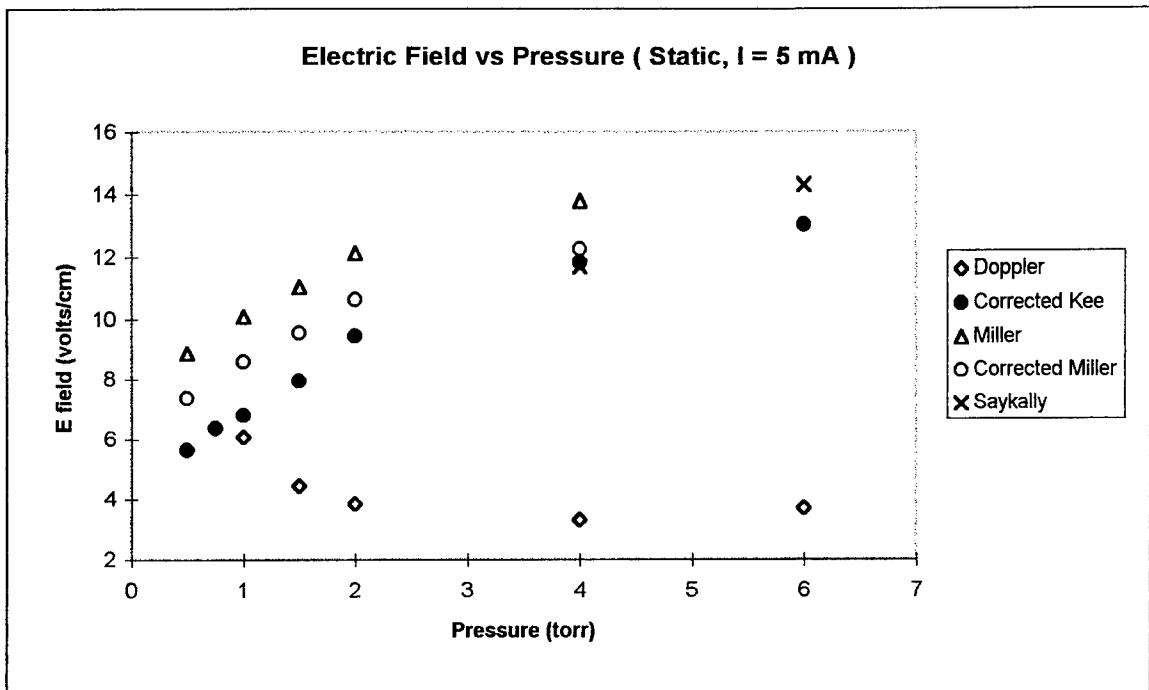


Figure 33. Adjusted Electric Field vs Pressure, Static Fill,  $I = 5 \text{ mA}$

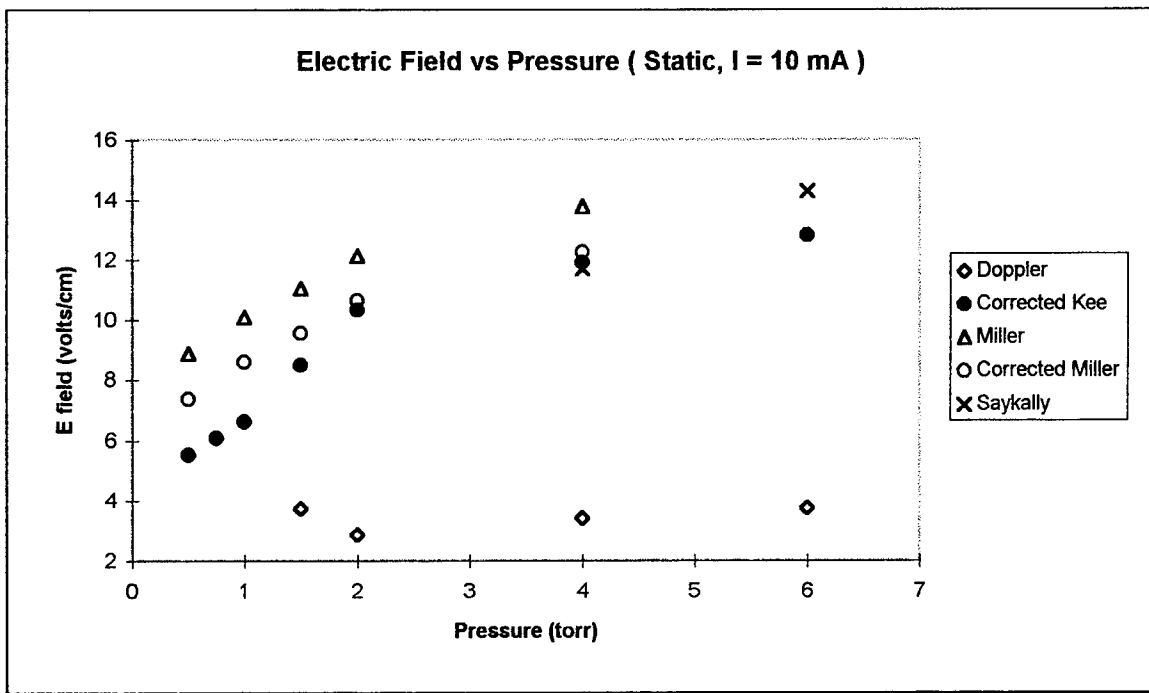


Figure 34. Adjusted Electric Field vs Pressure, Static Fill,  $I = 10 \text{ mA}$

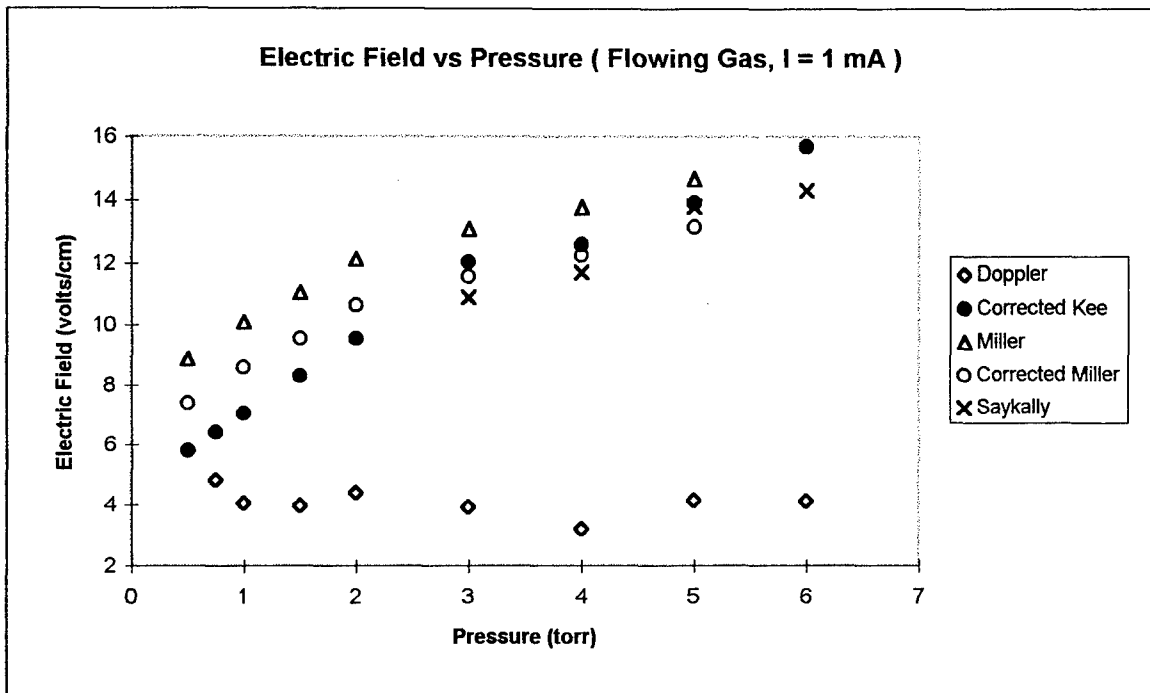


Figure 35. Adjusted Electric Field vs Pressure, Flowing Gas,  $I = 1 \text{ mA}$

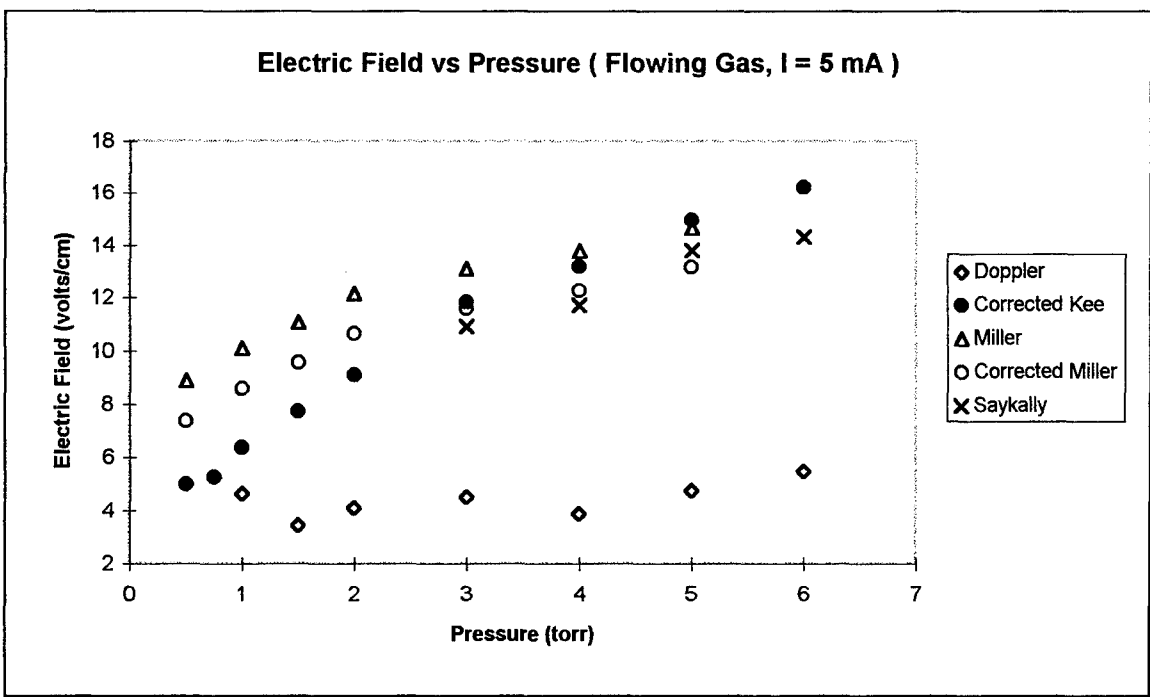


Figure 36. Adjusted Electric Field vs Pressure, Flowing Gas,  $I = 5 \text{ mA}$

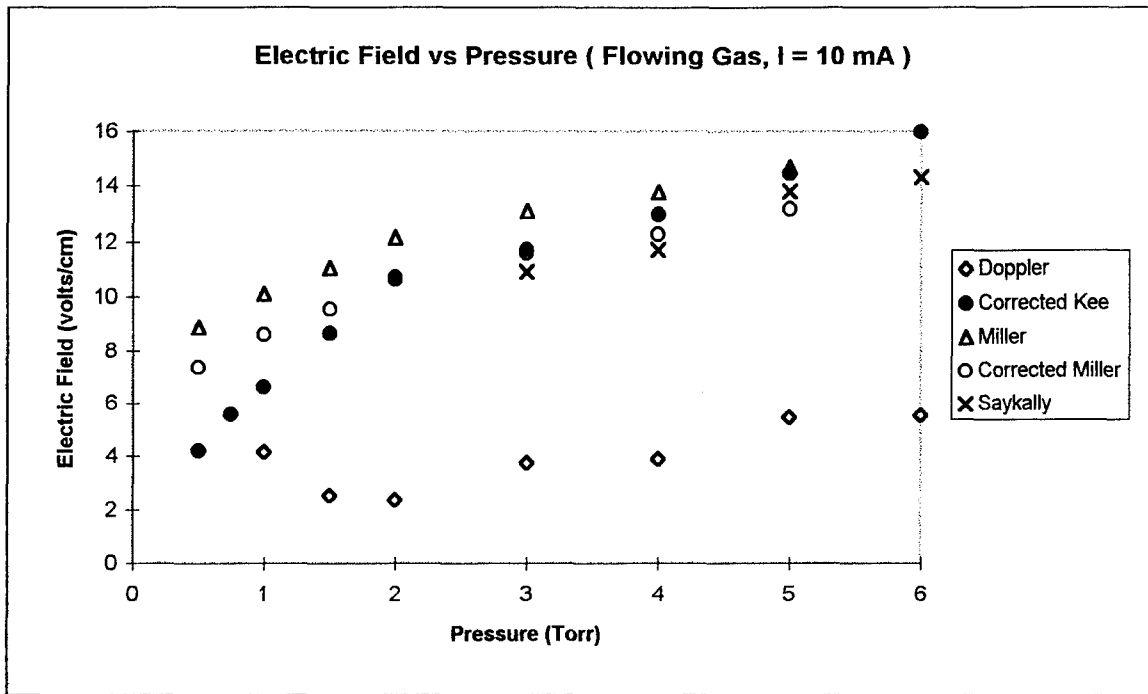


Figure 37. Adjusted Electric Field vs Pressure, Flowing Gas,  $I = 10 \text{ mA}$

2. E-scaled Doppler Shift vs Pressure. The E-scaled Doppler shifts were obtained by dividing the measured Doppler shift by the adjusted electric field. The results are displayed in Figures 38-43. In general, there is poor agreement between the measured values and the previously published values of Hong and Miller. The E-scaled Doppler shift tends to follow the same trend as the Hong and Miller data, but the expected drop in the shift due to collisions takes place at lower pressures than in their data.

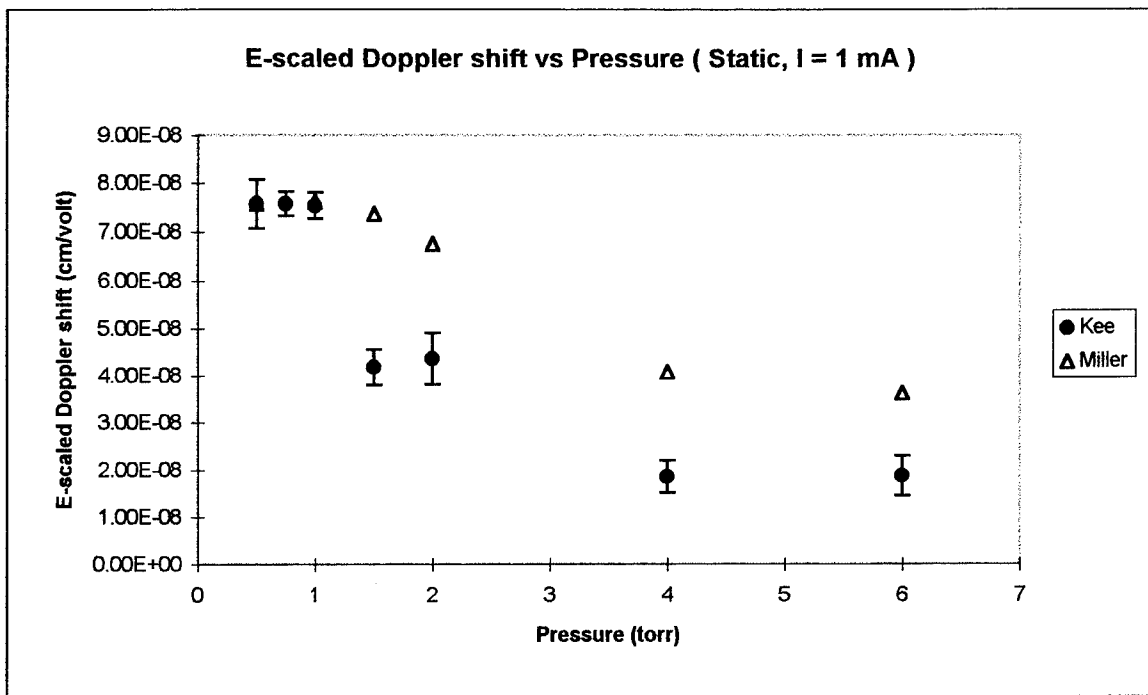


Figure 38. E-scaled Doppler Shift vs Pressure, Static Fill,  $I = 1 \text{ mA}$

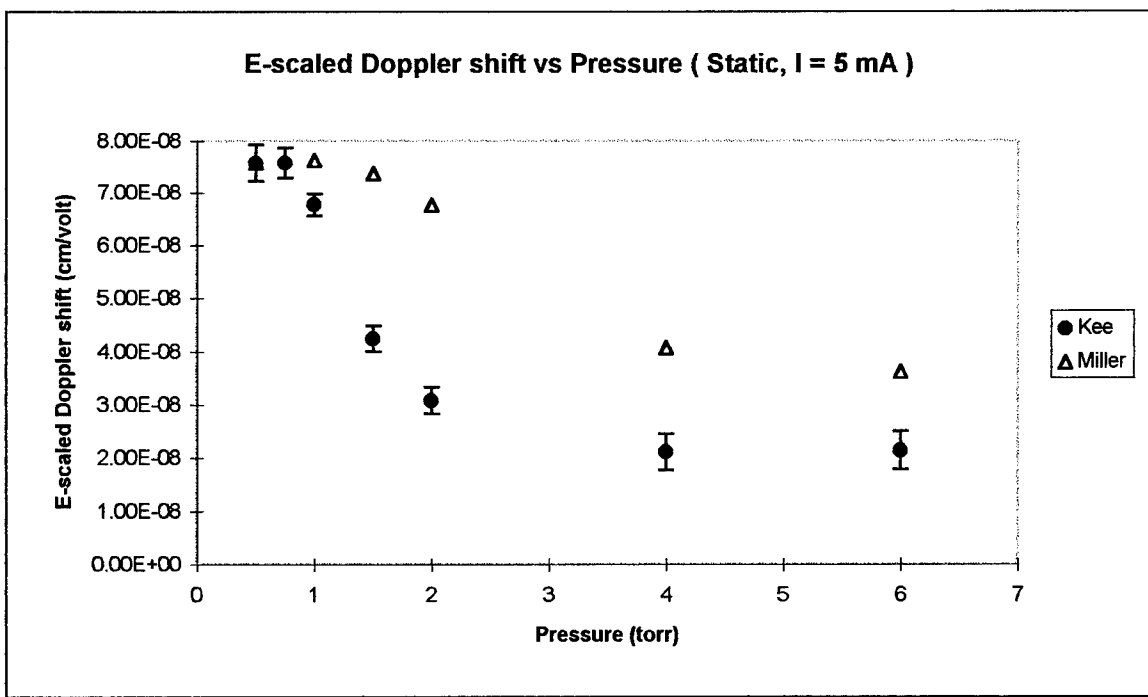


Figure 39. E-scaled Doppler Shift vs Pressure, Static Fill,  $I = 5 \text{ mA}$

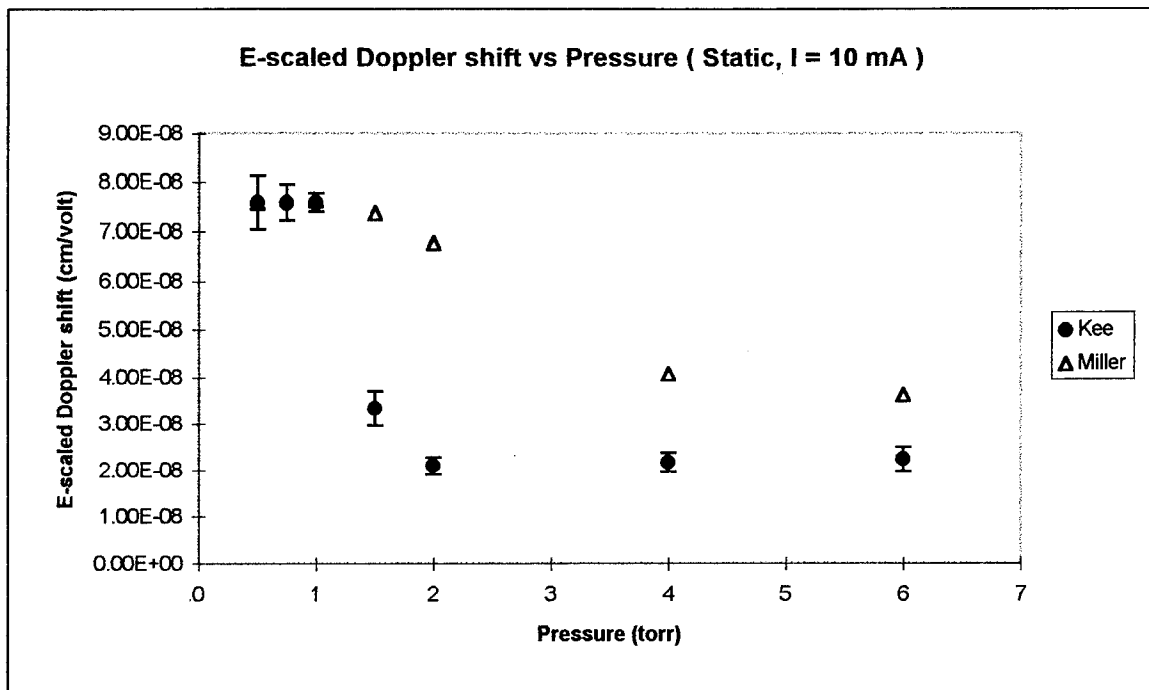


Figure 40. E-scaled Doppler Shift vs Pressure, Static Fill,  $I = 10 \text{ mA}$

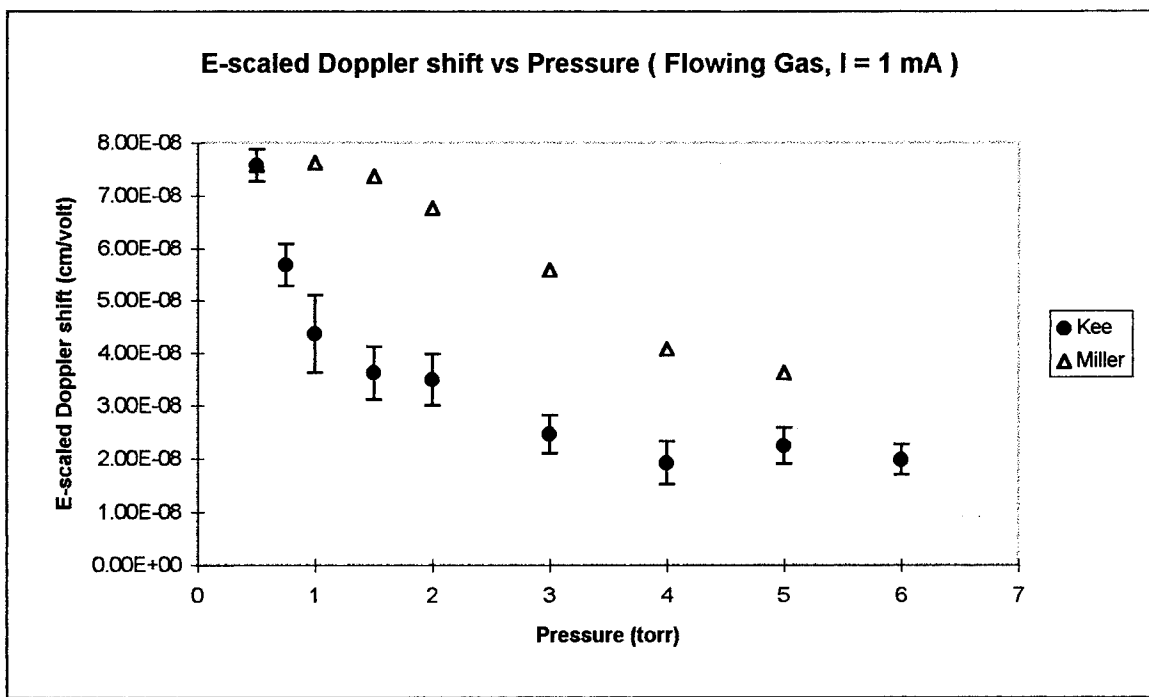


Figure 41. E-scaled Doppler Shift vs Pressure, Flowing Gas,  $I = 1 \text{ mA}$

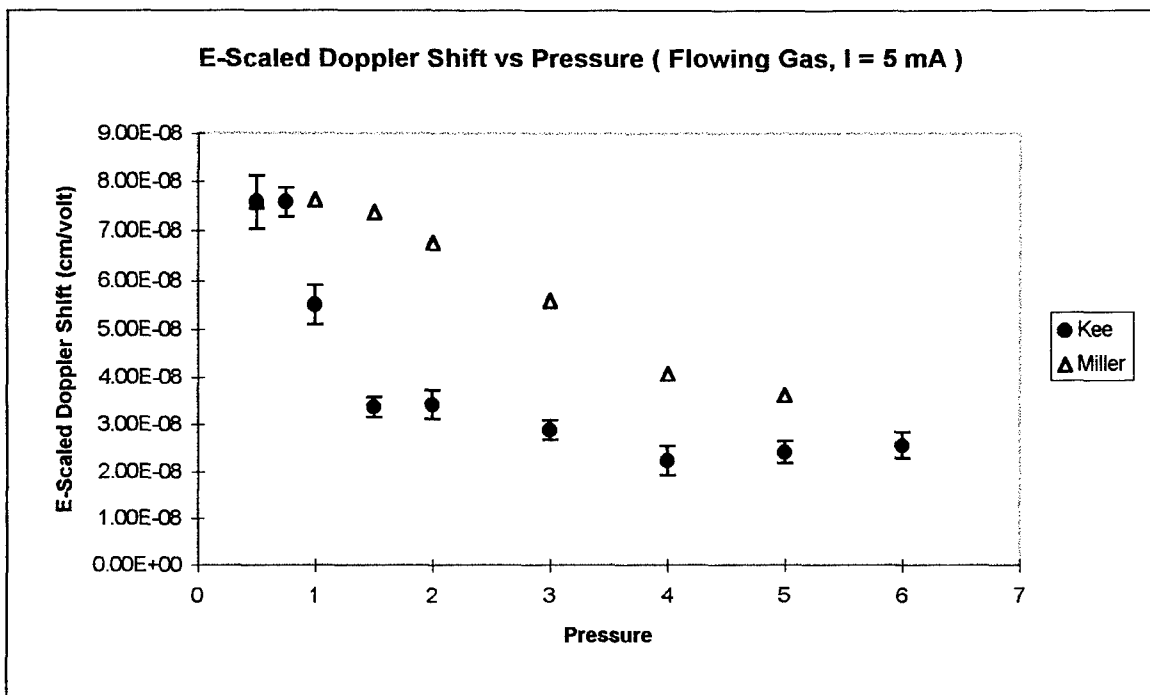


Figure 42. E-scaled Doppler Shift vs Pressure, Flowing Gas, I = 5 mA

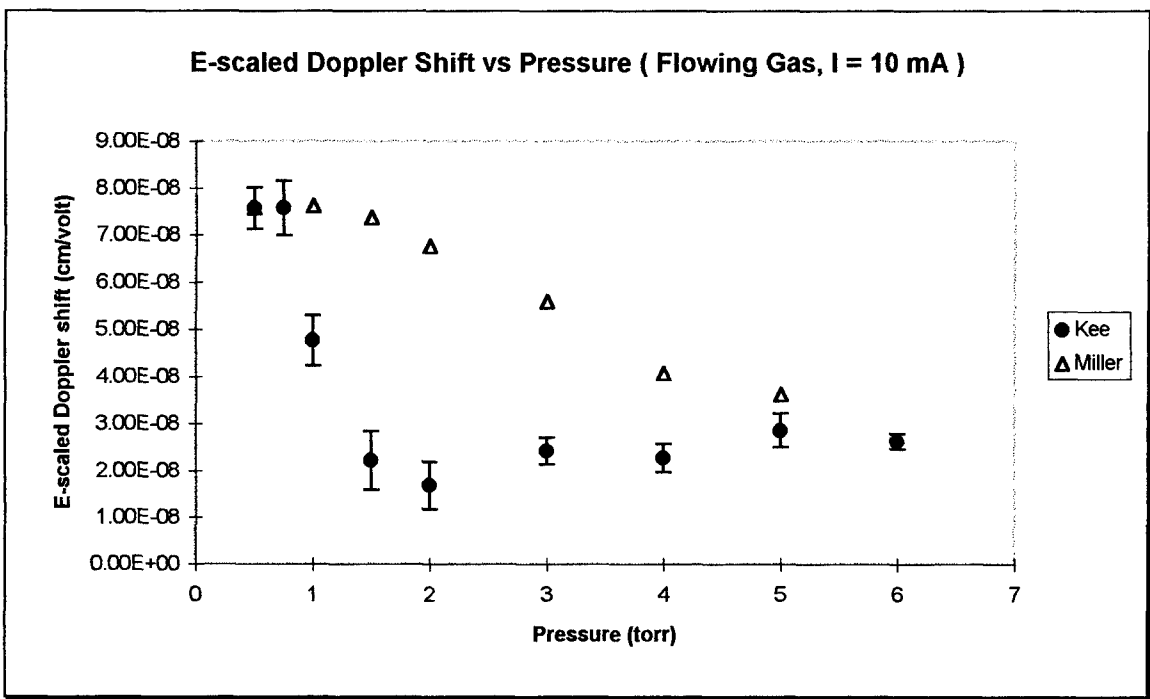


Figure 43. E-scaled Doppler Shift vs Pressure, Flowing Gas, I = 10 mA

3. Disagreement with Hong-Miller Experiment. For all experimental conditions, the observed Doppler shift disagreed with the Hong-Miller data. This experiment operated under similar conditions to that of Hong and Miller with the exception that the discharge currents were lower (1, 5, and 10 mA vs 25 mA).

A possible cause for the disagreement can be found by examining the four likely processes by which the  $N_2^+(B)$  ion are formed (see Figure 44). The first likely process is a one-step process, where  $N_2^+(B)$  is created by collision of a  $\sim 19$  eV electron with  $N_2$ . The second likely process is a two-step process where first  $N_2^+(X)$  is created by collision of a  $\sim 16$  eV electron with  $N_2$ , then  $N_2^+(B)$  from the collision of the  $N_2^+(X)$  ion with a  $\sim 3$  eV electron. The third and fourth processes involve collision of a He metastable with  $N_2$ . The metastable ionization can leave the  $N_2^+$  ion in either the B or X state. If the ion is left in the B state, it rapidly decays into the X state via radiative transition ( $\tau = 66\text{ns}$ ). Then  $N_2^+(B)$  can be formed by collision with a  $\sim 3$  eV electron.

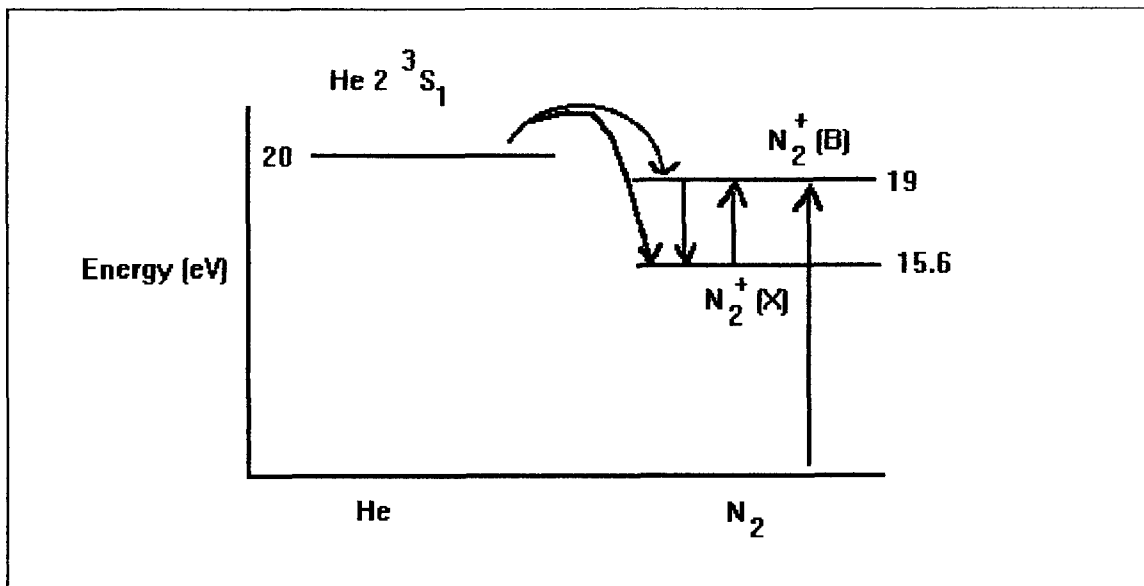


Figure 44.  $N_2^+(B)$  Formation Processes

The method of  $\text{N}_2^+(\text{B})$  formation affects the observed Doppler shift. The theory developed in Chapter 2 assumes a one-step process. If a two-step process is involved, then the observed Doppler shift would increase, because the ion accumulates kinetic energy from the applied electric field while in the X state.

Examination of the electron energy distribution function for the two experimental conditions can be used to qualitatively argue that the Hong-Miller experiment may be operating under conditions that include a greater fraction of two-step processes than in the author's experiment. In Figure 45, the electron energy distribution functions are plotted for discharge currents of 10 and 25 mA. The plot suggests that the one-step process may compose a higher fraction of the total rate of  $\text{N}_2^+(\text{B})$  formation for the 10 mA case, than for the 25 mA case. However, a detailed calculation, beyond the scope of this thesis, is required to definitively determine the relative contributions of one- and two-step processes to the total  $\text{N}_2^+(\text{B})$  formation rate.

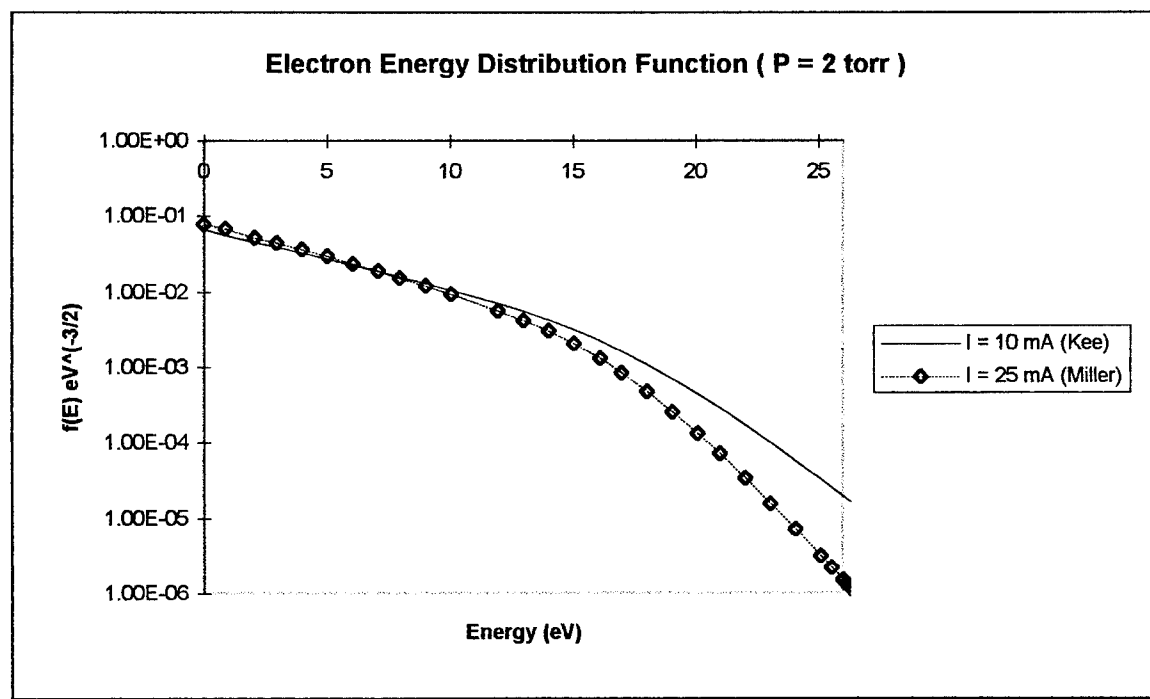


Figure 45. Electron Energy Distribution Function [22]

For the case of the metastable processes, the electron energy distribution function suggests that at  $\sim 3$  eV, the higher current has a larger distribution of electrons that will collisionally excite  $\text{N}_2^+(X)$  to  $\text{N}_2^+(B)$ . Again, the residence time in the X state will show as a bias towards larger Doppler shifts.

4. Plot of  $\chi^2$  Surface. The problem of fitting an equation to a set of data by choosing optimum fitting parameters has been addressed by Bevington [24:96-167]. The method used in analyzing data for this experiment is the *least-squares method*. Consider a set of  $j$  data points  $(y(x_j), x_j)$ , where  $x_j$  is the independent variable, and  $y(x_j)$  is the dependent variable. A fitting equation  $F(x_j, \alpha, \beta)$  is proposed to graph against the data, where  $\alpha$  and  $\beta$  are adjustable parameters, chosen to ‘optimize’ the fit to the experimental data.

The figure of merit for the fit is *chi-squared*,  $\chi^2$  which is defined as:

$$\chi^2 = \sum_j (F(x_j, \alpha, \beta) - y(x_j))^2 \frac{1}{\sigma_j^2} \quad (52)$$

where  $\sigma_j$  is the experimental error associated with the  $j$ th data point. Optimization of the fit is performed by choosing values of  $\alpha$  and  $\beta$  that minimize the value of  $\chi^2$ .

To determine  $Q_v$  and  $Q_q$ , the least-squares method is used to fit equation (25) to the experimental E-scaled Doppler shifts. Initially, a MathCAD 5.0 spreadsheet was written to perform the fit, using the Levenberg-Marquardt algorithm contained in the ‘solve block’ routine [25:499]. This proved to be unsatisfactory, as the value obtained from the fit proved to be highly sensitive to initial conditions.

Although it is computationally expensive, the *grid-search* method was finally used, due to its robustness, to search for the minima of  $\chi^2$ . In this method,  $\chi^2$  is computed at trial values of the fitting parameters, and the minima is found by inspection. A MathCAD spreadsheet was written to plot  $\chi^2$  as function of  $Q_v$  and  $Q_q$ , and to display the values in a table. The plots are given in Figures 47-52, and  $\chi^2$  values are presented in Tables 1-6.

The results are disappointing, in that the plots show  $\chi^2$  being a very weak function of  $Q_v$ , although being strongly dependent on  $Q_q$ . No minima in  $\chi^2$  is observed for positive values of  $Q_v$ , which eliminates the possibility of determining the ion mobility from this experiment.

A rough estimate of the quenching cross-section  $Q_q$ , can be obtained from the chi-square plots. Using the established value of the mobility ( $K_o = 19 \text{ cm}^2/\text{volt/sec}$ ), an estimate for the collision-cross section can be obtained from the Langevin equation [26:162]:

$$K_o = 0.815 \times \frac{e\lambda}{M_{ion}V} \sqrt{\frac{M_{ion} + M_{gas}}{M_{ion}}} \quad (53)$$

where

$$\lambda = \frac{1}{N_{gas}Q_v} \quad (54)$$

using the standard temperature (273 K) and pressure (760 torr). Assuming an ideal gas results in a collision cross-section of  $\sim 34.2 \text{ angstrom}^2$ . (This is in disagreement with the

Hong-Miller value of 17.8 angstrom<sup>2</sup>. This may be the result of their expression for the collision frequency being in error, reference equations 28 and 29).

Inspecting the plots shows that for the static gas fill experiments, a  $Q_q$  value on the order of 15-20 angstrom<sup>2</sup> is anticipated, while the flowing gas experiment results in a  $Q_q$  value of 20-25 angstrom<sup>2</sup>. In comparison, Hong and Miller reported a value of 6.3 angstrom<sup>2</sup>. The higher quenching cross-section for the flowing gas rate is attributed to a higher ion-gas collision velocity due to the flowing of the gas through the tube. The difference between our measured values and Hong and Miller's is attributed to the bias in the observed Doppler shift which results from a significant fraction of two-step  $N_2^+(B)$  production.

The larger quenching rate for the flowing gas in comparison to the static gas fill corresponds to a reduced measured E-scaled Doppler shifts in the mid-pressure regions, as well as a shift in the peak Doppler shifts to lower pressures. This also holds for comparisons to the Hong and Miller data

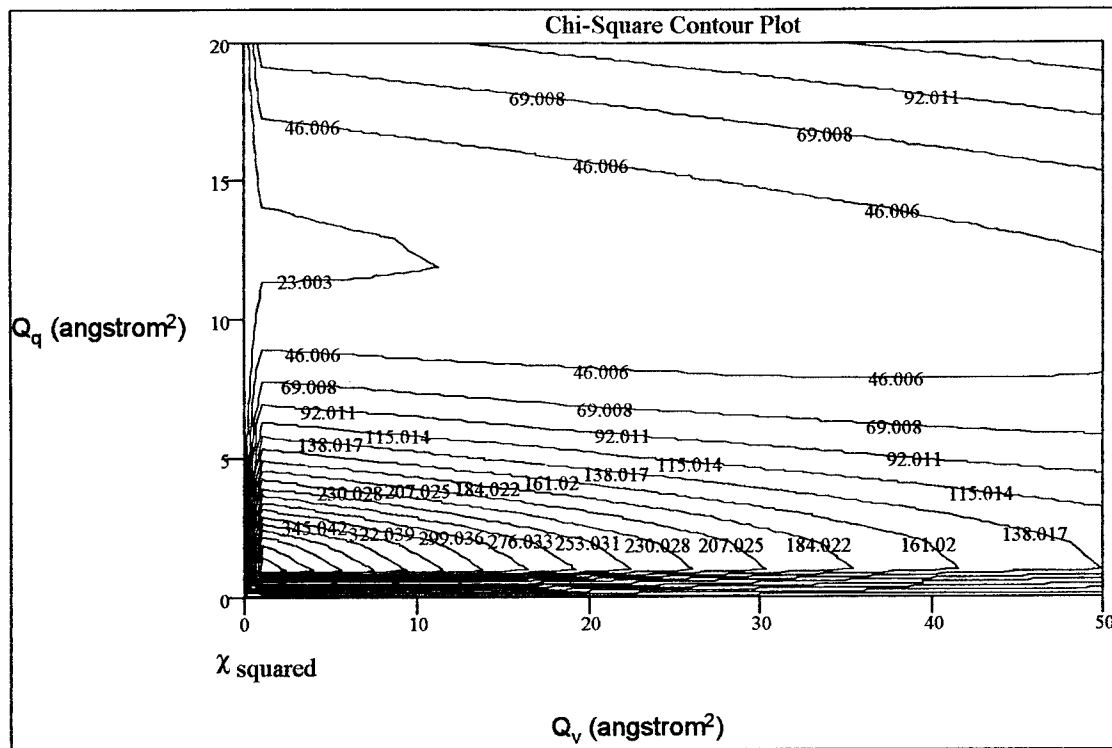


Figure 46.  $\chi^2$  Plot, Static Fill,  $I = 1$  mA

Table 1.  $\chi^2$  values, Static Fill,  $I = 1$  mA

$Q_v$ angstrom $^2$	$Q_q$ angstrom $^2$	10	11	12	13	14	15	16
1		32.969	24.936	20.899	20.259	22.559	27.435	34.578
2		32.617	24.847	21.026	20.564	23.013	28.014	35.261
3		32.289	24.779	21.170	20.884	23.479	28.603	35.953
4		31.986	24.732	21.331	21.217	23.957	29.202	36.653
5		31.706	24.703	21.508	21.564	24.447	29.81	37.361
6		31.451	24.695	21.701	21.925	24.947	30.428	38.077
7		31.219	24.706	21.911	22.299	25.459	31.055	38.801

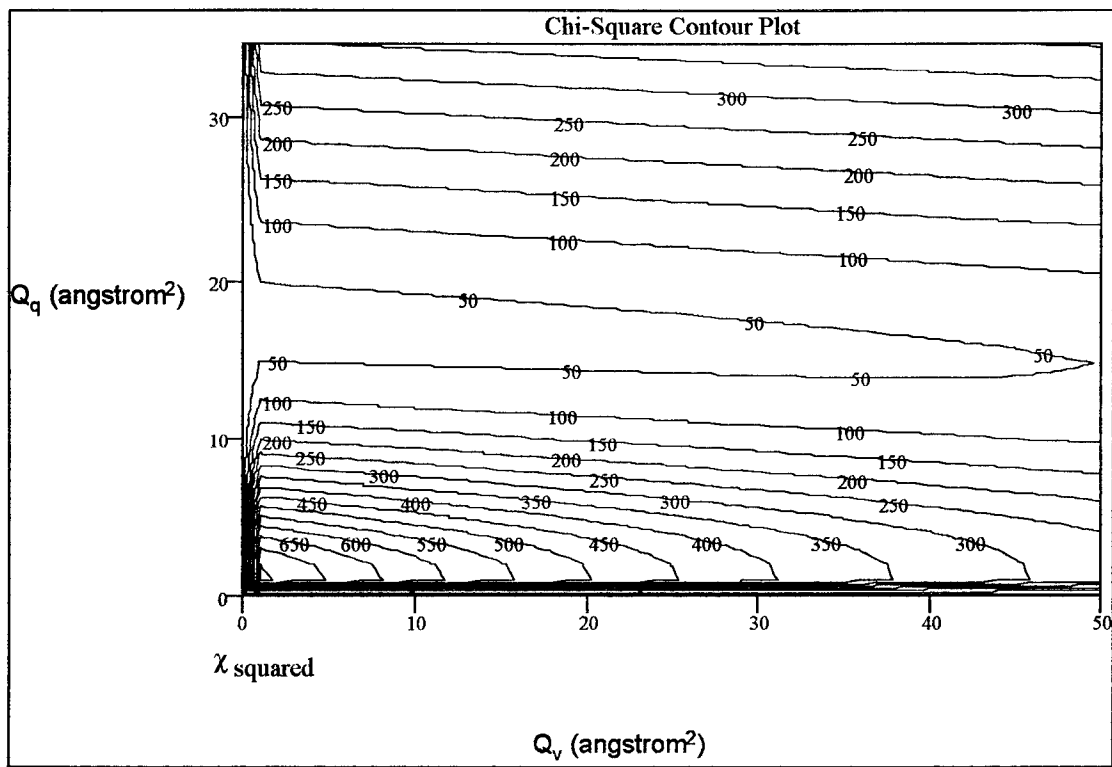


Figure 47.  $\chi^2$  Plot, Static Fill,  $I = 5 \text{ mA}$

Table 2.  $\chi^2$  values, Static Fill,  $I = 5 \text{ mA}$

$Q_v$ $\text{angstrom}^2$	$Q_q$ $\text{angstrom}^2$	14	15	16	17	18	19	20
1		66.299	51.093	41.792	37.662	38.031	42.292	49.903
2		65.416	50.604	41.629	37.769	38.361	42.807	50.570
3		64.562	50.137	41.484	37.892	38.705	43.333	51.247
4		63.734	49.693	41.358	38.029	39.061	43.870	51.932
5		62.934	49.271	41.250	38.182	39.430	44.417	52.626
6		62.160	48.871	41.161	38.151	39.812	44.975	53.329
7		61.413	48.493	41.09	38.534	40.206	45.543	54.04

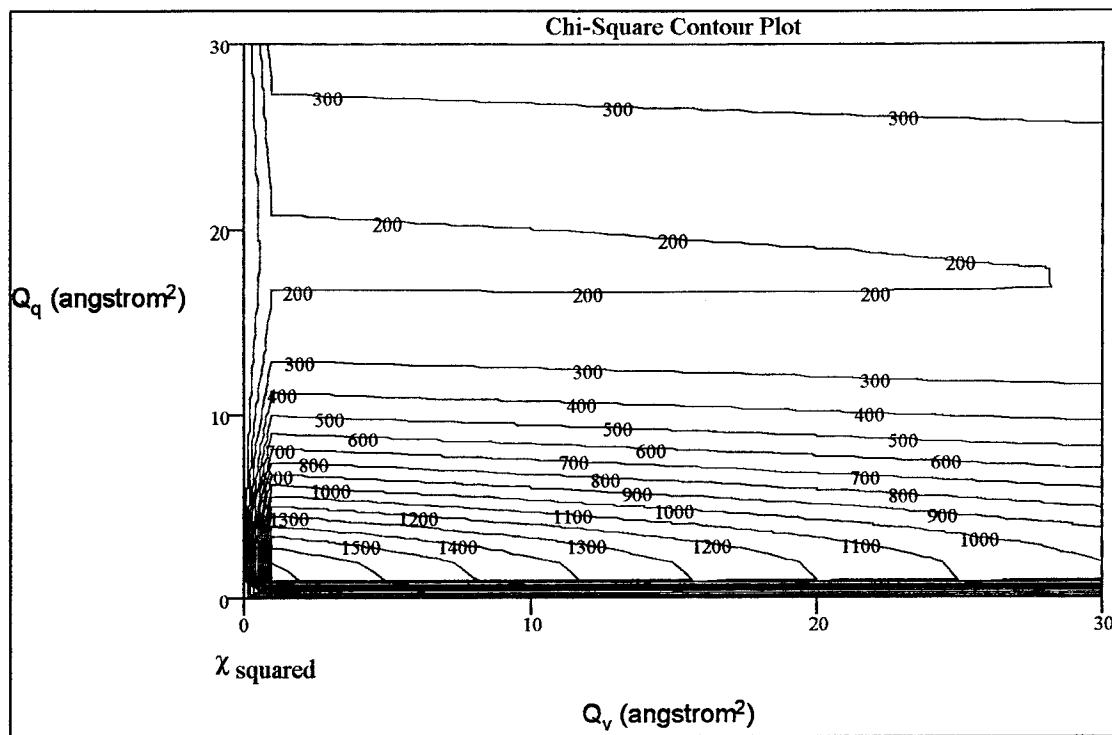


Figure 48.  $\chi^2$  Plot, Static Fill,  $I = 10 \text{ mA}$

Table 3.  $\chi^2$  values, Static Fill,  $I = 10 \text{ mA}$

$Q_v$ $\text{angstrom}^2$	$Q_q$ $\text{angstrom}^2$	17	18	19	20	21
1		198.811	191.984	190.631	193.901	201.06
2		198.639	192.103	190.988	193.450	201.766
3		198.484	192.237	191.357	195.010	202.48
4		198.346	192.385	191.738	195.579	203.202
5		198.226	192.548	192.130	196.158	203.931
6		198.124	192.725	192.534	196.746	204.669
7		198.038	192.915	192.949	197.344	205.414

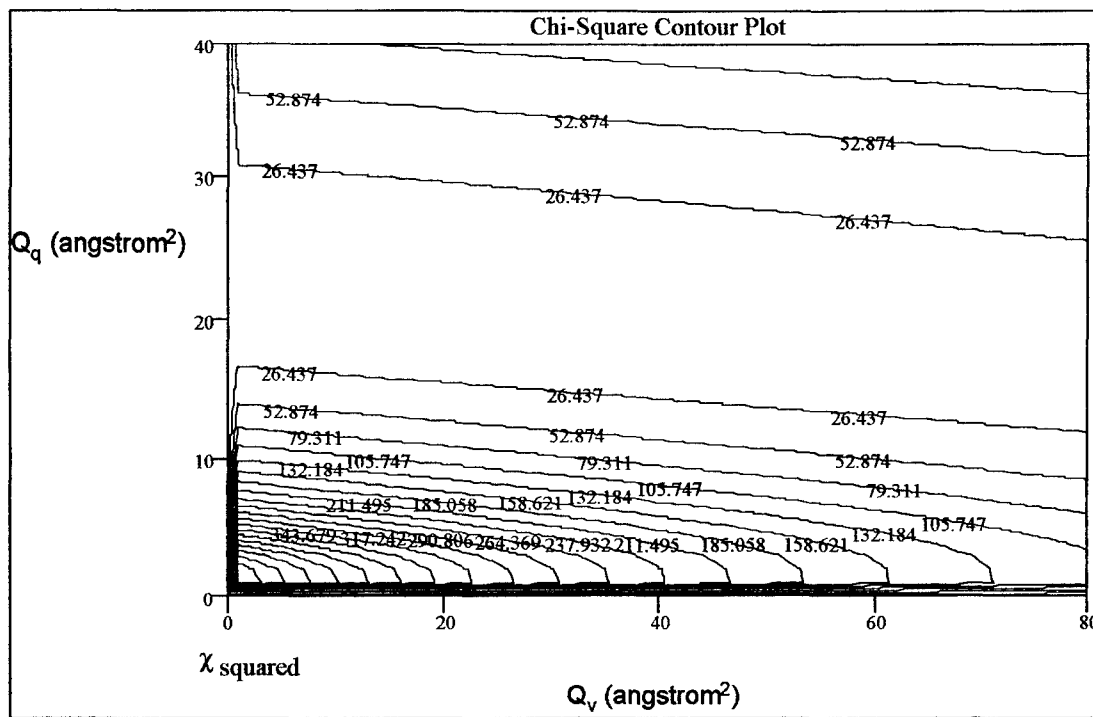


Figure 49.  $\chi^2$  Plot, Flowing Gas,  $I = 1 \text{ mA}$

Table 4.  $\chi^2$  values, Flowing Gas,  $I = 1 \text{ mA}$

$Q_v$ $\text{angstrom}^2$	$Q_q$ $\text{angstrom}^2$	22	23	24	25	26
1		7.559	7.193	7.619	8.756	10.532
2		7.554	7.228	7.697	8.872	10.682
3		7.533	7.266	7.778	8.991	10.833
4		7.525	7.307	7.862	9.112	10.986
5		7.521	7.351	7.948	9.235	11.142
6		7.521	7.398	8.038	9.361	11.299
7		7.523	7.449	8.129	9.489	11.459

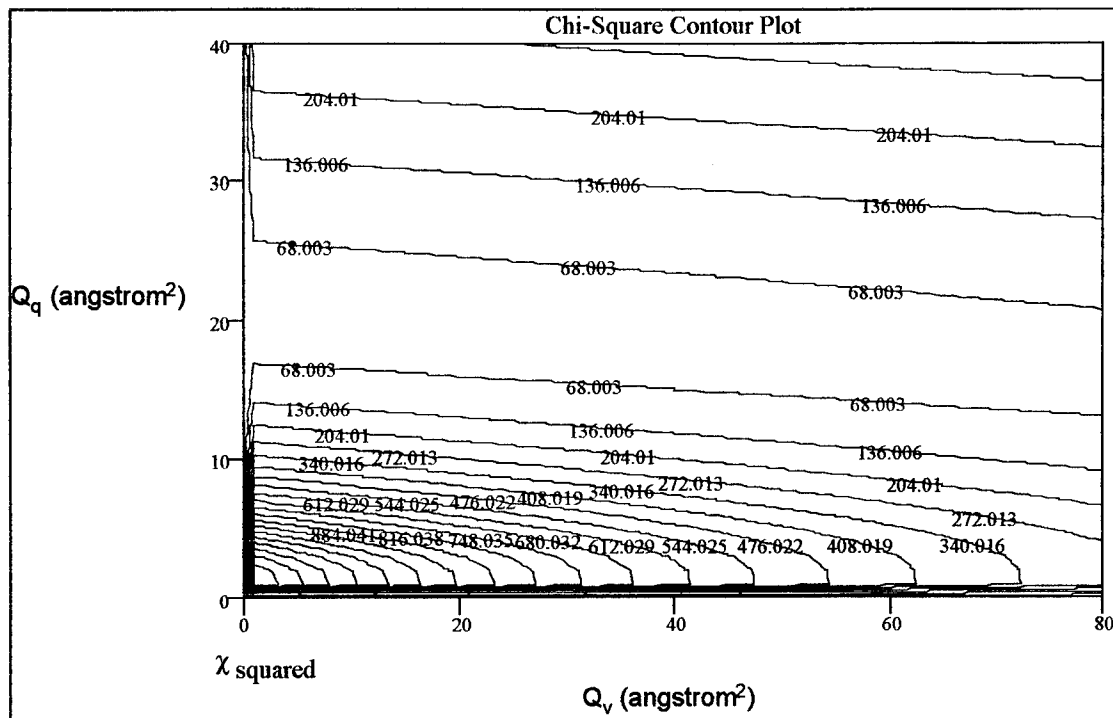


Figure 50.  $\chi^2$  Plot, Flowing Gas,  $I = 5 \text{ mA}$

Table 5.  $\chi^2$  values, Flowing Gas,  $I = 5 \text{ mA}$

$Q_v$ angstrom $^2$	$Q_q$ angstrom $^2$	19	20	21	22	23
1		47.739	43.340	42.145	43.667	47.493
2		47.498	43.282	42.238	43.885	47.814
3		47.267	43.233	42.339	44.110	48.140
4		47.047	43.192	42.447	44.340	48.472
5		46.838	43.161	42.563	44.577	48.808
6		46.640	43.139	42.686	44.820	49.150
7		46.452	43.126	42.816	45.070	49.497

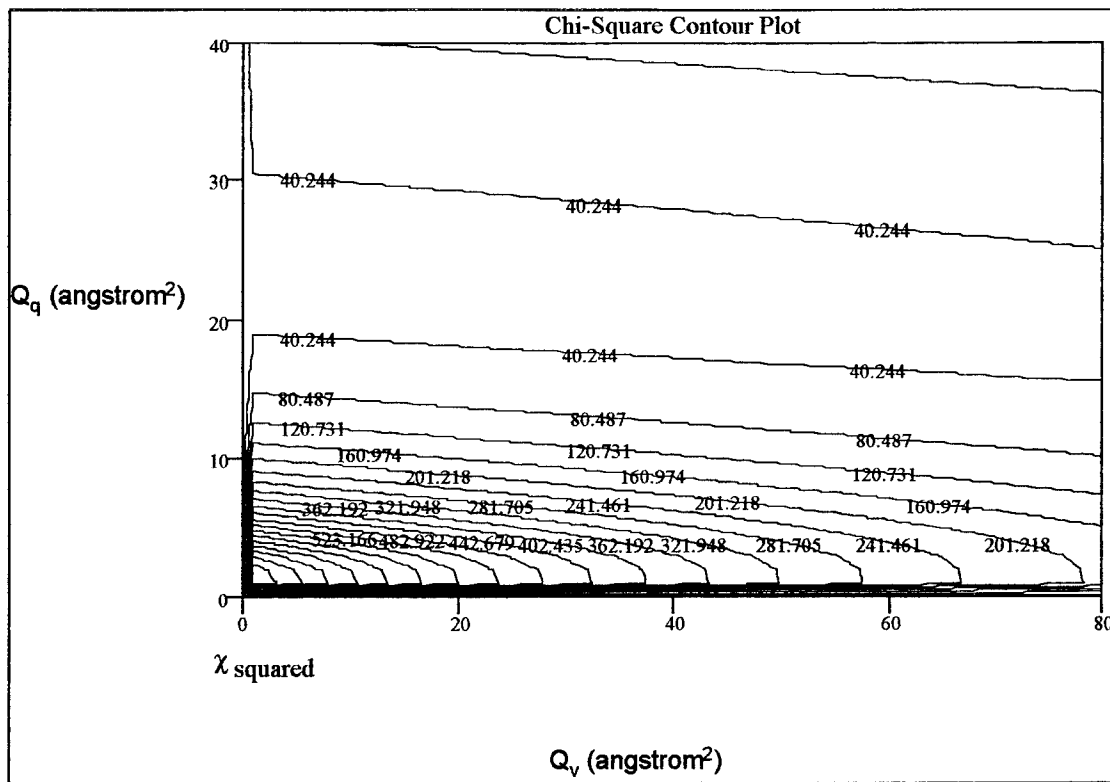


Figure 51.  $\chi^2$  Plot, Flowing Gas,  $I = 10$  mA

Table 6.  $\chi^2$  values, Flowing Gas,  $I = 10$  mA

$Q_v$ angstrom $^2$	$Q_q$ angstrom $^2$	22	23	24	25	26
1		30.786	29.511	29.082	29.385	30.322
2		30.734	29.506	29.177	29.453	30.420
3		30.685	29.504	29.154	29.524	30.519
4		30.639	29.504	29.193	29.597	30.620
5		30.596	29.506	29.234	29.671	30.722
6		30.555	29.511	29.278	29.747	30.826
7		30.518	29.518	29.323	29.825	30.932

Comparison to Hong-Miller results. The failure to obtain a physically realistic collision cross-section via this experiment raises the question of why this experiment failed where Hong and Miller succeeded. The explanation may lie in a statistical analysis of the Hong-Miller data. For this purpose, their data was extracted

from graphs by measuring with a metric ruler. The resolution of the ruler was well within the 8 mm wide error bars on the graph.

The  $\chi^2$  values of the fit to the Hong-Miller data were computed and are presented below in Figure 53 and Table 7. The  $\chi^2$  plot on their data shows a weak dependence on  $Q_v$  and a strong dependence on  $Q_q$ . Inspection of the  $\chi^2$  values in Table 7 yield  $Q_v \approx 5$  angstrom<sup>2</sup> in comparison to their published value of  $17.8 \pm 1.8$  angstrom<sup>2</sup>, and  $Q_q \approx 7$  angstrom<sup>2</sup> in comparison to their published value of  $6.3 \pm 0.7$  angstrom<sup>2</sup>.

This large disagreement between the  $Q_v$  given by Hong and Miller, and the values is likely due to the flat nature of the  $\chi^2$  surface along the  $Q_v$  axis. The Hong-Miller data was not given in text form, nor was their curve-fitting method specified. Slight deviations in their data, and the values extracted from the graph may be responsible for shifting the minima along the very flat  $\chi^2$  surface. The choice of curve-fitting method could also impact the final value of the fitting parameters. For example, the widely used Levenberg-Marquardt method performs poorly when the  $\chi^2$  surface is flat, and could converge to an incorrect result [27:525].

The apparent sensitivity of the location of the minimum to either a small change in initial conditions (experimental data), or a change in the  $\chi^2$  minima search algorithm implies that the 1.8 angstrom<sup>2</sup> uncertainty in  $Q_v$  given by Hong and Miller is underestimated. This insensitivity is illustrated in Figure 54 for the case where equation (28) is used to define the collision frequency.

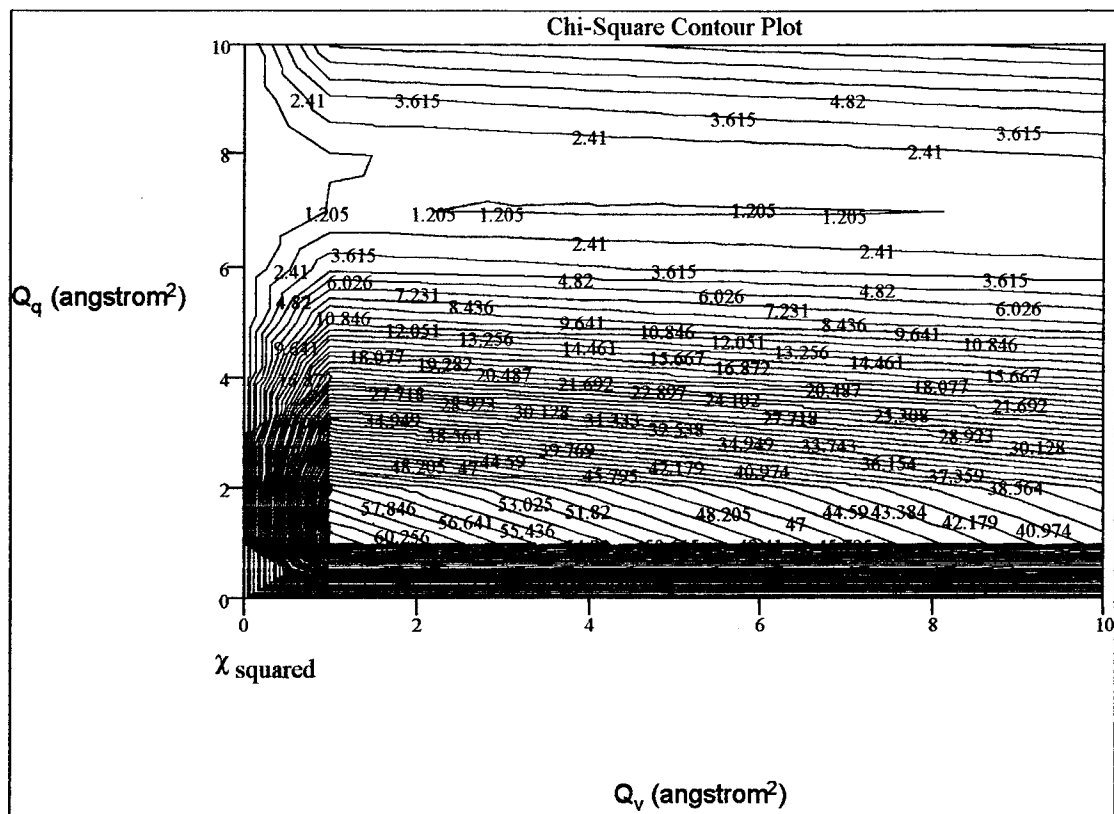


Figure 52.  $\chi^2$  Plot, Hong-Miller Experiment,  $I = 25$  mA

Table 7.  $\chi^2$  values, Hong-Miller Experiment,  $I = 25$  mA

$Q_v$ angstrom $^2$	$Q_q$ angstrom $^2$	5	6	7	8	9
1		11.962	4.543	1.263	1.152	3.395
2		11.315	4.252	1.212	1.263	3.614
3		10.699	3.983	1.176	1.384	3.84
4		10.115	3.735	1.154	1.514	4.074
5		9.562	3.506	1.145	1.654	4.314
6		9.038	3.298	1.150	1.803	4.561
7		8.543	3.109	1.168	1.962	4.814

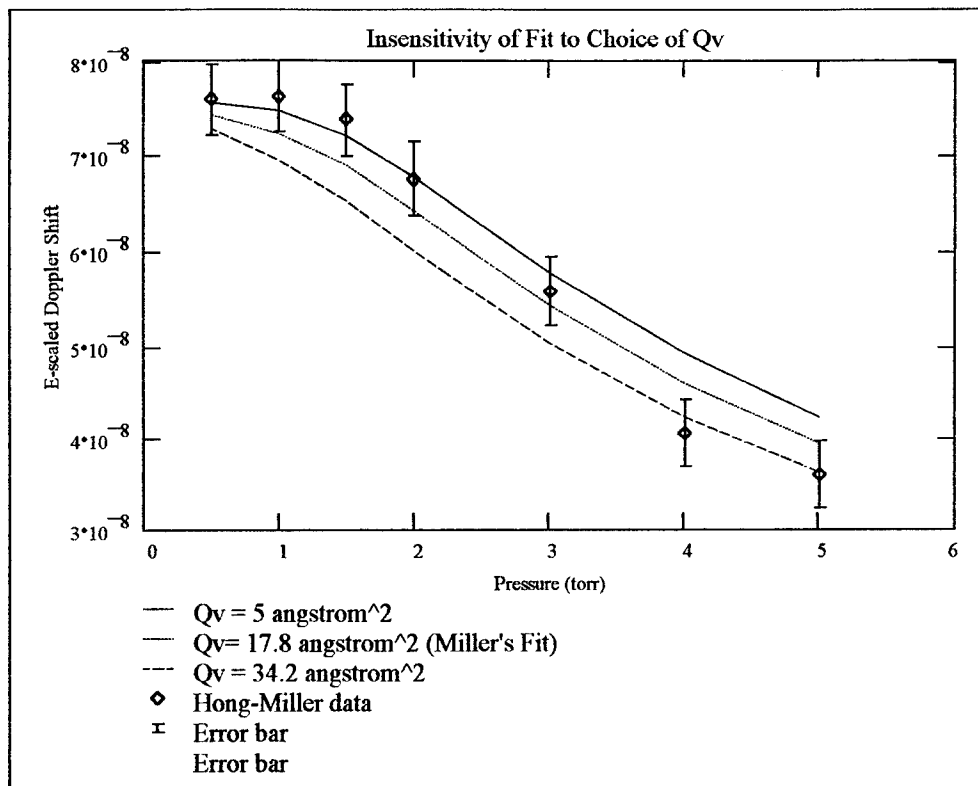


Figure 53. Insensitivity of Fitting Equation to Choice of  $Q_v$  for Hong-Miller Data.

## VI. Conclusions and Recommendations

### A. Summary of Results

This experiment failed to determine the mobility of the  $\text{N}_2^+$  ion in helium. This was due to the inability to reduce the data using the model of Hong and Miller. A  $\chi^2$  surface was calculated from a fit of the experimental data to a theoretical expression for the E-scaled Doppler shift. This surface was steep in the direction of the quenching cross-section, but flat in the direction of the collision cross-section. Whether the fitting equation is inherently insensitive to a fit to the collision cross-section has not been proven. It is possible that the flat  $\chi^2$  surface is the result of the model not being applicable to the data.

Estimates of the quenching cross-section were obtained from the  $\chi^2$  plots, assuming a collision cross-section of 34.2 angstrom<sup>2</sup> derived from the Langevin expression for the mobility, and previously published values of the  $\text{N}_2^+$  mobility in helium. For the static gas fill,  $Q_q \approx 15\text{-}20$  angstrom<sup>2</sup>, while for the flowing gas,  $Q_q \approx 20\text{-}25$  angstrom<sup>2</sup>. This is higher than the value reported by Hong and Miller ( $Q_q = 6.3 \pm 0.7$  angstrom<sup>2</sup>).

### B. Recommendations for Further Research

A statistical analysis of the data from this experiment and the Hong-Miller experiment show that measurements of the Doppler-shift resulting from the emission spectra of the  $\text{B} \rightarrow \text{X}$  transition of  $\text{N}_2^+$  yield a highly uncertain value for the collision

cross-section. Further work is needed on the model presented by Hong and Miller to determine under what conditions it may be applied towards experimental data

This leaves open the question of switching to the  $A \rightarrow X$  transition of  $N_2^+$ . Whether this would be fruitful depends on the sensitivity of the  $\chi^2$  surface to the fitting parameters. Hong and Miller have published cross-section resulting from this transition. A statistical analysis of their results, as performed here for the  $B \rightarrow X$  transition, should be accomplished prior to performing the experiment. In circumstances where no prior data is available, a rough estimate could be made of the ion mobility, and thus the collision-cross section. Values could then be generated for the E-scaled Doppler shift (a random number generator could be used to produce statistical error) for a range of pressures. Examination of the resulting  $\chi^2$  surface would then reveal whether the fitting equation is sensitive to the collision cross-section.

Plots of the electron energy distribution function for experimental parameters should be used for choosing a discharge current that minimizes the Doppler shift bias associated with two-step excited ion production processes, yet allows sufficient signal for recording the spectra. Temperature data may prove useful for further analysis of this diagnostic technique. For this reason, a thermocouple should be used to measure discharge tube wall temperatures. Another alternative is to use a water cooling jacket around the discharge tube to fix the wall at a desired temperature.

## Appendix A: Example Search for Minima of $\chi^2$

### Units:

$$\text{angstrom} := 10^{-10} \cdot \text{m}$$

$$\text{amu} := 1.6605402 \cdot 10^{-27} \cdot \text{kg} \quad \text{Atomic mass unit}$$

### Constants:

$$c := 299792458 \frac{\text{m}}{\text{sec}} \quad \text{Velocity of light}$$

$$k_B := 1.380658 \cdot 10^{-23} \frac{\text{joule}}{\text{K}} \quad \text{Boltzmann's constant}$$

$$D_a := 900 \cdot \text{cm}^2 \cdot \frac{\text{torr}}{\text{sec}} \quad \text{reduced ambipolar diffusion constant}$$

$$q := 1.60217733 \cdot 10^{-19} \cdot \text{coul} \quad \text{elementary charge}$$

$$\tau := 66 \cdot 10^{-9} \cdot \text{sec} \quad \text{Lifetime of B State of N}_2^+ \text{ ion}$$

$$M_{\text{He}} := 4 \cdot \text{amu} \quad \text{Mass of helium atom}$$

$$M_{\text{N}2} := 28 \cdot \text{amu} \quad \text{Mass of N}_2 \text{ molecule/ion}$$

$$\mu := \frac{M_{\text{He}} \cdot M_{\text{N}2}}{M_{\text{He}} + M_{\text{N}2}}$$

$$\mu = 3.5 \cdot \text{amu} \quad \text{reduced collision mass}$$

**Data:**

$$Ra := 0.4 \cdot \text{cm}$$

Discharge tube radius

$$T := 597 \cdot \text{K}$$

Ion translational temperature

<u>Gas Pressure</u>	<u>E-scaled doppler shift</u>	<u>error in E-scaled doppler shift</u>
$P := \begin{bmatrix} 0.5 \\ 0.75 \\ 1 \\ 2 \\ 4.0 \\ 6.0 \end{bmatrix} \cdot \text{torr}$	$\text{delnu normE} := \begin{bmatrix} 7.58 \cdot 10^{-8} \\ 7.58 \cdot 10^{-8} \\ 7.54 \cdot 10^{-8} \\ 4.36 \cdot 10^{-8} \\ 1.85 \cdot 10^{-8} \\ 1.86 \cdot 10^{-8} \end{bmatrix} \frac{\text{cm}}{\text{volt}}$	$\sigma_{\text{Shift}} := \begin{bmatrix} 5.01 \cdot 10^{-9} \\ 2.45 \cdot 10^{-9} \\ 2.65 \cdot 10^{-9} \\ 5.42 \cdot 10^{-9} \\ 3.4 \cdot 10^{-9} \\ 4.25 \cdot 10^{-9} \end{bmatrix} \frac{\text{cm}}{\text{volt}}$

$$P_{\text{N}2} := 0.01 \cdot \text{torr}$$

Partial pressure of nitrogen

**Expressions:**

$$\text{Terminate} := \text{length}(P) - 1 \quad \text{End of series value}$$

$$k := 0.. \text{Terminate} \quad \text{Iterator variable}$$

$$P_{\text{He}_k} := P_k - 0.01 \cdot \text{torr} \quad \text{Partial pressure of helium}$$

$$N_k := \frac{P_{\text{He}_k}}{k_B \cdot T} \quad \text{Helium number density}$$

$$V := \sqrt{\frac{3 \cdot k_B \cdot T}{\mu}} \quad \text{relative collision velocity}$$

$$\Gamma(Qv, k) := \frac{M_{He}}{M_{N2} + M_{He}} \cdot Qv \cdot N_k \cdot V \quad N_2-He \text{ collision frequency}$$

$$\gamma_k := \frac{D_a}{P_{He_k}} \cdot \frac{T}{273K} \cdot \left( \frac{2.405}{Ra} \right)^2 \quad \text{Wall collision rate}$$

$$\lambda(Qq, k) := \left( Qq \cdot N_k + \frac{\gamma_k}{V} \right)^{-1} \quad \text{Mean free path for quenching}$$

Theoretical expression for E-scaled doppler shift

$$y(Qv, Qq, k) := \frac{q}{M_{N2} \Gamma(Qv, k) \cdot c} \cdot \left[ 1 - \frac{1}{1 + \Gamma(Qv, k) \cdot \tau} \cdot \frac{1 - \exp\left(-\frac{\lambda(Qq, k)}{V \cdot \tau} - \frac{\Gamma(Qv, k) \cdot \lambda(Qq, k)}{V}\right)}{1 - \exp\left(-\frac{\lambda(Qq, k)}{V \cdot \tau}\right)} \right]$$

vel := 1.. 50

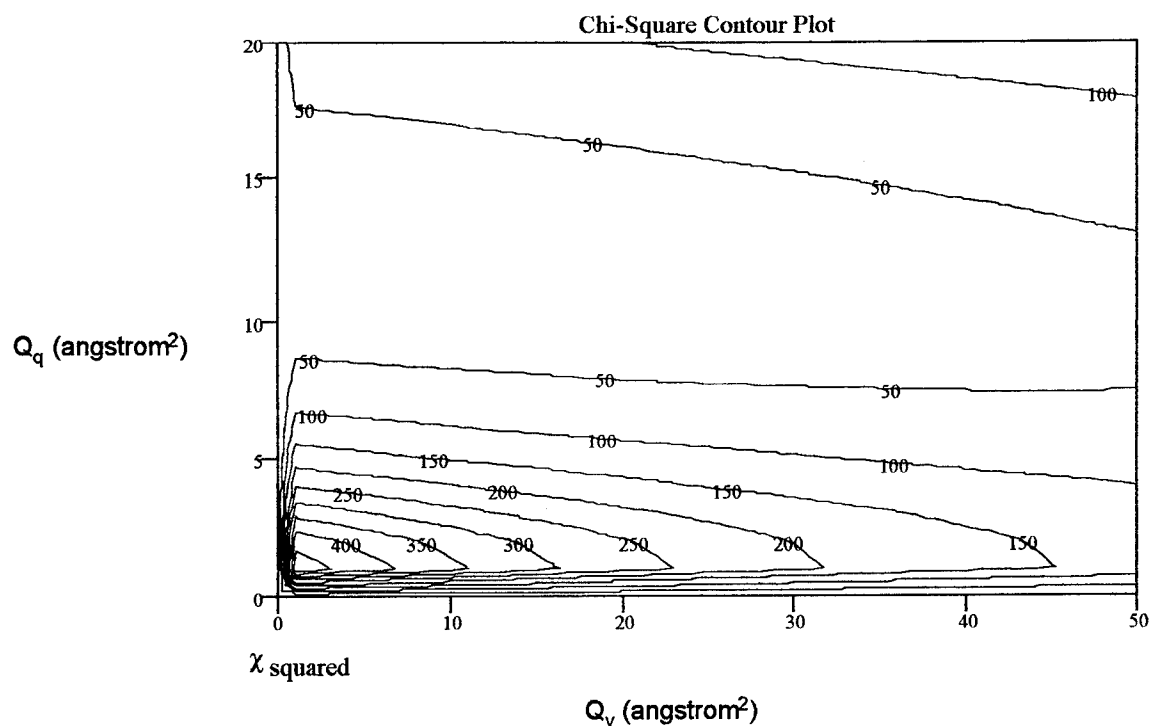
quench := 1.. 20

$$Qv_{vel} := vel \cdot \text{angstrom}^2 \quad \text{Trial values for momentum-transfer cross-section}$$

$$Qq_{quench} := quench \cdot \text{angstrom}^2 \quad \text{Trial values for quenching cross-sections}$$

Chi-square calculation

$$\chi^2_{\text{vel, quench}} := \sum_k \left( y(Qv_{vel}, Qq_{quench}, k) - \text{delnu normE}_k \right)^2 \cdot \frac{1}{(\sigma_{\text{Shift}})_k^2}$$



Chi-square values

$Q_q$  (angstrom $^2$ )

	8	9	10	11	12	13	14
1	64.633	45.79	33.018	25.098	21.191	20.691	23.139
2	63.524	45.115	32.675	25.02	21.328	21.006	23.602
3	62.455	44.47	32.357	24.962	21.482	21.335	24.078
4	61.423	43.855	32.063	24.924	21.652	21.678	24.565
5	60.428	43.27	31.793	24.905	21.839	22.035	25.063
6	59.469	42.713	31.547	24.906	22.042	22.405	25.572
7	58.547	42.185	31.324	24.926	22.26	22.788	26.093

Y-axis:  $Q_v$  (angstrom $^2$ )

X-axis:  $\chi$  squared =

## Appendix B: Residence Time in Discharge Tube

### units:

$$\text{sccm} := 12.66667 \cdot \text{torr} \cdot \frac{\text{cm}^3}{\text{sec}}$$

### Data:

Total Pressure

$$P := \begin{bmatrix} 0.5 \\ 0.75 \\ 1 \\ 1.5 \\ 2 \\ 3 \\ 5 \\ 5 \\ 6 \end{bmatrix} \cdot \text{torr}$$

Helium Flow rate

$$\Phi_{\text{He}} := \begin{bmatrix} 4 \\ 5.994 \\ 8.019 \\ 12.069 \\ 16.119 \\ 24.21 \\ 32.32 \\ 40.42 \\ 48.52 \end{bmatrix} \cdot \text{sccm}$$

Nitrogen Flow rate

$$\Phi_{\text{N2}} := \begin{bmatrix} 0.08 \\ 0.08 \\ 0.08 \\ 0.08 \\ 0.08 \\ 0.08 \\ 0.08 \\ 0.08 \\ 0.08 \end{bmatrix} \cdot \text{sccm}$$

$$r := 0.4 \cdot \text{cm} \quad \text{discharge tube radius}$$

$$x := 51.667 \cdot \text{mm} \quad \text{length of horizontal section of discharge tube}$$

### Expressions:

$$A := \pi \cdot r^2$$

$$A = 0.503 \cdot \text{cm}^2 \quad \text{cross-sectional area of discharge tube}$$

$$\Phi_{\text{tot}} := \overrightarrow{(\Phi_{\text{N2}} + \Phi_{\text{He}})}$$

$$\Phi_{\text{tot}} = \begin{bmatrix} 4.08 \\ 6.074 \\ 8.099 \\ 12.149 \\ 16.199 \\ 24.29 \\ 32.4 \\ 40.5 \\ 48.6 \end{bmatrix} \text{ sccm} \quad \text{Total mass flow rate}$$

The flow velocity is given by:

$$v := \frac{\overrightarrow{\Phi}_{\text{tot}}}{P \cdot A}$$

$$v = \begin{bmatrix} 2.056 \\ 2.041 \\ 2.041 \\ 2.041 \\ 2.041 \\ 2.041 \\ 2.04 \\ 1.633 \\ 2.041 \\ 2.041 \end{bmatrix} \text{ m sec}^{-1}$$

$v_{\text{mean}} := \text{mean}(v)$

$$v_{\text{mean}} = 199.729 \frac{\text{cm}}{\text{sec}}$$

Then the residence time in the tube is:

$$\tau := \frac{x}{v_{\text{mean}}}$$

$$\tau = 0.026 \text{ sec}$$

## Appendix C: Resolution of Spectrometer

### Units

$$\text{amu} := 1.660540210^{-27} \cdot \text{kg}$$

atomic mass unit

$$\text{angstrom} := 10^{-10} \cdot \text{m}$$

Angstrom

### Constants

$$c := 299792458 \frac{\text{m}}{\text{sec}}$$

Velocity of light

$$q := 1.6021773310^{-19} \cdot \text{coul}$$

Electron charge

$$M_{\text{He}} := 4.0026 \text{amu}$$

Mass of Helium atom

$$M_{\text{N}_2} := 2 \cdot 14.0067 \text{amu}$$

Mass of N<sub>2</sub> molecule

$$k_B := 1.38065810^{-23} \frac{\text{joule}}{\text{K}}$$

Boltzman constant

$$\tau_B := 66 \cdot 10^{-9} \cdot \text{sec}$$

Lifetime of N<sub>2</sub> + B state

$$T := 600 \text{ K}$$

Gas temperature

$$Q_V := 34 \text{ angstrom}^2$$

N<sub>2</sub>\*-He collision cross-section

$$\nu_{B0X0} := \frac{c}{3914 \text{ angstrom}}$$

frequency of B<sup>2</sup> Sigma (v=0) to X<sup>2</sup>sigma (v=0) transition

### Doppler broadening in :

$$\Delta\nu_{\text{doppler}}(v_0) := \frac{2 \cdot v_0}{c} \cdot \left( \frac{2 \cdot k_B \cdot T \cdot \ln(2)}{M_{\text{N}_2}} \right)^{\frac{1}{2}}$$

Frequency

$$\Delta\sigma_{\text{doppler}}(v_0) := \frac{\Delta\nu_{\text{doppler}}(v_0)}{c}$$

Wavenumber

### Pressure broadening:

$$\nu_{\text{coll}}(P) := \frac{P}{k_B \cdot T} \cdot Q_V \cdot \left[ \frac{8 \cdot k_B \cdot T}{\pi} \cdot \left( \frac{1}{M_{\text{N}_2}} + \frac{1}{M_{\text{He}}} \right) \right]^{\frac{1}{2}}$$

collision frequency as a function of pressure

$$\Delta\nu_{\text{pressure}}(P) := \frac{1}{2\pi} \cdot \left( \frac{1}{\tau_B} + 2 \cdot v_{\text{coll}}(P) \right) \quad \text{Pressure broadening in frequency.}$$

$$\Delta\sigma_{\text{pressure}}(P) := \frac{\Delta\nu_{\text{pressure}}(P)}{c} \quad \text{Pressure broadening in wavenumber.}$$

### Resolution of spectrometer

$$R_1 := 4.3 \cdot 10^5 \quad \text{Resolving power of Bomem spectrometer}$$

$$\Delta\sigma_{\text{inst}}(\sigma, R) := \frac{\sigma}{R}$$

$$\Delta\sigma_{\text{Bomem}}(\sigma) := \Delta\sigma_{\text{inst}}(\sigma, R_1)$$

### Comparison of linewidths for B-X (0,1) transition as a function of Pressure.

$$i := 10, 20.. 760 \quad \text{iterator}$$

$$P_i := i \cdot \text{torr} \quad \text{Pressure variable}$$

$$\sigma_{\text{BX}} := \frac{v_{\text{B0X0}}}{c}$$

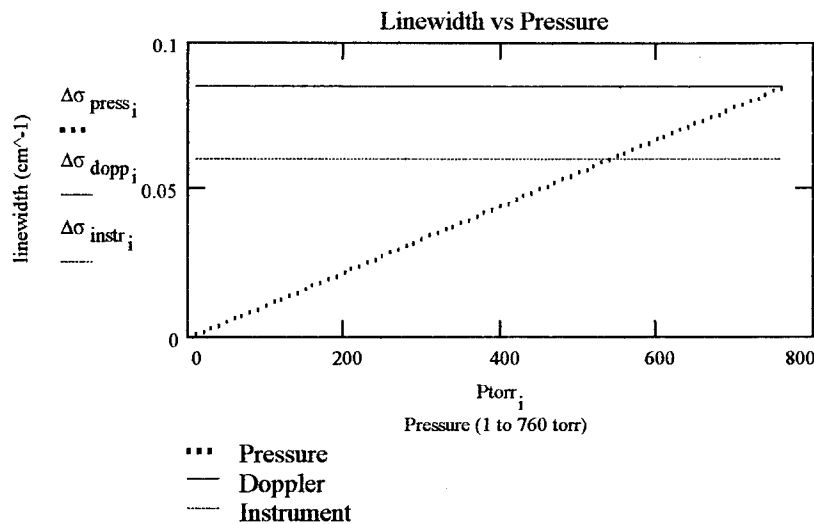
$$\sigma_{\text{BX}} = 2.555 \cdot 10^4 \cdot \text{cm}^{-1} \quad \text{wavenumber of transition}$$

$$\Delta\sigma_{\text{press}_i} := \Delta\sigma_{\text{pressure}}(P_i) \quad \text{Pressure broadening}$$

$$\Delta\sigma_{\text{dopp}_i} := \Delta\sigma_{\text{doppler}}(\sigma_{\text{BX}} \cdot c) \quad \text{Doppler broadening}$$

$$\Delta\sigma_{\text{instr}_i} := \Delta\sigma_{\text{Bomem}}(\sigma_{\text{BX}}) \quad \text{Instrument broadening}$$

$$P_{\text{torr}, i} := \frac{P_i}{\text{torr}}$$



As is seen, at subatmospheric pressures, the Doppler linewidth dominates. The instrument broadening is comparable to the Doppler broadening. The resolution in this experiment is limited by Doppler broadening

#### Precision of linecenter for B-X transition

$$\delta\sigma := \frac{\Delta\sigma_{\text{doppler}}(\sigma_{\text{BX}}^c)}{20}$$

Rule of thumb is that line position can be determined to within 1/20 the width of the line [28:1]

$$\delta\sigma = 0.004 \cdot \text{cm}^{-1}$$

To detect a line position shift, the separation  $\Delta\sigma_{\text{tot}}$ , between two separately measured peaks must be greater than the uncertainty of the line position.

$$\Delta\sigma_{\text{tot}} := \delta\sigma$$

In wavenumbers

$$\Delta\sigma_{\text{tot}} = 0.004 \cdot \text{cm}^{-1}$$

$$\Delta v_{\text{tot}} := c \cdot \Delta \sigma_{\text{tot}}$$

$$\Delta v_{\text{tot}} = 1.269 \cdot 10^8 \cdot \frac{1}{\text{sec}} \quad \text{In frequency}$$

The minimum Doppler shift that can be detected is then given by:

$$\text{Shift}_{\text{min}} := \frac{\Delta v_{\text{tot}}}{v_{\text{B0X0}}}$$

$$\text{Shift}_{\text{min}} = 1.657 \cdot 10^{-7}$$

This is of comparable magnitude to the minimum Doppler shift values measured in this experiment

## Bibliography

1. Mason, E.A. and E.W. McDaniel. Transport Properties of Ions in Gases. New York: John Wiley & Sons, 1988.
2. Biondi, M.A. and L.M. Chanin. "Mobilities of Atomic and Molecular Ions in the Noble Gases," Physical Review, 24(4), 910-916, (15 May 1954).
3. Johnson, R., H.L. Brown, and M.A. Biondi. "Ion-Molecule Reactions Involving  $N_2^+$ ,  $N^+$ ,  $O_2^+$ , and  $O^+$  Ions from 300° K to  $\sim$ 1 eV," The Journal of Chemical Physics, 52 (10), 5080-5084.
4. McFarland, M, *et al*. "Flow-drift Technique for Ion Mobility and Ion-molecule Reaction Rate Constant Measurements. I. Apparatus and Mobility Measurements," The Journal of Chemical Physics, 59 (12), 6610-6619, (15 December 1973).
5. Haese, N.N., Fu-Shih Pan, and Takeshi Oka. "Doppler Shift and Ion Mobility Measurements of  $ArH^+$  in a He dc Glow Discharge by Infrared Laser Spectroscopy." Physical Review Letters, 50 (20), 1575-1578, (16 May 1983).
6. Gudeman, C.S., *et al*. "Velocity-Modulated Infrared Laser Spectroscopy of Molecular Ions: The  $v_1$  Band of  $HCO^+$ ," Physical Review Letters, 50 (10), 727-731, (7 March 1983).
7. Radunsky, M.B., and R.J. Saykally, "Non-Intrusive Measurement of Axial Electric Fields In Low-Pressure Glow Discharges By Velocity Modulation Laser Spectroscopy," Chemical Physics Letters, 152 (4,5), 419-423, (18 November 1988).
8. Martin, P.A., and G. Guelachvili. "Velocity-Modulation Fourier-Transform Spectroscopy of Molecular Ions," Physical Review Letters, 65 (20), 2535-2538, (12 November 1990).
9. Hong, X., and T. Miller. "Velocity Modulated Fourier Transform Emission as a Plasma Diagnostic and a Spectroscopic Tool," The Journal of Chemical Physics, 101 (6), 4572-4577, (15 September 1994).
10. Lindinger, W., and D.L. Albritton. "Mobilities of Various Mass-identified Positive Ions in Helium and Argon," The Journal of Chemical Physics, 62 (9), 3517-3522, (1 May 1975).

11. Desesquelles, M., M. Dufay, and M.C. Poulicac. "Lifetime Measurement of Molecular States With an Accelerated Ion Beam," *Physics Letters*, 27A (2), 96-97, (3 June 1968).
12. McDaniel, E.W., and E. A. Mason. The Mobility and Diffusion of Ions In Gases. New York: John Wiley & Sons, 1973.
13. Reif, F. Fundamentals of Thermal and Statistical Physics. New York: McGraw-Hill, 1965.
14. Hori, H., et al. "State-specific Mobility of Excited Cadmium and Calcium Ions in a Discharge Plasma Measured by a Tunable Diode Laser," Physical Review E, 47 (1), 623-634, (January 1993).
15. Loewenstein, E. V., "Fourier Spectroscopy: An Introduction," Aspen International Conference on Fourier Spectroscopy, 1970. G.A. Vanasse, A.T. Stair Jr., and D.J. Baker, eds., AFCRL-71-0017.
16. Bomem-Research Software User's Guide., Version 6, Revision 1, (December 1990).
17. Instruction manual, EW series, Glassman High Voltage Inc., (29 September 1993).
18. Hamamatsu Catalog, (October 1990).
19. Herzberg, G. Molecular Spectra and Molecular Structure I. Spectra of Diatomic Molecules., New York: Van Nostrand Reinhold Co., 1950.
20. DeJoseph, C.A. Private communication.
21. Radunsky, M.B., and R.J. Saykally. "Electronic Absorption Spectroscopy of Molecular Ions in Plasmas by Dye Laser Velocity Modulation: The A  $\leftarrow$  X system of  $\text{N}_2^+$ ," Journal of Chemical Physics, 87 (2), (15 July 1987).
22. Nagpal, R. Private communication.
23. Pitts, Donald R., and L.E. Sissom. Schaum's Outline of Theory and Problems of Heat Transfer. New York: McGraw-Hill, 1977.
24. Bevington, P.R. and D.K. Robinson. Data Reduction and Error Analysis for the Physical Sciences, New York: McGraw-Hill, 1992.
25. Mathcad 5.0 Plus User's Guide, MathSoft Inc., 1994.

26. Nasser, E. Fundamentals of Gaseous Ionization and Plasma Electronics.  
New York: Wiley-Interscience, 1971.
27. Press, W.H., et al. Numerical Recipes: The Art of Scientific Computing,  
Cambridge: Cambridge University Press, 1986.
28. Cole, A.R.H. Tables of Wavenumbers for the Calibration of Infrared Spectrometer.  
Oxford: Pergamon Press, 1977.

## Vita

Captain Patrick D. Kee was born April 5, 1966 in Omaha, Nebraska. He graduated from Daniel J. Gross High School in Bellevue, Nebraska in 1984. In May of 1989, he graduated from the University of Nebraska at Omaha with a Bachelor of Arts Degree in Physics, and was a Distinguished Graduate of the Air Force Reserve Officer Training Corps. In August of 1989, he received a direct duty assignment to Wright Research and Development Center (now Wright Laboratory), and was placed in the Advanced Plasma Research Group. At Wright Laboratory he did in-house experimental research on diamond thin films, increasing the laboratory's production capability from a box of equipment in the corner of a room to an operating microwave plasma deposition reactor. In August 1991, he was reassigned to Foreign Technology Division (now the National Air Intelligence Center), as a Tactical Systems Threat Analyst, where he wrote the Airlift Threat Environment Description, the Defense Intelligence Agency's baseline threat study produced to support of the acquisition of airlift aircraft. He then entered the School of Engineering, Air Force Institute of Technology, in May of 1993.

Permanent Address: 1224 North 95th Ave  
Omaha, NE 68141

# REPORT DOCUMENTATION PAGE

Form Approved  
OMB No. 0704-0188

Public reporting burden for this collection of information is estimated to average 1 hour per response, including the time for reviewing instructions, searching existing data sources, gathering and maintaining the data needed, and completing and reviewing the collection of information. Send comments regarding this burden estimate or any other aspect of this collection of information, including suggestions for reducing this burden, to Washington Headquarters Services, Directorate for Information Operations and Reports, 1215 Jefferson Davis Highway, Suite 1204, Arlington, VA 22202-4302, and to the Office of Management and Budget, Paperwork Reduction Project (0704-0188), Washington, DC 20503.

1. AGENCY USE ONLY (Leave blank)	2. REPORT DATE	3. REPORT TYPE AND DATES COVERED
	December 1994	Master's Thesis
4. TITLE AND SUBTITLE		5. FUNDING NUMBERS
MEASUREMENT OF N <sub>2</sub> <sup>+</sup> MOBILITY IN He VIA FOURIER TRANSFORM EMISSION SPECTROSCOPY		
6. AUTHOR(S)		
Patrick D. Kee, Capt., USAF		
7. PERFORMING ORGANIZATION NAME(S) AND ADDRESS(ES)		8. PERFORMING ORGANIZATION REPORT NUMBER
Air Force Institute of Technology 2750 P Street Wright-Patterson AFB, OH 45433-6583		AFIT/GAP/EN/94D-4
9. SPONSORING / MONITORING AGENCY NAME(S) AND ADDRESS(ES)		10. SPONSORING / MONITORING AGENCY REPORT NUMBER
Charles A. DeJoseph, Ph.D, GS-13 WL/POOC-3 Bldg 450 2645 Fifth St Ste 13 Wright-Patterson AFB, OH 45433-7919		

11. SUPPLEMENTARY NOTES

12a. DISTRIBUTION / AVAILABILITY STATEMENT	12b. DISTRIBUTION CODE
Approved for public release; distribution unlimited	

13. ABSTRACT (Maximum 200 words)

Recently, Hong and Miller<sup>1</sup> used Fourier Transform Emission (FTE) spectroscopy to determine the N<sub>2</sub><sup>+</sup> mobility in helium by relating the observed Doppler shift of the N<sub>2</sub><sup>+</sup> (B-X) transition to the measured electric field in the discharge as determined by probes. In order to establish the technique in-house, this effort duplicated that experiment and investigated the sensitivity and utility of the method. Doppler shift measurements in this experiment disagreed significantly with those reported by Hong and Miller. Attempts to reduce the data (and thus determine the mobility) using a model developed by Hong and Miller were unsuccessful. The model did not qualitatively or quantitatively describe the Doppler shifts observed in this work. At this time, an explanation of the differences between the two experiments is not known. Possibilities include effects of striations on the Doppler shift measurements, competition between one- and two-step excitation of the N<sub>2</sub><sup>+</sup> (B-X) state, and failure to interpret the Hong and Miller model correctly. Subsequent attempts to model Hong and Miller's own data (taken from their figures) yielded mobility parameters which disagreed with their published results.

1. Hong, X. and T.A. Miller. J. Chem. Phys. vol. 101, p. 4572 (1994).

14. SUBJECT TERMS		15. NUMBER OF PAGES	
Fourier transform spectroscopy, ion mobility, ion transport, gas discharges, DC discharges, plasma physics,		102	
		16. PRICE CODE	
17. SECURITY CLASSIFICATION OF REPORT	18. SECURITY CLASSIFICATION OF THIS PAGE	19. SECURITY CLASSIFICATION OF ABSTRACT	20. LIMITATION OF ABSTRACT
UNCLASSIFIED	UNCLASSIFIED	UNCLASSIFIED	